Università degli Studi di Genova

Doctorate in Science and Technology of Chemistry and Materials

Curriculum of Pharmaceuticals, Food and Cosmetic Sciences

XXXVI cycle

DEVELOPMENT OF EXOSOMES AND BIOINSPIRED VESICLES FOR DRUG DELIVERY

Supervisor

Prof. Gabriele Caviglioli

Ph. D. candidate

Alice Balboni

Abstract

It has been already demonstrated that cell membrane-coated biomaterials are endowed with superior biocompatibility, decreased clearance rate from the rethiculoendothelial system, improved colloidal stability and homotypic targeting abilities. In the present research, two different types of cell cultures were employed as cell membranes (CM) source for the preparation of biomimetic nanosystems: glioblastoma primary cells, obtained from patient biopsies, and colorectal cancer cells cultured from a murine cell line. Isolated CM were analysed in terms of retained protein content and the elimination of residual genetic material from parent cells was assessed in this fraction. Glioblastoma or colorectal cancer CM were used to prepare CM-derived vesicles, and BPA-loaded artificial liposomes were developed and characterize for a future functionalization with glioblastoma CM. Colorectal cancer CM were also hybridized with synthetic, to achieve hybrid vesicles improving the production yield. CM and lipids were hybridized following two different techniques, namely the co-extrusion or micromixing using a microfluidic device. All the obtained formulations were characterized in terms of physico-chemical properties, morphology and process yield; for hybrids, membrane fusion efficiency was also evaluated. The *in vitro* internalization and homologous selectivity of biomimetic vesicles into parent cells and different cell types were investigated by confocal microscopy and flow cytometry. The obtained results confirmed that pure and stable bio-inspired nanosystems were developed with good production yield both from primary cells and from the immortalized cell line. Moreover, thanks to the cell-derived membranes, their selective cellular uptake sensibly increased in comparison to artificial liposomes, reaching the highest value in homotypic internalization into parent cells.

1. General introduction

1. General introduction

1.1. Exosomes as drug delivery systems

Exosomes are nanoscaled extracellular vesicles produced by cells to vehiculate bioactive molecules involved in cell-to-cell signalling. The exosome membrane is a phospholipid bilayer mainly composed of phosphatidylserine, sphingomyelin, cholesterol, ceramides, and ganglioside GM3 [1]. As they originate from the membrane of late endosomes, their membrane is decorated with proteins characteristic of endosomes and plasma membrane of the parent cell [2]. Hence, their proteome is particularly rich in phospholipases and lipid-related proteins, tetraspanins (CD9, CD63, CD81 and CD82), heat shock proteins (HSP70, HSP90), and transmembrane proteins specific to the cell of origin [3]. Besides characteristic proteins and lipids, the ability of exosomes to carry nucleic acids such as messenger RNA (mRNA), small interfering RNA (siRNA), microRNA (miRNA) and DNA fragments, arose strong interest in the field of gene therapy and gene delivery [1]. As well as in healthy conditions, exosomes play a crucial role in cell communication in several pathological states, such as cancer, and neurodegenerative, cardiovascular, infectious and respiratory diseases. They are involved in the transfer of specific proteins, lipids, in the transmission of downstream signalling events, and in the delivery of specific nucleic acid cargo [4]. A unique characteristic of these vesicles is the specific interaction with a target recipient cell. Exosome targeting ability is due to the asymmetrical lipid distribution and specific protein composition of their membranes [5] and it is possibly exploited by cancer cells to transfer material amongst tumor formations and in the process of metastatization [6].

The described characteristics of exosomes, namely their nanoscaled dimensions and their peculiar organotropism, together with their innate biocompatibility, make these vesicles good candidates as drug delivery systems. Many authors have proposed exosomes and exosome-mimetic systems as nanocarriers for cancer treatment, studying different techniques for vesicle isolation and purification, drug loading and surface functionalization [7]. The most diffused techniques used for exosome isolation from culture media are summarized in Fig. 1. The drug loading methods can be classified in endogenous and exogenous loading: endogenous loading relies on the incubation of the parent cells with the drug to be loaded, or on the genetic modification of cells to induce the expression of proteins or nucleic acids to be included in the released vesicles;

exogenous loading implicates the incorporation of the drug in exosomes previously isolated from cell culture media or body fluids (urine, blood, saliva, breast milk, etc.) [8].

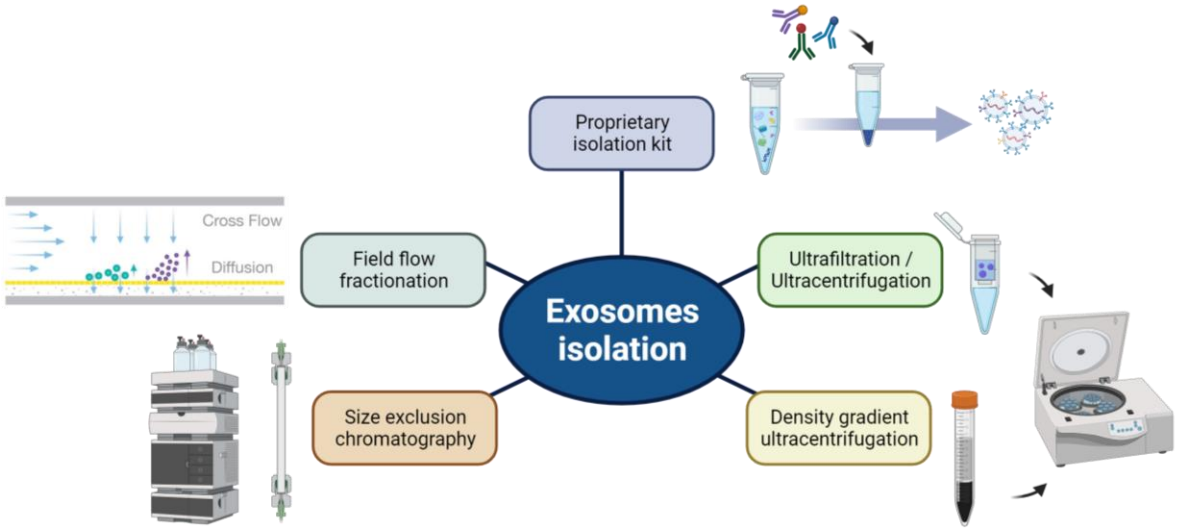

Figure 1: Schematic representation of the different methods developed for exosome isolation. Created with BioRender.com

In spite of the comprehensive research carried out following this approach, the clinical translation of exosomes as drug carriers is still a challenge. The low production yield combined with the complicated exosome isolation make them hard to provide in a useful concentration [9]. Moreover, their structural heterogeneity and batch-to-batch differences explain the difficulties in establishing a standard, scalable, and cost-effective GMP procedure for exosome isolation, purification and use as therapeutic agents [10]. Consequently, to address the described limitations, the pharmaceutical nanotechnology community focused the attention on other bio-mimetic and cell-derived systems, which will be discussed in the following chapter.

1.2 Cell-derived bio-mimetic nanosystems: different cells, cargoes, and formulation techniques

As cell-to-cell homotypic interactions exploit special biofunctions such as characteristic phospholipids and lipoproteins, the use of cell-derived materials to form nanovesicles or to coat nanoparticles represents a good alternative to artificial surface functionalization. Moreover, the direct use of cell membrane (CM) is an efficient approach to avoid expensive and time-consuming biomaterial isolation and nanosystem surface decoration. It has been studied that CM-coated biomaterials are endowed with superior biocompatibility, decreased clearance from the reticuloendothelial system, improved colloidal stability and homotypic targeting abilities [11, 12] (Fig 2). Rao et al. hypothesized that the CM-related stabilizing effect on nanosized systems can be attributed to flexible and hydrophilic surface glycans on CMs, which prevent aggregation of the structures [13].

Current research on CM-derived nanoparticles (NPs) has been focusing on outer membranes of platelets, erythrocytes, leukocytes, stem and cancer cells [14]. Erythrocytes were considered ideal sources thanks to their membrane proteins that confer immune tolerance [13, 15, 16], similarly to CD47 and CD45, which are present on leukocyte membrane [17, 18]. Moreover, beside bypassing the immune system, leukocytes and platelets have been studied because of their characteristic functional proteins such as lymphocyte function-associated antigen 1 and macrophage-1, CD41, CD42b, CD61, which allow binding to inflamed endothelium and targeting to tumors [19-21]. Cancer cells were also identified as good candidates for CM coating of NPs, because of their immune evasion and good homotypic cell recognition, namely innate cancer targeting ability, which can be attributed to the transfer of cell adhesion molecules with homotypic binding properties [11, 22, 23].

Cell membranes have been exploited to coat polymeric or inorganic NPs or used as such for the formulation of CM-derived vesicles. Red blood CMs have been studied to improve the circulation time of a wide variety of nanomaterials. Starting from gold nanoparticles, relevant tools in cancer research thanks to their successful use in imaging, sensing, and photodynamic therapy, Gao et al. used red blood CMs to coat AuNPs, minimizing their uptake by macrophages and significantly improving their blood circulation [24]. In two

following research studies, red blood CMs were exploited with the same aim for gold nanocages and gold nanorods [25, 26]. Red blood CMs have also been used to increase the biocompatibility of magnetic nanoparticles, widely used as contrast agents for magnetic resonance imaging due to their superparamagnetic properties. Xuan et al. attached magnetic colloids onto the surface of hypocrellin B-loaded mesoporous silica NPs, and further coated them with red blood CMs, achieving improved hypocrellin B retention compared to uncoated ones [27]. In another work, Fe_3O_4 nanoparticles were coated with the same cell-derived material, achieving the evasion of immune responses on both the cellular level (myeloid-derived suppressor cells) and the humoral level (IgM and IgG) [28]. Red blood CM-coated Fe_3O_4 theranostic NPs were also described by Ren et al. [29], who evidenced *in vivo* prolonged blood retention time, high tumor accumulation and relatively lowered liver biodistribution. Other versatile cores for membrane cloaking are metal-organic frameworks (MOFs), which consist in hybrid porous nanomaterials composed of metal ions or metal clusters combined with organic ligands [30]. These attractive platforms can serve as vehicles embedding drugs and biomolecules in their tight cavities with high loading efficiency. Zhang et al. delivered glucose oxidase and tirapazamine to tumor sites using zeolitic imidazolate framework-8 (ZIF-8), reaching high tumor accumulation thanks to red blood CM coating of MOFs surface [31]. ZIF-8 was also formulated by Alyami et al. exploiting cancer cells as membrane sources: the authors achieved an excellent tumor targeted delivery of CRISPR/Cas9 by coating the system with cervix carcinoma or breast adenocarcinoma CMs [32]. Indeed, besides the significant improvements provided by red blood CM coating to bio-mimetic systems, the unique homologous targeting ability characterizing cancer CM coating was evidenced in several works. Nie et al. exploited breast cancer CM for mesoporous silica NPs coating [33], whereas Sun et al. cloaked the surface of gold nanorods for oral squamous cancer cell radiosensitizing [34]. Lung carcinoma cells have been widely used in CM coating: in an interesting work, an acetalated dextran-based NP core loaded with curcumin was coated with CMs derived from pulmonary epithelial cancer cells [35]. This type of CMs was also exploited to surround poly (lactic-co-glycolic acid) (PLGA) NPs by Liu et al., who compared the affinity for the originating cells of two bio-mimetic nanosystems coated with CMs or exosome membranes from the same cell line [36]. Polymeric NPs composed of PLGA are other popular inner cores for CM

decoration, being PLGA a biodegradable and biocompatible copolymer approved by FDA, many researchers have investigated the CM coating of PLGA NPs for developing drug delivery systems [23, 37-41]. Amongst the most interesting ones, Bose et al. reported that stem CM coating of VEGF (Vascular-Endothelial Growth Factor)-loaded PLGA NPs reduced the drug release rate as compared to that of bare ones [42]. Yang et al. demonstrated that mesenchymal stem CM coating of PLGA NP cores could improve the uptake of doxorubicin compared to uncoated systems, besides providing good cancer targeting and macrophage evasion. As in these works, several theranostic platforms took advantage from mesenchymal stem CM cloaking [43]: noteworthy is the work of Mu et al., who developed a biocompatible gene delivery platform using polydopamine-coated Fe_3O_4 NPs conjugated with siRNAs and surrounded by mesenchymal stem CM; CM-functionalized Fe_3O_4-polydopamine-siRNA NPs resulted to have tumor targeting capacity and excellent photothermal conversion efficiency [44]. Mesenchymal stem cell-derived membranes were also used to coat core-shell structures for the delivery of human tumor necrosis factor-related apoptosis-inducing ligand (TRAIL), achieving high cancer cell internalization and capability of inducing apoptosis in glioblastoma cells *in vitro* [45].

CMs have been used not only as biomaterial coating, but also for the formulation of membrane vesicles, mimicking an “empty cell” an innovative strategy for the targeted delivery of active molecules. Kaneti et al. exploited mesenchymal stem CMs for the preparation of “nanoghosts” able to evade the immune system while targeting multiple cancer cell types [46], whereas Go et al. selected monocyte CM to prepare monocyte-mimicking vesicles for the delivery of dexamethasone to treat systemic inflammatory response syndrome associated with infection [47]. Moreover, hybridization of cell membranes with liposomes was attempted with different cell types, to improve the yield of production of CM-vesicles while exploiting CM-derived material as targeting moieties for artificial liposomes. Natural killer cells were hybridized with synthetic fusogenic liposomes by Pitchaimani et al., obtaining a stable and cancer selective doxorubicin vehicle [48]. In another work, the authors designed mixed semi-synthetic vesicles by fusing red blood CMs and breast cancer CMs with artificial lipids, achieving efficient doxorubicin loading, high tumor accumulation and low clearance by the immune system [49], and finally Zhang et al. investigated the hybridization of lung cancer CMs with synthetic lipids for the co-delivery of siRNA and docetaxel [50].

Another aspect to consider when discussing CM coating is that the membrane sources predominantly used for this scope are murine or human cancer cell lines, rather than primary cells deriving from biopsies. The main reasons for the preferential use of cell lines are their ability to grow indefinitely *in vitro* and thus to provide an unlimited source of biological material, and the absence of ethical concerns for their supply. However, as pointed out by Mirabelli et al., it is important to consider that cell lines have some limitations in mimicking tumor microenvironment, especially due to the differences in terms of gene expression, as compared to *in vivo* tumor tissues [51]. Indeed, *in vitro* cultured cell lines do not have interactions with other cell types, thus their growth is not under the influence of cytokines and other cell-signalling molecules, and the native tissue architecture is lost [52]. Primary cells have a finite period of cell culture, ensuring genomic and phenotypic stability, differently from cell lines, which are subjected to changes within the proteome after prolonged passage as a result of selective pressures [53]. The difference in transcriptomic and proteomic between the derived cell line and the originating cancer tissue would justify the replacement of cell lines with primary cell cultures for some applications. This might be an important aspect to consider when exploiting CMs for the preparation of drug vehicles, given the impact of the characteristic proteome of the originating cell.

Different techniques have been studied to efficiently exploit CMs to improve the biocompatibility of nanovehicles. Co-extrusion of core NPs with CMs through a series of porous polymer films is currently the most common method for NPs coating: this process relies on shear force to deform or rupture vesicles, allowing them to reassemble around the cores in an energetically favoured process [14]. The parameters that can be regulated in order to control the final characteristics, such as uniformity, thickness, and stability, are the ratio between vesicles and NPs [39], flow rate, temperature, and pressure [54]. Coextrusion enables a good level of control and reproducibility, however, it is unfavourable for scaling-up due to the material loss and to the high incidence of membrane clogging when increasing formulation concentration. Amongst extruder membranes, the “tortuous path”-type (polyether sulfone filter), consisting of fibers crisscrossed over each other, can easily be clogged up, compared to the “nucleation track”-type membrane (polycarbonate filters), which is a thin polymer sheet with straight-sided holes of exact diameter [54].

Sonication constitutes another strategy for CM coating, enabling higher throughput compared to coextrusion. Within this method, the spontaneous fusion of CMs with core NPs is induced by acoustic waves and cavitation bubbles, which allow an increase in membrane permeability while maintaining protein and lipidic structure [55, 56]. Sonication amplitude and duration can be tuned, as well as temperature and particle density, to improve coating efficiency and system stability and to avoid aggregation [57].

CM coating has also been achieved by electroporation: similarly to sonication, this technique breaks down the dielectric layer over CMs, generating transient pores and thus permitting internalization of NPs [58]. However, as demonstrated by Hu et al., a sugar additive such as trehalose might necessary to prevent “electrofusion” and system aggregation within this approach [59].

A less diffuse method for CM coating is the freeze-thawing method, which was demonstrated to present several important drawbacks such as damage of membrane integrity and system aggregation [60].

Finally, hydrodynamic mixing through microfluidic devices is an emerging approach not only for CM coating, but in general for nanotechnology in drug delivery. Besides other groundbreaking advantages discussed in the following chapter, this technique allows to improve the mixing of core NPs and CMs, minimizing material loss, increasing core loading efficiency and allowing a scale up transition of the process [61]. Microfluidics strongly contributed to the optimization and standardization of the CM-coating processes, as pointed out by several authors [62]. In one interesting work, microfluidics was employed for the insertion of proteins deriving from leukocyte membranes into synthetic liposomes, achieving good selectivity of the vehicle for inflamed tissues [63]. In addition, microfluidic platforms have been coupled to other techniques: two noteworthy examples are the sonication-assisted microfluidic method for cancer CM coating of PLGA NPs [36] and the preparation of red blood CM-coated Fe_3O_4 NPs through the coupling of electroporation and microfluidics [13]. In both cases, this formulation technology significantly improved the throughput of the process, resulting in more

efficient systems also in terms of tumour accumulation, probably due to an increased degree of coating compared to traditional coating methods.

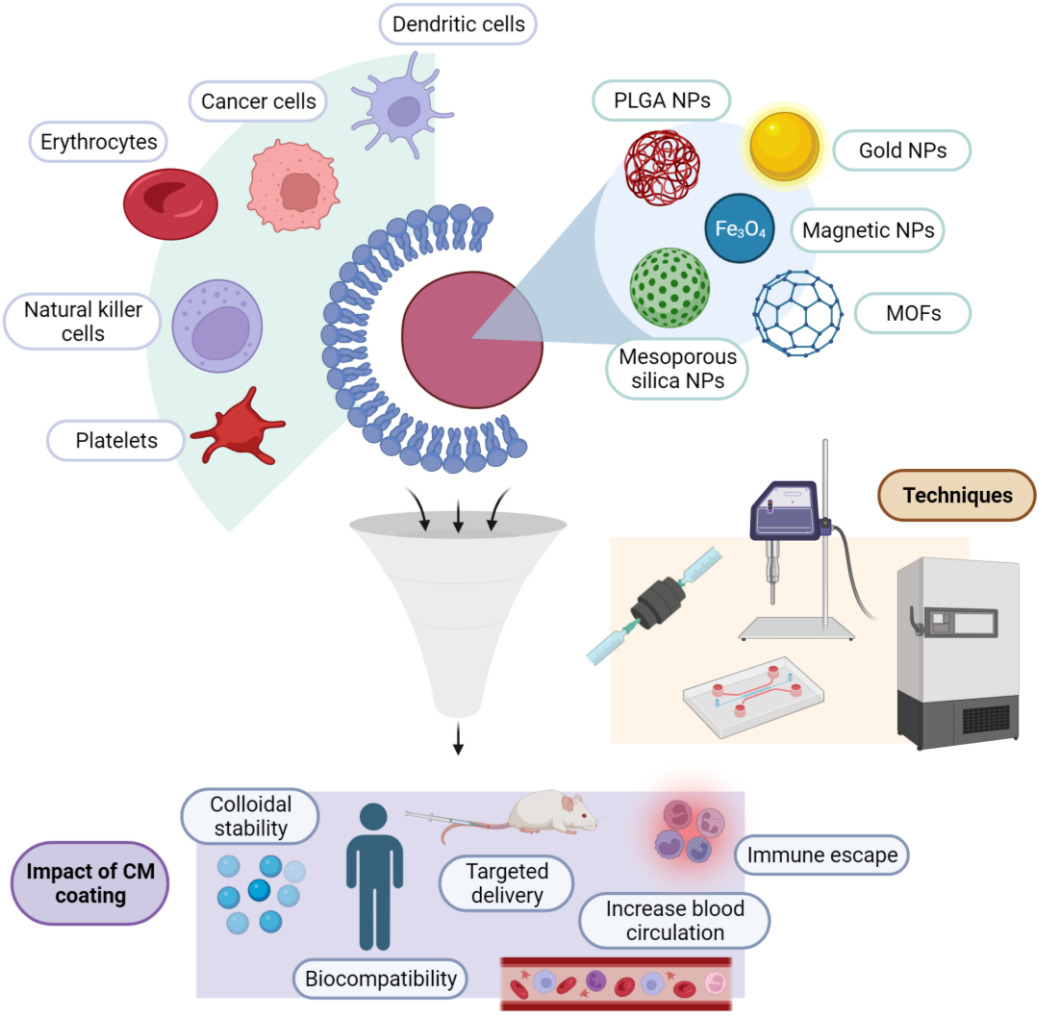

Figure 2: Schematic representation of the different strategies for CM-coating and the advantages related. Created with BioRender.com

1.3 Microfluidic devices in nanotechnology

Nanosystems are traditionally prepared using bulk methods. Recently, to improve the control on NP final properties for different applications, microfluidic techniques have arisen interest in researchers. The mixing using microchannels allows the handling of picoliter-scaled samples, rapid mass transfer, precise control over reaction conditions, cost-effectiveness, homogeneity of reaction environment and short production time [64]. Focusing the attention on organic NPs (liposomes, lipid NPs, polymeric NPs), the nanoprecipitation process of the organic precursor in an aqueous antisolvent has been increasingly replaced by the mixing of the two solutions through microfluidic platforms that, for organic NPs, are referred to as micromixers. The parameters that mostly affect the final NP characteristics when using micromixers include precursor concentration, temperature, pH, total flow rate (TFR) and flow rate ratio (FRR) [65]. TFR is intended as the sum of flow rates entering a microchannel from the inlets (Fig. 3), and FRR is the ratio of aqueous flow rate to NP precursor flow rate. Moreover, mixing time and uniformity are strongly related to the final size and size distribution of NPs, such that a shorter mixing time results in smaller particles and lower PDI [66]. Microfluidics enable efficient micrometer-scaled mixing with a mixing time resulting minor than the precipitation time, thus allowing the production of small NPs with a low PDI. The first liposome formulation obtained by Jahn et al. in 2004, using a microfluidic hydrodynamic focusing channel, attracted very much attention from both the engineering and pharmaceutic point of views, since the authors demonstrated that they could control liposome size by tuning solvent flow rates and concentrations [67]. However, their platform was endowed with laminar flow microchannels, which rely on diffusion-based mixing (straight microchannel), characterized by a low Reynolds number (Re ~ 1):

$$\mathrm{Re} = \frac{\rho \mathrm{U} \mathrm{Dh}}{\eta}$$

where ρ is the fluid density, U is the fluid velocity, D_h is the hydrodynamic diameter of the channel, and η is the dynamic viscosity of the fluid [64]. Consequently, their device was characterised by a long mixing time and low mixing efficiency due to the limited mass transfer occurring in diffusion between the laminar streams.

To overcome these issues, new technologies have been developed to fasten the mixing by inducing the production of a turbulent flow inside microchannels. These new methods are based on two different approaches, namely passive and active mixing. In passive mixing, flow disturbances are induced by unique geometrical structures designed in the microchannel, such as staggered herringbone [68], serpentine [69], and split-and-recombine [70] structures; these type of platforms can be fabricated from a variety of materials, being glass [71, 72] and silicon [73] the predominantly used ones.

Staggered Herringbone Micromixers (SHM) are the most popular devices: they provoke micromixing through chaotic advection, generated by structures designed on the floor of the microchannel [74] (Fig. 3). This results in faster mixing process, which is generally related with the production of small-sized NPs with excellent monodispersity. Moreover, the lower mixing time at lower flow rates leads to less dilution and shorter processing times for NP synthesis [75]. This technology is commercially available as a NanoAssemblr® platform consisting of a pump system and a cartridge with a Y-junction connected to a SHM region. In recent years, SHM method has been widely employed for the preparation of lipid NPs, hybrid PLGA-lipid NPs, liposomes, oil–in-water nanoemulsions and unilamellar vesicles [61, 75-77].

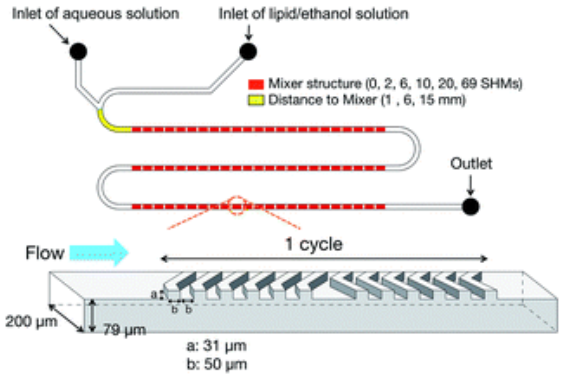

Figure 3: Schematic illustration of Staggered Herringbone Micromixer.
Reproduced from [65] under the Creative Commons Attribution license
(https://creativecommons.org/licenses/by-nc/3.0/).

Another micromixing technology relies on the split-and-recombine method (SAR) constituting the principle of bifurcating mixers and Tesla mixers (Fig. 4A). In this technique, the turbulence in the fluid stream is due to the microchannel path: it splits into two branches and remerge multiple times to induce rapid chaotic mixing [64].

Within specific bifurcating mixers, the microchannel comprises a series of circular toroids that subjects the fluids to centrifugal forces to achieve a faster mixing process (Fig.4B) [78].

Finally, the microfluidic mixing through serpentine structures relies on microvortices generated in the fluid stream by the presence of several curvatures within the microchannel that cause a mismatch in the velocity of different portions of the fluid, thus allowing chaotic advection [79, 80] (Fig. 4C).

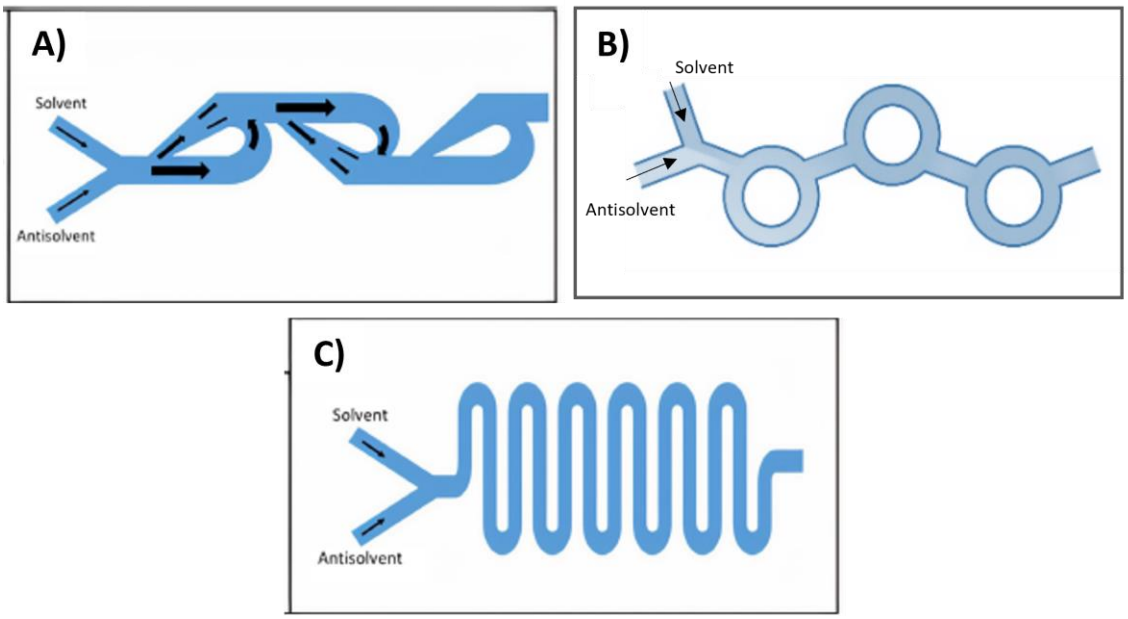

Figure 4: Schematic illustration of microfluidic devices: (A) Tesla mixer, (B) SAR toroid mixer, (C) Serpentine micromixer. From [64] under the Creative Commons Attribution license (https://creativecommons.org/licenses/by/4.0/).

In the active mixing approach, the turbulent flow is generated by external applied forces such as acoustic [81], thermal [82] and electric [83] fields.

The acoustic field-driven method is a versatile technique in which the application of frequencies from 1 kHz to 1 GHz to a simple laminar flow microchannel generates vortices and chaotic advection. Consequently, the so-called “cavitation microstreaming” occurs, due to the collapse of cavitation microbubbles formed at frequencies below 200 kHz [84]. This phenomenon enhances mixing and prevents clogging and NP aggregation and can be achieved through the immersion of microchannels in ultrasonic baths [66, 85] or by using piezoelectric transducers bonded to glass or silicon substrates [86, 87].

In electrical micromixing, instead, the fluid motion is induced by the direct or alternate current applied by electrodes connected to the microchannel. The applied current can cause different types of phenomena: electrohydrodynamics, related to the fluid distinct electrical properties causing electrical stresses at the fluid-fluid interface; alternating current electrothermal effect, involving micro-vortices formed in the channel thanks to the fluid different temperature zones (linked to the alternated current electric field); and direct current-induced thermal buoyancy convection, where mixing is due to the formation of a temperature gradient arising from Joule heating, which triggers a gradient in the electrical properties of the fluid [88]. Also active micromixing was exploited for the formulation of different nanosystems, such as liposomes [61, 89-91], polymeric NPs [71, 92, 93] and several hybrid systems including exosome- and CM-coated polymeric nanosystems [13, 36, 56].

Another aspect where microfluidics was able to improve nanovehicle quality and applicability is drug loading. Paclitaxel, doxorubicin and 5-fluorouracile are just some examples of chemotherapeutics that have been encapsulated into lipidic or polymeric nanosystems by microfluidics [94-97]. Both active and passive micromixing were exploited for the formulation of loaded NPs, achieving enhanced encapsulation efficiency and drug loading compared to bulk methods [98]. Besides traditional chemotherapeutics, microfluidic-generated delivery systems have been widely studied for gene therapy [79, 92]. Within this approach, genetic material such as DNA or RNA are exploited as therapeutics for genetic, acquired and infectious diseases. In nonviral gene delivery vehicles, genetic material is encapsulated into lipid, polypeptide or polymeric NPs to provide a protection from enzymes, thereby extending their lifetime in the blood, and allowing nucleic acids *in vivo* administration [99]. Among the different forms of genetic material, siRNA and mRNA have wide potential for therapeutic and biomedical applications, including bioanalysis, gene silencing, protein replacement and vaccines. Lipid NPs, mainly composed of ionizable or cationic lipids resulted to be the most effective mRNA-vehiculating system, enabling high encapsulation efficiency and effective cytosolic delivery of nucleic acids [100]. It is worth mentioning the successful case of SARS-CoV-2 mRNA-based vaccines BNT162b2 (Pfizer-BioNTech) and mRNA-1273 (Moderna), approved by FDA and EMA, constituting a milestone in gene delivery [101]. The high scale production of these mRNA delivery nanosystems was performed in

continuous with the parallelization of 100 static micromixers, where purified mRNA and lipids were injected, resulting in the precipitation and self-assembly of stable lipid NPs [102].

2. Aim of the project

2. Aim of the project

Traditional artificial NP functionalisation for selective cancer targeting has several drawbacks, including time-consuming and expensive processes, and low final throughput. For this reason, the use of biologically derived materials has attracted attention, combining less laborious procedures for systems preparation with more efficient tumor accumulation, and high biocompatibility [11]. Within this context, the study of exosomes as drug delivery systems constituted a milestone in recent research, allowing on one side to exploit the natural tumor targeting characteristic of these systems, and on the other to load drugs or therapeutic nanomaterials with high efficiency and consequent significant effect *in vitro* and *in vivo* [1]. However, exosome development as drug vehicles has been impaired by the low yield of isolation, the lack of standard procedures for their production and purification and their potential carcinogenicity [103, 104]. Addressing these challenges, as an innovative targeting strategy, cancer CMs direct use for the formulation of anticancer drug vehicles has been implemented in recent research [33, 34]. As thoroughly reported in the previous sections, this approach allowed to inherently reproduce the biological properties of the source cells on the bio-inspired nanosystem and to achieve a broad range of functions, including prolonged circulation, immune escape, and disease-related targeting ability. In the present work, cancer CM-derived vesicles (CMVs) were designed and deeply characterized. An interesting purpose of this work is the separate study of primary glioblastoma (GBM) cells (from biopsies samples) and immortalized colorectal cancer (CRC) cells from a murine cell line, as CM sources. Two types of systems were differently developed: “pure” CM-derived vesicles (CMVs) were obtained by assembling isolated cell membranes from GBM and CRC cancer cells, whereas CRC-CM fusion with synthetic lipids was performed to produce hybrid vesicles. The challenge addressed with membrane hybridization was to retain CM characteristic proteins and phospholipids and to embed them into a synthetic lipidic bilayer aiming to produce a tunable and standardly reproducible platform for drug delivery. The final purpose of the study was to demonstrate the role of CM decoration in cell affinity and internalization and to design a high throughput, standardizable and scalable procedure for the preparation of a potential cell-derived drug vehicle for cancer treatment.

3. Cell membrane-derived vesicles (CMVs) from glioblastoma cells

3. Cell membrane-derived vesicles (CMVs) from glioblastoma cells

3.1. Introduction

3.1.1. Glioblastoma (GBM): prognosis and treatment

GBM is a malignant astrocytic tumour, preferentially located in the cerebral hemispheres. It constitutes 25% of all malignant nervous system tumors and its prognosis is very poor, with a relative survival for adults of less than 30% at one year, 5% at three years, and 3% at five years, with no difference between men and women [105, 106]. Although no prevention screening is available so far, known risk factors for primary brain tumours include exposure to therapeutic ionising radiation, employment in synthetic rubber manufacturing, and exposure to vinyl chloride or pesticides. Several researches reported increased risk of developing brain tumours in patients who had undergone irradiation for leukaemia as children, identifying therapeutic ionising radiation as a strong risk factor [107]. The 2021 WHO classification recognizes three subtypes of GBM: gliosarcoma, giant cell GBM, and epithelioid cell GBM [108]. All subtypes are characterized by the presence of poorly differentiated neoplastic astrocytes exhibiting cellular polymorphism, nuclear atypia and mitotic activity, generally endowed with regional heterogeneity and highly invasive growth. Histopathological and diagnostic features are also vascular thrombosis, microvascular proliferation and necrosis [109]. GBM, which typically affects adults, frequently develops *de novo* without evidence of a less malignant precursor lesion (primary GBM) and is characterized by the loss of phosphatase and tensin homolog (PTEN) and by epidermal growth factor receptor (EGFR) amplification. Alternatively, GBM may mature from diffuse grade II astrocytomas or anaplastic astrocytomas (secondary GBM) and it exhibits alterations in p53, platelet-derived growth factor receptor (PDGF-R) alpha and p16, even if the impact of these alterations on the prognosis has not been clarified yet [110]. Another common mutation characterizing GBM is hypermethylation, with consequent disfunction, of the O6-methylguanine-DNA methyltransferase (MGMT) gene, which is involved in DNA repair and whose expression is associated with drug resistance. Therefore, hypermethylation of the MGMT gene promoter, besides being a valuable predictive marker, is also associated with therapy efficiency and consequent longer overall survival [111].

The most common clinical presentation of GBM at diagnosis is headache and/or nausea in a context of a large tumor or significant edema [112]. An overview of the predominant symptoms leading to a diagnosis is summarized in Figure 5.

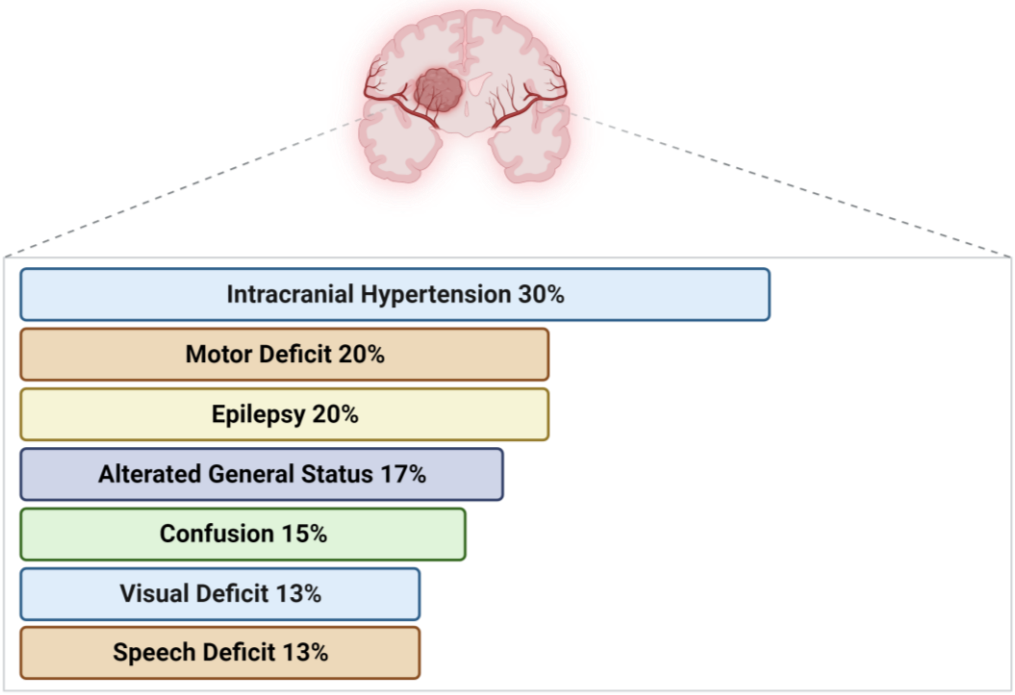

Figure 5: Overview of the main reported clinical presentations in glioblastomas [109]. Created with BioRender.com

Concerning GBM imaging and therapeutic response monitoring, gadolinium-enhanced magnetic resonance imaging (MRI), magnetic resonance spectroscopy (MRS) and [F18]-fluorodeoxyglucose-positron emission tomography (FDG-PET) are the most widespread techniques [110]. Typical MRI imaging characteristics of glioblastomas consist in infiltrative, heterogeneous, poorly circumscribed intraparenchymal lesions, and display contrast enhancement at their margin, evidencing blood–brain barrier disruption [113].

To date, the standard treatment for GBM consists in surgical resection, which is frequently uncomplete given the infiltrative character of the lesion, followed by the association of radiotherapy and temozolomide. However, the frequently observed tumor recurrence is mainly due to treatment resistance, indicating that new strategies are needed to improve radiotherapy and chemotherapy association efficacy. Resistance to radiotherapy was discovered to be related to the presence of a sub-population of self-renewing and pluripotent GBM stem cells within the tumor [114]. These surprisingly

numerous stem cells can overcome the damage of chemo- and radio-therapy through adaptive resistance pathways, representing a good pharmacological target for more effective GBM therapies [115].

3.1.2. Boron neutron capture therapy (BNCT)

Boron neutron capture therapy (BNCT) is a selective and low-invasive cancer radiotherapy that relies on the neutron capture-fission response occurring when the steady isotope boron-10 (^{10}B) is irradiated and converted to unstable ^{11}B (Fig. 6). The therapeutic effect is due to the consequent release of a high-linear energy transfer of alpha particles (^{4}He), lithium-7 ions (^{7}Li), and gamma radiations, from a sufficient amount of ^{11}B [116]. The neutrons used for ^{10}B irradiation can be low-energy (0.025 eV) thermal neutrons or, for clinical applications, higher energy epithermal neutrons (10000 eV), which manage to penetrate thick tissues and the skull, a critical feature for BNCT success. The very short path lengths of alpha particles (5–9 μm) allow to selectively damage the boron-containing cells, making this technique sufficiently safe and minimally invasive [117]. However, to be effective, a selective accumulation of ^{10}B in the tumor is needed: about 20 μg of ^{10}B per gram of tumor tissue (or 10^9 atoms/cell) have to be selectively delivered to the tumor, while a sufficient dose of neutrons must penetrate and be absorbed by the cells to initiate the fission reaction [116].

For this reason, a strategy for increasing the selective uptake of boron-carrying agents into cancer cells is a solid need. An ideal BNCT delivery agent is characterized by high tumor uptake, low intrinsic toxicity, and minimal normal tissue uptake, possibly featuring tumor/normal tissue and tumor/blood boron concentration higher than 3. Another important requirement is sufficient persistence in the tumor (more than one hour) and relatively rapid clearance from blood and normal tissues [118]. To date, the clinically used ^{10}B carriers in BNCT are sodium mercapto-undecahydro-closo-dodecaborate ($Na_2B_{12}H_{11}SH$), known as sodium borocaptate (BSH), and (L)-4-dihydroxyborylphenylalanine, commonly known as boronophenylalanine (BPA). BSH is an anionic polyhedral borane icosahedron used in clinical trials preferentially for the treatment of GBM and other high-grade gliomas. BPA is a boron-containing amino acid with low water solubility, administered in clinic as a complex with fructose, which significantly increases its aqueous solubility at physiological pH [119]. As already reported in several works published at the beginning of the century, this compound is able to preferentially accumulate in tumor tissues, justifying its use in clinical trials for the treatment of GBM [120, 121], meningiomas [122], head and neck tumors [123, 124], melanoma [125] and hepatocellular carcinoma [126]. Moreover, it is noteworthy that

boron agents are efficiently internalized by GBM stem cells, which further proves the high clinical potentiality of BNCT for the treatment of this pathology [127]. Nevertheless, the limited tumor/normal tissue ratios of boron accumulation, in patients treated with BPA-fructose complex and BSH, still impairs BNCT application for cancer treatment. For this reason, new strategies for the selective delivery of high amounts of boron are needed, and the development of nanosized boron delivery agents could be a promising approach. Different types of nanosystems have been recently designed aiming to encapsulate elemental boron or boron-carrying molecules, including liposomes and iron oxide, gold, silica and polymeric NPs [118].

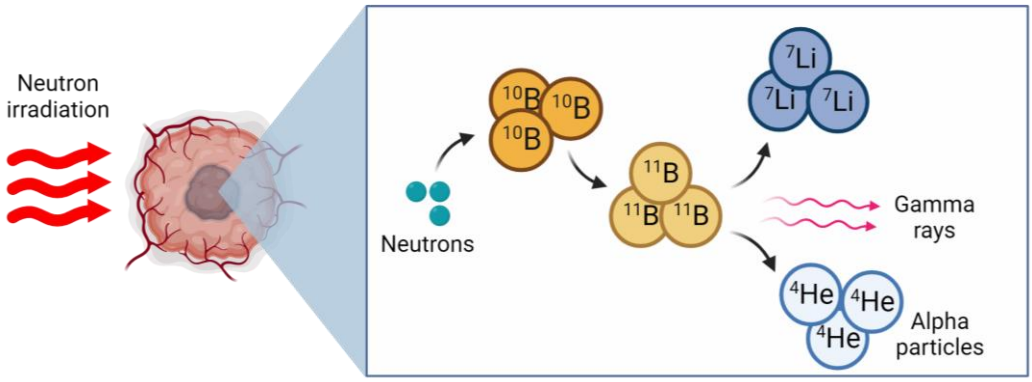

Figure 6: Schematic representation of BNCT mechanism. Created with BioRender.com

3.2. Materials and methods

3.2.1. Cell cultures

Human GBM cells were isolated from postsurgical specimens of patients who underwent surgery at IRCCS Ospedale Policlinico San Martino in Genoa, with informed consent using the guidelines approved by the Institutional Ethical Committee. Cells were cultured in EndoGRO-LS Complete Culture Media Kit (Sigma-Aldrich, USA) and seeded on attachment factor-coated plates. Human glial oligodendrocytic hybrid cell line M03.13 (Tebu-Bio, France) with a normal oligodendrocyte and astrocyte phenotype [128] was maintained in Dulbecco's Modified Eagle Medium (DMEM) containing 15% fetal bovine serum (FBS), 1% penicillin/streptomycin, 1% glutamine (all from Gibco, Thermo Fisher, USA). M03.13 were differentiated for five days in 100 nM phorbol 12-myristate 13-acetate (PMA, Sigma-Aldrich, USA) and 1% FBS complete medium prior to the treatment.

3.2.2. BPA and BPA-fructose complex solutions preparation

BPA (Sigma-Aldrich, USA) containing naturally occurring and stable isotopes, ^{11}B (80.1 %) and ^{10}B (19.9 %), was used for economical reason instead of ^{10}B-enriched molecules (> 90%), which will be necessary in the phase of thermal neutron irradiation tests.

An accurately weighed amount of BPA L-isomer was suspended in methanol (1 mg/mL) by vigorous stirring and sonication. BPA solubilization in water was achieved through the formation of a complex with fructose (Sigma-Aldrich, USA) indicated as BPA-fr, combining BPA with a 10 % molar excess of fructose in Milli-Q water. 1 M NaOH aqueous solution was carefully added to the suspension until BPA was completely solubilized (around pH 9). Then, pH neutralization was performed by slowly adding 0.1 M HCl aqueous solution. The pH was monitored after each HCl addition, obtaining a 6.5 mg/mL complex solution at pH 7.4; the concentration is expressed as BPA weight on total solution volume.

3.2.3. CMVs and liposomes preparation and purification

To prepare monodispersed nanosized CMVs, 2-2.5 x 10^7 GBM cells were homogenized on ice for 100 downstrokes (Dounce manual homogenizer, VWR, Italy) in homogenizing buffer at pH 7.4. The homogenizing buffer had the following composition: 225 mM mannitol (Sigma-Aldrich, USA), 75 mM sucrose (Sigma-Aldrich, USA), 0.5% w/v BSA, 0.5 mM EGTA, 30 mM tris-HCl, 5 µL/mL protease inhibitor cocktail and 1% v/v phosphatase

inhibitor cocktail (all from Thermo Fisher, USA). The homogenate underwent a differential centrifugation procedure using a Beckman Coulter J2-Avnati J-30 I centrifuge (Beckman Coulter, USA) : firstly, it was centrifuged at 800 x g for 5 min at 4 °C; the pellet was discarded, and the supernatant was centrifuged again for 5 min at 800 x g and 4 °C and then for 10 min at 10000 x g and 4 °C; the supernatant was collected again and centrifuged for 20 min at 25000 x g and 4 °C to obtain the crude membrane fraction as a pellet. The pellet was resuspended in a buffer composed of 225 mM mannitol, 75 mM sucrose, 30 mM tris-HCl, pH 7.4 (henceforth indicated as starting buffer) and centrifuged again for 20 min at 25000 x g and 4 °C to remove microsomal and cytosolic contamination; this last step was repeated twice. Two further pellet washings were carried out with physiologic saline solution (0.9 % NaCl). The obtained purified plasma membranes were resuspended in a calculated volume of Milli-Q water or PBS (Thermo Fisher, USA) and extruded through polycarbonate filters with decreasing pore size (400 – 200 – 100 nm, 20 passages each) using a LiposoFast Basic pneumatic extruder (Avestin, Canada) set at 4 bar, immersed in a thermostated water bath at 37 °C. Fluorescent labelling of CMVs was performed by resuspending the CM pellet with an appropriate volume of a 2 nmol/mL 1,1'-dioctadecyl-3,3,3',3'-tetramethylindocarbocyanine iodide (CM-DiI) ethanolic solution ($\lambda_{exc/em}$ =550/570 nm) (Thermos Fisher, USA). After vigorous stirring, ethanol was evaporated under N_2 flux at RT, and the obtained labelled pellet was hydrated and extruded as previously described.

For liposomes formulation, stock solutions of 1,2-distearoyl-sn-glycero-3-phosphocholine (DSPC) (Avanti Polar Lipids, USA), 1,2-distearoyl-sn-glycero-3-phosphoethanolamine-N-[methoxy(polyethylene glycol)-2000] (ammonium salt) (DSPE-PEG2000) (Nanocs, USA) and cholesterol ≥ 99% (Sigma-Aldrich, USA) were prepared by dissolving appropriate amounts of lipid powders in chloroform. Then, calculated volumes of stock solutions (final lipid ratio of 52:45:3 mol% DSPC:cholesterol:DSPE-PEG2000) were mixed in a round-bottom flask and dried in a rotary evaporator under reduced pressure.

To prepare blank liposomes, after removal of the organic solvent, the resulting lipid film was hydrated with an appropriate volume of Milli-Q water or PBS, to obtain a final lipid concentration of 10 mM, in a thermostated bath at 58 °C for 2 h. The obtained multilamellar vesicles were extruded, using the pneumatic extruded mentioned above,

through polycarbonate filters with decreasing pore size (400 – 200 – 100 nm, 20 passages each) at 58 °C and 4 bar.

Fluorescently labelled liposomes were obtained by adding an appropriate volume of a 95 nmol/mL CM-DiI ethanolic solution to the organic mixture prior to film formation.

For the preparation of BPA-loaded liposomes (Lipo BPA), 1.5 mL of a 1 mg/mL BPA solution in methanol were added to the organic lipid mixture composed of 10 µmol of lipids, prior to lipid film formation. After organic solvent evaporation, the film was hydrated with Milli-Q water for a final lipid concentration of 10 mM, and the obtained multilamellar vesicles were extruded as reported above. BPA-fr-loaded liposomes (Lipo BPA-fr) were obtained by hydrating the lipid film from 15 µmol lipids with 1.5 mL of a 6.25 mg/mL BPA-fructose complex solution in Milli-Q water, followed by extrusion performed as reported for the previous formulations.

Vesicles suspensions were purified by semipreparative HPLC through size exclusion chromatography (SEC) with refractive index (RI) and UV detector. The TSKgel G6000pw chromatographic column (i.d. 7.5 mm, length 30 cm) (Tosoh Bioscience, Japan) was thermostated at 30 °C; injection volume was 400 µL; isocratic elution was performed with 1 mL/min Milli-Q water. RI detector sensitivity was set at a value of 64, with a time constant of 1, and the detection cell was thermostated at 30 °C; UV detector was set at 210 - 220 - 280 nm wavelengths. The injections were performed using a 500 µL loop, using the partial loop-fill injection method. HPLC data were analysed by Waters Empower™ 3 software. Prior to HPLC purification of Lipo BPA-fr, part of the unencapsulated BPA-fructose was removed through centrifugation on 100 kDa membrane filters at 1000 rpm for 20 min, in order to avoid pressure issues on the HPLC system, due to the high viscosity of BPA-fr solution.

The purified liposomes were lyophilized prior to ICP-AES analysis for B quantification.

3.2.4. CMVs and liposomes characterization

Dynamic Light Scattering (DLS): Hydrodynamic diameter, polydispersity index and Z potential of the nanosystems were determined by DLS (Zetasizer HSa 3000, Malvern, UK). To carry out the size measurement, 30 µL of liposomal suspension were diluted to the final volume of 3 mL with 0.01 N NaCl aqueous solution, while the extruded CMVs were analysed without further dilution. The average hydrodynamic diameter value was obtained from three measurements (10 sub runs each) with the software firstly acquiring

the signal in NNLS (non-negative least squares) mode, then re-elaborating it through the CONTIN algorithm. The Z potential was determined through an electrophoretic mobility measurement on the samples diluted as described for size analysis, and was expressed as mean value of 5 measurements.

Nanoparticle Tracking Analysis (NTA): Vesicle concentration was studied by NTA (NanoSight NS300, Malvern, UK). The particle suspensions were diluted with Milli-Q water to a suitable concentration for a correct analysis (1:200-1:500 dilution for CMVs and 1:10000- 1:100000 for liposomes) and a 488 nm laser was used to detect the particles in scattering mode. The yield of the process for CMVs production was defined as the number of final vesicles obtained per initial cell, calculated with the following equation:

Yield = number of final vesicles/number of initial cells homogenized

Transmission Electron Microscopy (TEM): For TEM observations, different aliquots of CMVs were concentrated under a N_2 flux for 2 h at RT, and observed using a Hitachi HT7800 transmission electron microscope equipped with a Megaview 3 digital camera (HITACHI, Japan) and Radius software. 20 µL of 2% paraformaldehyde in 0.1 M phosphate buffer (pH 7.4) were added to 20 µL of vesicle suspension in starting buffer; the vesicles were then adsorbed for 20 min to formvar-carbon coated copper grids by floating the grids on 5 µL drops on parafilm. Subsequently, the grids were rinsed in phosphate buffer and negatively stained with 2% uranyl acetate for 5 min at RT. Stained grids were embedded in 2.5% methylcellulose for improved preservation and air dried before examination.

Atomic Force Microscopy (AFM): Morphology and elasticity of CMVs were investigated through AFM. The support for CMVs was prepared by covering a 35 mm glass coverslip with a 10 µg/mL polylysine solution. After 20 min incubation, the surface of the coverslip was allowed to dry at RT for 1 h. 30 µL of an aqueous suspension of CMVs were deposed on the prepared substrate, incubated for 5 min and, afterwards, 70 µL of PBS were added. Measurements were performed with a JPK NanoWizard IV microscope (Bruker, USA) equipped with a DNP-10 probe with nominal elastic constant k=0.06 N/m. Vesicle images were obtained through the "quantitative imaging technique" and Young's modulus (E) was calculated using the JPK Data Processing software. E of CMVs was calculated as mean value measured in 17 different samples.

Proteomic analysis: The protein profile of CMVs was qualitatively characterized through a proteomic analysis. Briefly, the vesicle aqueous suspension was dried under a N_2 flux overnight, resuspended in 50 µL of iST-LYSE buffer (PreOmics, Germany) and lysed for 10 min at 95 °C on a ThermoMixer (Torrey Pines Scientific, USA) at 1000 rpm. The lysed samples were then transferred to a 96-deep well plate and PAC-based protein isolation on magnetic microparticles and digestion were automated on a KingFisher™ Apex magnetic handling station in a 96-well format (Thermo Fisher Scientific, USA). More in detail, acetonitrile-induced protein aggregation was performed to precipitate proteins on beads with a protein/beads ratio of 1:4 (two cycles of 1 min of mixing at medium speed, followed by a 10 min pause each). Sequential washings with acetonitrile, 70% ethanol and isopropanol were carried out for 2.5 min at a slow speed, without releasing the beads from the magnet. The captured proteins were then digested with 100 µL of 25 mM Tris-HCl pH 8, LysC (Fujifilm Wako, USA) and trypsin (Promega, USA) in an enzyme/protein ratio of 1:400 and 1:200 (w/w) for 2.5 h at 37 °C. Once the process was completed, the magnetic beads were removed from the digested samples. The peptide mixtures were acidified using 2% trifluoroacetic acid and separated by liquid chromatography prior to mass (MS) analysis. Briefly, the acidified sample was loaded onto C18 Evotips according to the manufacturer's instructions. Peptides were analyzed on the Evosep One LC system using an EASY spray column (150 µm x 15 cm, Thermo Fisher Scientific, USA) and the pre-programmed gradient of 30 samples per day, with a flow rate of 500 nL/min. The column temperature was maintained at 40 °C and interfaced online with the Orbitrap Exploris 480 MS (Thermo Fisher Scientific, USA) equipped with the FAIMS Pro Duo Interface (Thermo Fisher Scientific, USA). MS analysis was performed in data independent acquisition (DIA) mode. The FAIMS CV was set to -45 at standard resolution. The full MS resolution was set to 120000 in a range between 375 and 1500 m/z, with an AGC target of 300% and the maximum IT set to Auto; the AGC target value for the fragment spectra was set at 1000%; 40 windows of 15 Da were used with an overlap of 1 Da; the normalized collision energy was set at 30%. Raw data were acquired in profile mode using positive polarity. Raw files were processed with Spectronaut version 18[3] using a library-free approach (directDIA). Enzymes/Cleavage Rules were set to trypsin/P, LysC. The library was generated against the UniProt Homo Sapiens Taxonomy ID 9606 database (released November 2022). The FDR of PTMs and

peptide/protein groups were set to 0.01. For the quantification precursor, filtering was set to Identified (Qvalue) and MS2 was chosen as quantity MS level. The protein report generated by Spectronaut was imported into the Perseus software version 1.6.15.0[4] for statistical analysis. UniProt database was employed for the study of protein function and characteristics.

Immunofluorescence study on CMVs: The presence of the membrane protein Annexin A2 on the CMVs surface, identified with the proteomic analysis, was also confirmed by an immunofluorescence study on DiI-labelled CMVs. Briefly, DiI-CMVs were incubated with a 1:200 dilution in PBS of Alexa Fluor® 488-labelled rabbit anti-annexin A2 antibody (Abcam, UK) overnight at 4 °C. Unbound antibodies were removed by ultracentrifugation: the mixture suspension was centrifuged for 20 min at 25000g and 4 °C; after discarding the supernatant, the pellet was washed twice with PBS and finally resuspended in PBS, and a suspension drop was observed with confocal microscope (A Stellaris8 Falcon TauSTED, Leica Microsystems, Germany) at 520 nm for Alexa Fluor® 488 and 570 nm for DiI.

Nucleic acid electrophoresis: DNA or RNA presence in the purified CM fraction was investigated by agarose gel electrophoresis. Briefly, agarose gel 1% was prepared by heating an agarose suspension in 1x TBE filtered buffer (Tris/boric acid/EDTA buffer) (Invitrogen™, Thermo Fisher, USA); the agarose solution in buffer was allowed to cool down at RT and ethidium bromide gel stain (Bio-Rad, USA) was added. The mixture was poured in the gel stamp and allowed to polymerize at RT for 30 min. The samples were mixed with a gel loading buffer (18 µL sample suspension + 2 µL gel loading buffer) and loaded into gel wells; the electrophoretic run was performed at 80 V for 40 min in TBE running buffer. The gels were imaged by GelDoc imaging system (Bio-Rad, USA).

3.2.5. Boron loading evaluation: ICP-AES analysis

Lyophilized samples were dissolved in 3 mL of methanol, transferred to Teflon containers to avoid any boron contamination from glass, and dried at 90 °C under N_2 flux. 40 µL of standard solution of yttrium (1000 ppm) were added as internal standard and the mixture was digested with 3 mL of 65% (m/m) nitric acid (for trace metal analysis) at 160 °C for 6 h. After cooling at RT, the solutions were diluted to 10 mL with ultra-pure water (>18 MOhm cm, Puranity TU3+, VWR International). BPA concentration in digested purified liposomal samples were measured by ICP-AES using an iCAP 7000 Series

(Thermo Fisher Scientific, USA) with axial plasma view for better sensitivity. For B quantification, a three-point calibration was carried out using 1000 µg/mL boron ICP Standard Solutions. The emission line chosen was 249.773 nm. Blank liposomes were also digested and analysed in order to detect any matrix-related signal.

Final BPA concentration in the purified samples was determined and encapsulation efficiency (EE%) and drug loading % were calculated using the following equations:

$$EE\% = (w_t/w_i) \times 100$$

where w_t is the amount of boronated agent found in the purified liposomal suspension and w_i is the amount of BPA initially added for loading;

$$\text{Drug loading } \% = (w_d/w_f) \times 100$$

where w_d is the amount of boronated agent found in the purified liposomal suspension, and w_f is the final weight of the lyophilized formulation.

For ICP-AES recovery study, lyophilized blank liposomes were dissolved in methanol, dried as described above, and spiked with an accurately measured volume of BPA or BPA-fr solution. The obtained mixtures were digested and analysed as already described. The recovery results were expressed as the BPA detected ratio on the initial drug used for sample spiking, according to the following equation:

$$\text{Recovery } \% = (w_t/w_i) \times 100$$

where w_t is the amount of boronated agent found in the sample and w_i is the amount of BPA added for matrix spiking.

3.2.6. *In vitro* internalization study: confocal microscopy, FACS

Confocal microscopy: Confocal microscopy was used to observe the internalization of fluorescently labelled CMVs into GBM parent and heterologous cells (i.e., GBM cells deriving from a different patient), and healthy oligodendrocytes. To this aim, 10000–15000 human GBM cells or oligodendrocytes were cultured for 24 h at 37 °C in 5% CO_2 environment. Cells were stained with CellMask™ Green Plasma Membrane Stain (Invitrogen™, Thermo Fisher, USA) for 15 min at 37 °C; after removal of the cell staining solution, the cells were treated with 1.3 mL of DiI-CMVs suspension in PBS (approx. 6.1 × 10^9 particles/mL) or with 1.3 mL of a DiI-liposome dispersion previously diluted to obtain approximately the same nanoparticle concentration. Incubations were carried out for 15 and 30 min; after removal of the CMVs or liposome suspensions, the cells were

added with 1 mL of PBS and imaged by a A Stellaris8 Falcon TauSTED (Leica Microsystems, Germany), operating as confocal microscope with a 100x objective /1.40 NA. The desired excitation wavelengths were chosen using a white light laser (λ = 488 nm for CellMask™ and λ = 561 nm for CM-Dil). The time of measurement was kept below 2 h for each Petri dish.

Fluorescence-Activated Cell Sorting (FACS) analysis: Internalization of CMVs and liposomes into parent and heterologous GBM cells and healthy oligodendrocytes was quantitatively investigated at two time points by flow cytometry. 250000 GBM cells per well were seeded in 60 mm Petri dishes, cultured for 24 h and then treated with 3 mL particle suspensions in complete medium at a final concentration of 5.5 x 10^8 particles/mL. The cells were incubated with the fluorescently labelled CMVs or liposomes for 2 h and overnight at 37 °C. Afterwards, the nanoparticle suspension was removed, and the cells were washed with PBS, detached with trypsin-EDTA solution, washed with PBS and read with CytoFLEX S Flow Cytometer (Beckman Coulter, USA), excluding the dead ones from the analysis. Data analysis was done using FlowJo software X (BD, USA).

3.2.7. *In vitro* cytotoxicity study

In vitro toxicity of CMVs was evaluated on parent and heterologous GBM cells and healthy oligodendrocytes by assessing the reduction of MTT reagent (3-(4,5-dimethylthiazol-2-yl)-2,5-diphenyl-2H-tetrazolium bromide). 3000 cells/well were plated in 96-well plates and treated with CMVs at two different concentrations: 4 x 10^9 or 8 x 10^9 particles/mL; untreated control cells were maintained in medium at the same conditions. After 24 or 48 h of incubation with CMVs, the cells were washed with PBS and MTT (2.5 mg/mL in PBS) was added and allowed to react for 2 h at 37 °C in a 5% CO_2 atmosphere. The violet-blue water-insoluble formazan crystals produced by MTT reduction were solubilized with dimethyl sulfoxide and the absorbance was measured with a BioTek ELx800 microplate reader (Agilent Technologies, USA) at 570 nm. The signal of treated samples was related to untreated control cells to calculate cell viability expressed as percentage.

3.3. Results and discussion

3.3.1. Preparation and characterization of CMVs from GBM primary cells

GBM cells homogenate underwent a differential centrifugation procedure aiming to isolate the membrane fraction, and to remove cytosolic components. The CM isolation protocol was designed adapting the procedure described by J. M. Suski et al. in [129]. As indicated by the authors, with the first low speed centrifugations (800 x g), nuclei and unbroken cells were removed as pellet, while the higher speed centrifugations (10000 and 25000 x g) were performed to isolate CMs from the mitochondrial fraction and from cytosol and microsomes, respectively (Fig. 7).

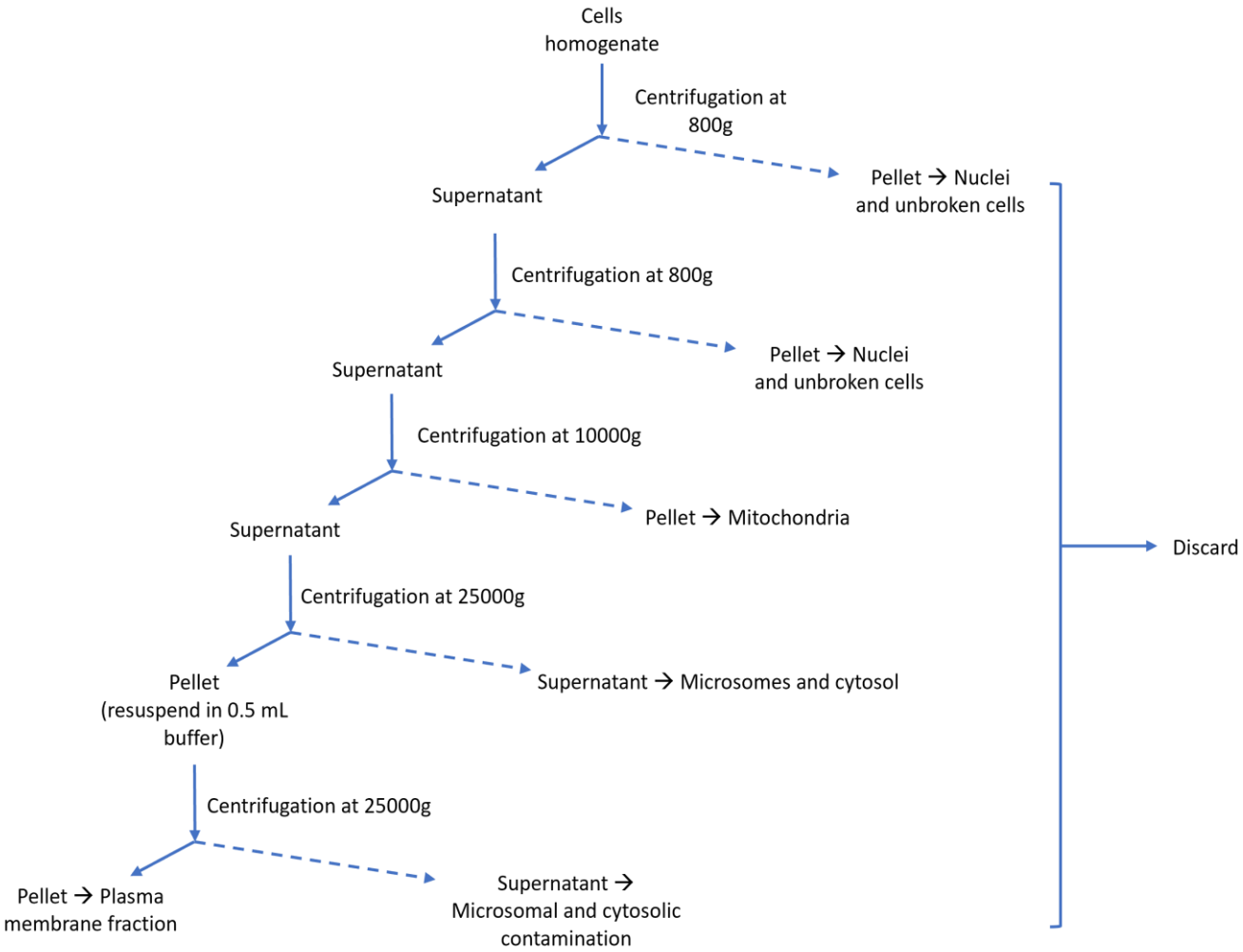

Figure 7: Schematic representation of CM isolation process

Once obtained the purified membrane fragments, they were resuspended in Milli-Q water or PBS and extruded through polycarbonate filters of decreasing pore size to obtain CM-derived nanovesicles.

CMVs were characterized in terms of size, PDI and Z potential by DLS; the results are summarized in Table 1. They resulted in a monodisperse population of nanovesicles of about 125 nm with a negative surface charge. Negative Z potential, besides favouring nanovesicle stability, confirmed the maintenance of the surface charge characterizing the CMs, which are known to carry a negatively charged network of glycosylated proteins intercalated within the lipid bilayer, in turns comprising negatively charged phospholipids [130].

	Size (nm)	**PDI**	**Z potential (mV)**	**Concentration (particles/mL)**	**Yield (x 10^3)**
CMVs	125 ± 7	0.13 ± 0.05	-23 ± 4	8 ± 3 x 10^{10}	3.0 ± 0.9

Table 1: Physico-chemical properties of CMVs from GBM primary cells. Mean values ± standard deviation (n=5).

Moreover, nanoparticle tracking analysis was used to measure the number of CMVs in 900 µL of final suspension obtained from 2 – 2.5 x 10^7 GBM cells. NTA provides a combined analysis of Brownian motion via light scattering to count and size nanoparticles in a liquid suspension [131]. In this analysis, particles in suspension were injected in a flow chamber and irradiated using a laser source. A syringe pump was used to slowly push particle suspension through the chamber to better analyse single particles in the sample compared to one static field of view [132]. The light scattering produced by the nanostructures was collected by a 20x microscope objective and was recorded with a digital camera (Fig. 8A). NTA software analysed particles individually and simultaneously, and, by using the Stokes-Einstein equation, calculated their hydrodynamic diameters (Fig. 8B).

Despite NTA is currently considered to be the best method available for measuring the concentration of nanosystem suspensions, this technique requires specific precautions: to obtain accurate and reproducible size distribution and concentration data, it is important to dilute the nanoparticle suspension to a concentration of ~10^7-10^9

particles/mL, which is the suitable range for Nanosight instruments operations; moreover, camera level and detection threshold settings must be accurately configurated and standardized to minimize potential variability and artefacts.

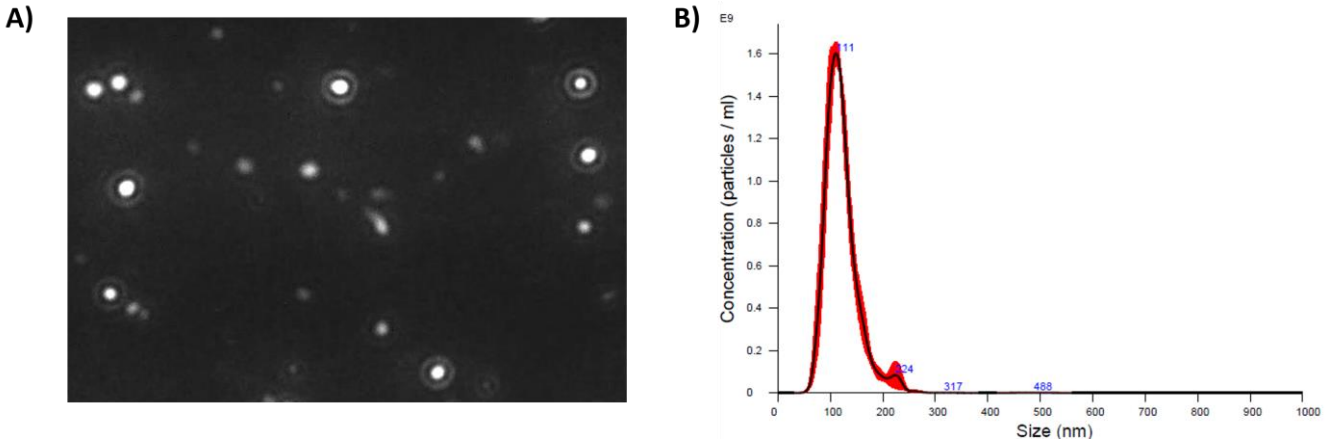

Figure 8: (A) NTA digital camera live image and (B) size distribution of CMVs in water suspension, dilution 1:250.

From this measurement, the concentration of the final CMVs suspension, obtained from around 2 x 10^7 cells and with a final volume of 0.9 mL, was determined, and the yield of the production process was calculated as the ratio of the final number of obtained vesicles on the number of initial GBM cells. The number of obtained CMVs, thus the yield of the production process, resulted slightly higher, compared to data reported in the literature for exosome isolation. Indeed, exosomes undergoing different isolation procedures are frequently found in concentrations ranging from 4 × 10^{10} to 8 × 10^{10} particles/mL in final suspension [133, 134]. However, an appropriate comparison between the developed CMVs and exosomes is difficult to make because of some issues related to exosome extraction. First, exosome production yield is strictly dependent on the different isolation technique employed, resulting in high variability of data published [135]; secondly, a measured number of starting cells or volume of biological fluid for exosome extraction would rather be defined, to give an accurate description of vesicle throughput, otherwise a comparison with CM-derived vesicles might be misleading; lastly, it is common knowledge that exosome extraction procedures are not able to ensure exosome purity and their isolation from structures of approximately the same dimension; this might justify an overestimation of exosome concentration in the extracted fraction [1].

TEM analysis was performed on a concentrated aliquot of CMVs to assess their morphology. TEM micrographs allowed to observe round-shaped unilamellar nanovesicles delimited by a phospholipid bilayer (Fig. 9). The deformed conditions of the vesicles observed in TEM images indicates CMVs collapse, which is a common consequence of the steps of staining and air drying applied to lipid vesicles for sample preparation [136]. Moreover, during acquisition, the sample is exposed to vacuum, potentially inducing distortion, or alteration of the vesicle structures. Deformation phenomena occur more frequently when the sample is composed by soft nano-objects, as in the case of CMVs [137].

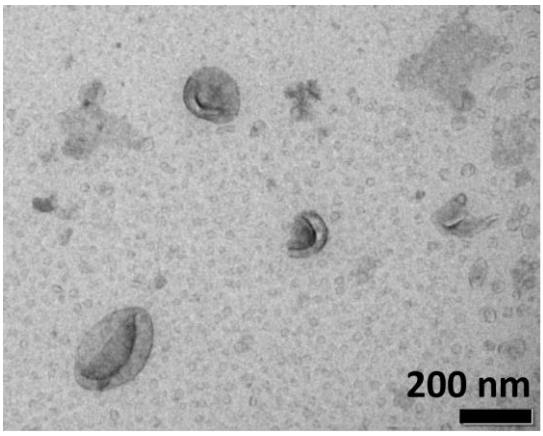

Figure 9: TEM micrograph of CMVs.

The surface morphology and physical characteristics of CMVs were further studied by AFM.

This microscopy technique relies on the fluctuations of a contacting mechanical probe to produce details on the morphology and on the elasticity of an analysed sample. Briefly, a cantilever with a sharp tip (R_c = 5-15 nm) approaches the surface of the object, thanks to attractive forces between the surface and the tip, and, as the cantilever is brought in contact with the sample surface, increasingly repulsive forces induce a deflection of the tip [138]. These deflections are detected by a position-sensitive photo diode (PSPD), which tracks the different directions of a reflected laser beam, incident on the cantilever (Fig. 10A). Thus, if an AFM tip passes over a region of interest, scanning a substrate surface and encountering different objects, the features of the sample result in cantilever deflection (and the subsequent change in direction of reflected beam), recorded by the PSPD. The collected data on the forces that the sample imposes on the

tip can be used to form an image of the three-dimensional shape (topography) of a sample surface or measure its elasticity [139].

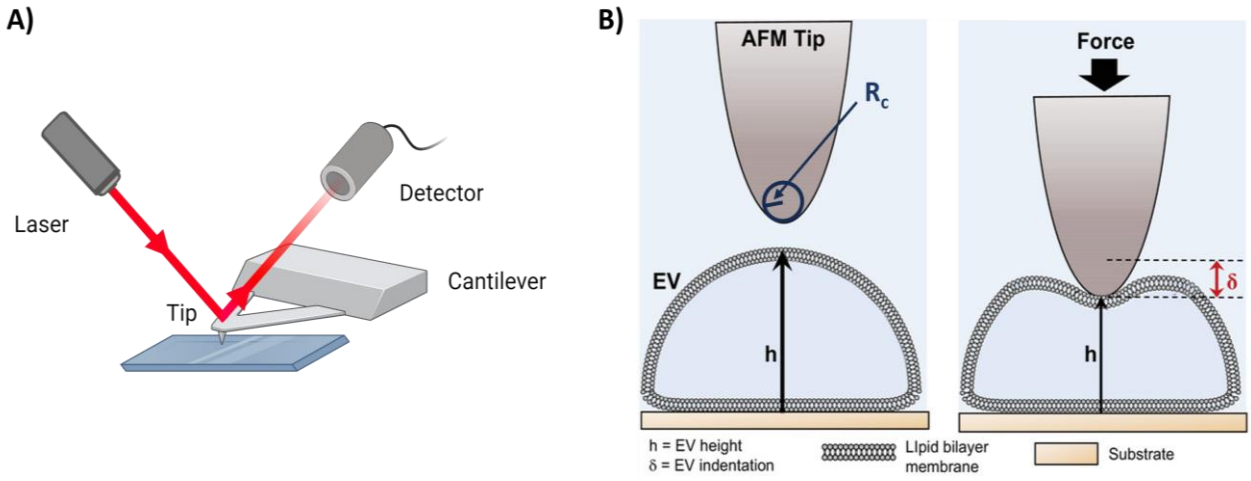

Figure 10: AFM technology. (A) Theoretic principles of AFM and (B) Representation of EVs mechanical features during AFM measurements: the spherical shape of EVs in suspension is modified when it adheres to the substrate, assuming a hemispherical shape (first h variation) and again when it is indented by the AFM tip, which deforms the lipid bilayer, inducing a second h variation of a factor δ (indentation depth). Reproduced from [139] under the Creative Commons Attribution 4.0 International License.

The elasticity, defined as the ability of a material to return to its original state after an exposure to stress, was described for CMVs using the Young's modulus (E) using the following equation:

$$F = \frac{4}{3}\sqrt{R_c}\frac{E}{1-\nu^2}\delta^{3/2}$$

where F is the applied force, R_c the spherical tip radius, v the Poisson modulus and δ the indentation, namely the difference between the height of the object before and after the force application (Fig. 10B); E quantifies the relationship between the compressive stress applied on a surface per unit area, and the axial proportional deformation, defining the stiffness or the resistance to the strain, characterizing the material.

Different substrates has also been shown to affect vesicle deformation and hence their measurements. For this reason, selecting a support with a convenient affinity for CMVs, is of particular importance. The vesicle-substrate affinity must be not excessively strong

to avoid CMVs structural deformation, as this could make the determination of the initial point of contact between the vesicle and the AFM tip very challenging. Likewise, if the interaction is too weak, objects might not successfully adhere to the surface of analysis, or not enough to withstand the imaging forces [139].

For the elasticity study of CMVs, different substrates were tested: neat glass was found to have extreme affinity for CMVs, resulting unsuitable due to CMVs fusion on its surface, which impaired a precise analysis. Conversely, no CMVs were observed when the imaging was performed using (3-aminopropyl)-triethoxysilane (APTES)-functionalised glass, which evidently did not succeed to retain vesicles on its surface. Finally, poly-lysine functionalization was tested on glass coverslips, resulting in a suitable combination of properties allowing the attachment of a considerable number of CMVs that adhered on the surface, yet avoiding the fusion with the substrate or amongst them.

One of the images obtained for GBM-derived CMVs is reported in Figure 11. Figure 11A is a 2D representation of the morphology of a CMV, while figure 11B is the Young's modulus map. The variation of the elasticity detected by the instrument is here represented as a change in the pixels colour. Indeed, when the stiffness is high as the tip is in contact with the substrate, the reported pixels are paler (orange), while when E decreases and the resistance to the tip is lower, pixels are darker. From this map, a circumscribed area of interest was selected to calculate the mean Young's modulus of the object surface, which resulted E = 580 kPa for this particular specimen. This procedure was repeated for 17 CMVs and the mean E with the SD was calculated, resulting E_{mean} = 687 ± 182 kPa, around 40 folds lower than the E calculated for the substrate (E = 28 ± 12 MPa).

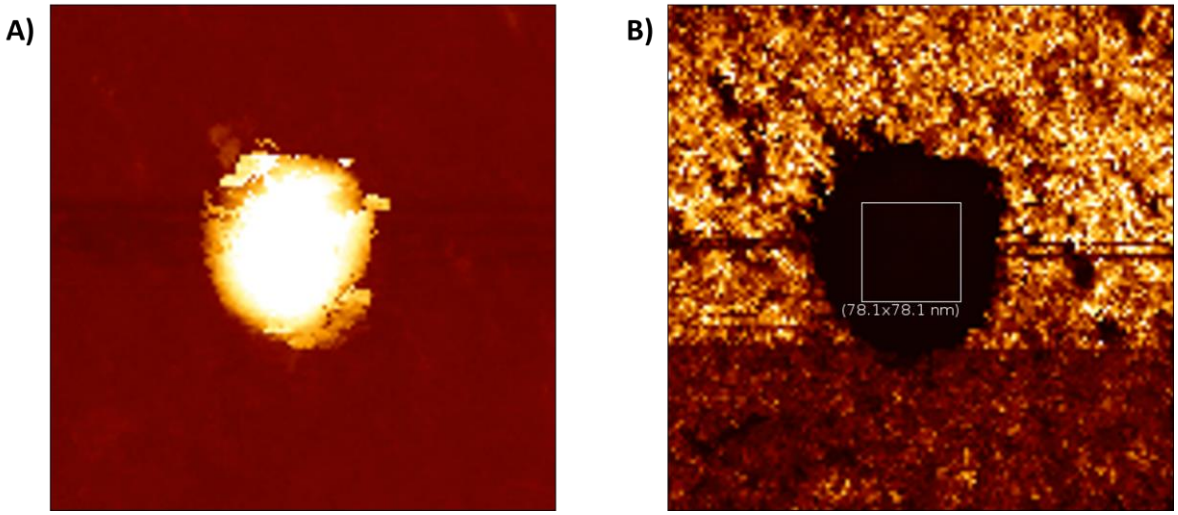

Figure 11: Atomic force microscopy images. (A) Morphologic study of a single CMV, (B) Young's modulus map extracted from AFM results. The square on the CMV surface delimits the considered area for the calculation of the mean E for this sample.

To compare the obtained result to mechanical properties of exosomes, noteworthy is the variability of their elasticity values, related to the different isolation protocol used [140] and to the low selectivity of isolation methods. Indeed, Gazze et al. found that exosomes isolated from hNSC cell line conditioned media had a wide Young's modulus range from 3.7 to 46.1 MPa [140]. Bairamukov et al. observed that small non membranous NPs isolated with exosomes (< 30 nm) exhibited high stiffness as well as large multilamellar EVs, while 30-50 nm vesicles, easily identified as plasma exosomes, were associated with an intermediate Young's modulus of 6.6 ± 0.6 MPa [141]. Despite the high variability of E values reported in literature for endogenous vesicles, CMVs resulted slightly more elastic than exosomes, although this might not affect the suitability of CM-derived vesicles as valid alternatives to naturally secreted EVs.

AFM has been widely applied for exosomes and functionalized liposomes characterization [139, 142], as elasticity and stiffness have been demonstrated to be indicators of their lipidic composition and of the presence of different membrane proteins [143-146]. In particular, Rawicz et al. observed that, in bilayer vesicles composed of phosphatidylcholine (PC) chains, membrane stiffness increased by progressively increasing the length of the saturated/monounsaturated PC chains. This pattern was inverted when two or more cis double bonds were present, resulting in lower stiffness for long chain unsaturated lipids. The authors also evidenced that poly-

cis unsaturated chain bilayers, characterized by lower stiffness, were also thinner and more flexible [143]. Besides the presence of different phospholipids, other solutes included in the membrane might influence vesicle rigidity, as underlined by Dimova et al [144]. Cholesterol resulted to have different effects depending on membrane lipidic composition, although a stiffness increase was observed when inserting this compound into mono-unsaturated lipidic bilayer [147]. Concerning cell membranes, the influence on membrane rigidity of the large number of asymmetrically distributed or anchored biomacromolecules is of particular interest. Different effects have been observed, according to different conformation, orientation and concentration of the several peptides under study [148-150].

When polymers are artificially inserted into synthetic membranes, an increase in vesicle stiffness is induced, according to both a theoretical [151] and an experimental [152] study. Moreover, adsorbed proteins can also have a role on membrane rigidity, as evidenced in the case of avidin binding to biotinylated bilayers, which resulted in an increase in membrane stiffness [153].

In the case of exosomes, Sorkin et al. observed that natural vesicles are generally more elastic than pure lipid liposomes, suggesting that the presence of membrane proteins was important in stiffness lowering, and that the amount of membrane proteins resulted to be the determining factor for this decrease [145].

Even more interestingly, several studies considered the impact of membrane stiffness on the interaction with cells and/or with the cellular environment. Vesicle interaction with host cells might occur through different pathways, most commonly membrane fusion, macropinocytosis and receptor-mediated endocytosis [154]. The single occurring pathway, as well as the efficacy of vesicle internalization, depend upon several factors, including strength of attractive interactions amongst lipids in vesicles and in the CM of host cells, receptor density on the membrane of the host cell, ligand density on vesicle surface, ligand-receptor affinity [155]. However, as pointed out in several studies [154-156], also vesicle elasticity has an impact on their interaction with cells, although a clear definition on the importance and direction of this effect is difficult to extract from the literature. In a theoretical study, Yi et al. evidenced that for a stiff particle the adhesive interaction between the particle and the membrane simply induces the cell membrane to deform and surround the particle. In contrast, for soft particles, the deformation is

partitioned between the particle and the membrane: a very soft particle would initially spread along the cell membrane without significant deformation of the latter. Thus, at a later stage, the cell membrane will be forced to bend around the stretched particle, requiring a more abrupt rise in elastic energy; in contrast, surrounding a rigid particle would involve a gentler increase in elastic energy [154]. Consequently, with less rigid NPs, stronger vesicle-membrane interaction would be necessary to balance the faster rise in elastic energy, as confirmed by the experimental results obtained by Beningo et al. [157]. Also Anselmo et al. supported this hypothesis with *in vivo* biodistribution studies, demonstrating that softer NPs (E = 10 kPa) exhibited longer blood circulation time compared to stiffer ones (E = 3000 kPa), as a result of higher uptake of stiffer NPs from macrophages of the reticuloendothelial system. *In vitro* internalization studies on epithelial, endothelial and macrophage cell cultures, confirmed this hypothesis evidencing higher cellular internalization of more rigid NPs, compared to soft ones [158].

As demonstrated by both a molecular dynamic simulation [155] and experimental data [159], this mechanism described for receptor-mediated endocytic pathway changes when a strong ligand-receptor interaction is implicated: in this case, elastic vesicles deform, acquiring an oblate shape to maximize the ligand–receptor interaction, but, successively, reassume their spherical shape, allowing to bypass the high energy barrier of membrane bending to wrap the oblate vesicle. Therefore, elastic ligand-functionalized vesicles might be internalized in a more efficient way, in comparison with their untargeted rigid counterparts [155].

Considering all the mentioned issues discussed in the literature, a measured stiffness-elasticity balance would be required for an effective drug delivery system: for targeted vesicles a strong ligand-receptor interaction, as well as good elasticity are necessary for an efficient endocytosis, being the higher stiffness related to unspecific uptake and lower blood circulation time.

These studies witness that the characterization of vesicles in terms of mechanical properties is of outmost interest for better understanding their functioning, and constitutes an important parameter for their characterization.

Prior to CMVs formation by CM extrusion, the effective purification of the isolated plasma membrane fraction was assessed by studying the genetic material and proteins retained during the extraction process. DNA or RNA elimination is essential in cancer-derived CMVs, given their potential ability to promote carcinogenesis by delivering genetic material, as already observed for cancer cell-originating exosomes [104]. An agarose gel electrophoresis, which relies on the electric field-driven migration of charged RNA and DNA from a negatively to a positively charged electrode, was performed on the resuspended CM pellet. The starting buffer was used as a negative control, while an aliquot of the unprocessed cell lysate was run as a positive control. As shown in Fig. 12A, a faint band was still detectable in CM isolated following the initial protocol. For this reason, a further pellet washing with the starting buffer (SB) was introduced in the final procedure, resulting in the complete purification from any genetic material contamination (Fig. 12B). Moreover, the resuspended CM was subjected to probe sonication in order to disrupt multilamellar vesicles potentially formed in suspension that might enclose genetic material and hamper its migration, leading to unreliable results. Also in this case, no DNA- or RNA-related absorbance was detected, confirming the previous results (Fig. 12C). This test allowed to ensure the safety of the obtained formulation in terms of DNA- or RNA-derived potential carcinogenesis.

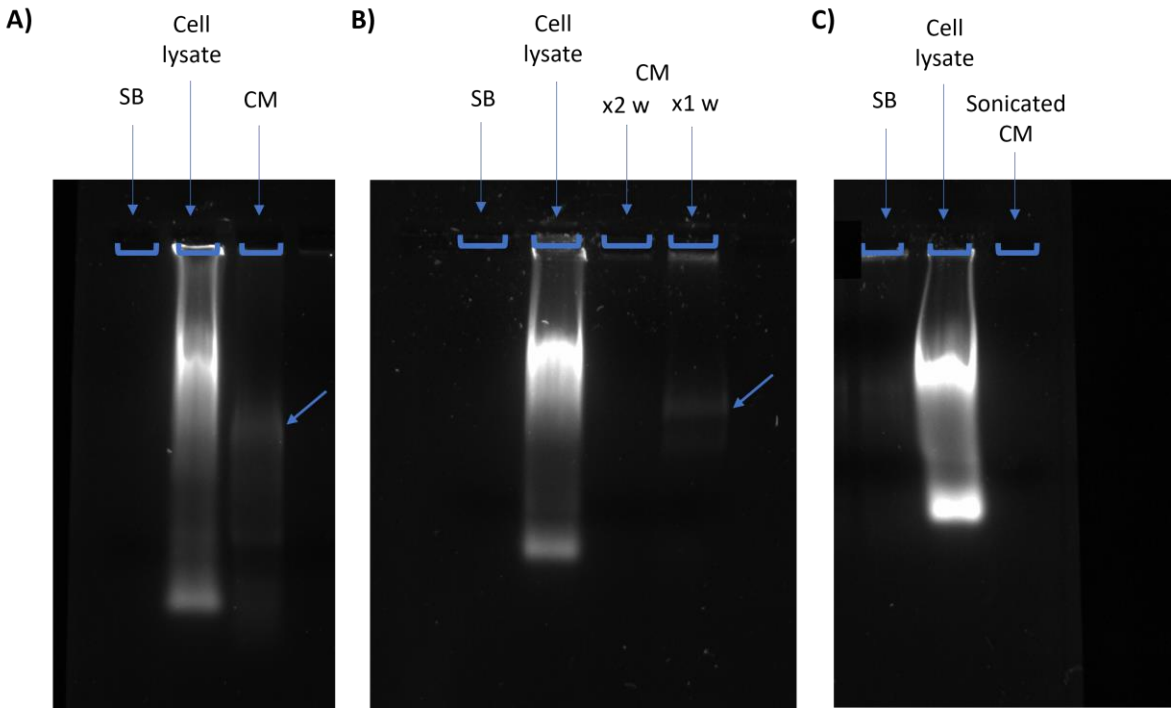

Figure 12: Scan of agarose gel electrophoresis. (A) CM isolated with the initial protocol, (B) two adjacent runs of CM: CM isolated with the initial protocol (x1 w) and undergoing a further washing (x2 w), and (C) probe-sonicated resuspended CM. SB=starting buffer.

Membrane protein retention was assessed by proteomic analysis of CMVs, which allowed not only to prove the presence of a high number of protein groups, but also to qualitatively identify them and consequently to speculate their role in the interaction between CMVs and the host cell, on the basis of their principal functions. In Table 2, the membrane proteins with highest relative abundance are reported; the proteins are associated with the cellular mechanisms in which they are commonly involved, according to UniProt database.

Protein function	**Protein name**	**Gene name**	**Relative abundance (Log_2)**
Immune surveillance escape	Leukocyte surface antigen CD47	CD47	10.11
Cell migration	CD44 antigen	CD44	11.46
	Integrin beta-1	ITGB1	11.21
	HLA class I histocompatibility antigen A	HLA-A	10.76
	CD9 antigen	CD9	10.45
	Neuronal cell adhesion molecule	NRCAM	8.53
	Carbonic anhydrase-9	CA9	7.54
	Pro-neuregulin-1	NRG1	3.91
Promotion of extracellular matrix degradation and invasion	Annexin A2	ANXA2	12.10
	Integrin alpha-3	ITGA3	11.75
	Adipocyte plasma membrane-associated protein	APMAP	9.36

Table 2: Proteomic analysis: some of the most abundant membrane proteins with their encoding genes, their functions, and relative abundances.

Several of the membrane proteins found are reported in the literature as characteristic of GBM cells, like annexin A2 [160], human leukocyte antigen (HLA), class I histocompatibility antigen A and pro-neuregulin-1 [161] and adipocyte plasma membrane-associated protein [162]. Moreover, as shown in the table, the proteomic analysis identified membrane proteins involved in mechanisms related to cancer progression that might have a key implication in malignant cell targeting and immune escape ability of CMVs.

The most abundant membrane protein found in my CMVs sample was annexin A2, a calcium-binding protein expressed on the surface of macrophages, mononuclear cells, endothelial cells, and several types of cancer cells [163]. The expression of this protein has been associated with cell dissemination and metastasis in many cancer types, and several studies positively correlated annexin A2 overexpression in GBM cells with tumor aggressiveness and progression. The overexpression of annexin A2 has been associated to enhanced cell invasion, angiogenesis, proliferation, matrix invasion and mesenchymal transition [164, 165], and Zhai et al. [166] observed that knockdown of annexin A2 decreased glioma cell migration *in vitro* and slowed tumor progression *in vivo*.

To thoroughly investigate whether the proteins retained in CMVs could be actually implicated in the interaction with the host cell, their exposition on the outer surface of the vesicles must be demonstrated. Indeed, given their hydrophilic/lipophilic nature, proteins might remain enclosed in the aqueous core of CMVs or included in the phospholipid bilayer with their active domain oriented towards the inner side of the membrane.

Annexin A2 was selected for this spatial orientation study, given its high relative abundance in the sample and its representative role in GBM cell-to-cell signalling. Confocal microscopy was used to observe the colocalization of fluorescently labelled CMVs with a fluorescent anti-Annexin A2 antibody, demonstrating the effective binding of the antibody with the active domain on the outer surface of CMVs. As shown in Fig. 13, a good level of colocalization of the two probes was observed as yellow colour, resulting from the merge of red (CM-DiI-labelled vesicles) and green (Alexa Fluor® 488-labelled antibody) signal.

This result confirmed the outer orientation of the active binding site of Annexin A2, suggesting an efficient implication of this protein in CMVs interaction with host cells and extracellular environment.

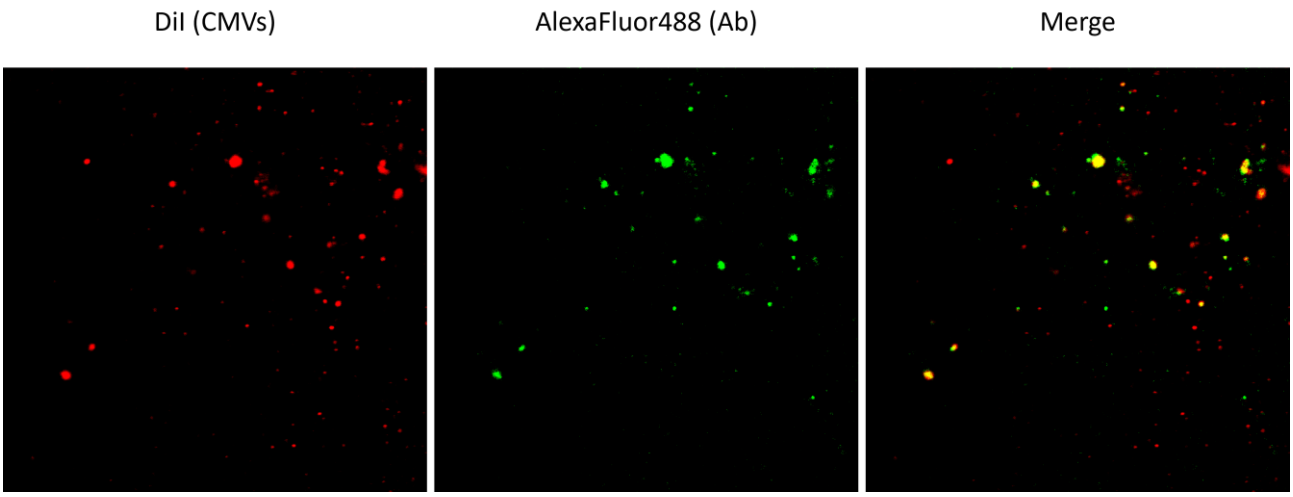

Figure 13: Confocal imaging of DiI-CMVs incubated with anti-Annexin A2 Alexa Fluor® 488-antibody. On the left: sample observed at λ = 570 nm; in the middle: sample observed at λ = 520 nm; on the right, merging of the two signals.

3.3.2. *In vitro* studies on glioblastoma and healthy cells

To study whether the CMVs could exhibit homotypic selective uptake and have a better cellular internalization efficiency compared to synthetic liposomes, and to rule out a possible aspecific interaction of the cells with lipid NPs, confocal microscopy and flow cytometry analysis were performed. Stealth liposomes were prepared with the thin lipid film hydration method, using DSPC, cholesterol, and a 3% mol of pegylated phospholipid (DSPE-PEG2000), which is known to improve stability during storage. Liposome size and Z potential resulted similar to CMV ones, with a hydrodynamic diameter of 145 ± 7 nm and a surface charge of -24 ± 2 mV, thus confirming that liposomes constitute a suitable artificial control to be compared with CMVs. CMVs and synthetic liposomes were fluorescently labelled with CM-DiI and incubated, at the same concentration, with parent and heterologous GBM cells and, as a control, with healthy oligodendrocytes. NP internalization efficiency was observed with confocal microscopy at two different time points. Confocal images revealed that parent and heterologous GBM cells internalized DiI-CMVs as soon as after 30 min of incubation, while a very low cell uptake was observed on healthy oligodendrocytes, suggesting that CMVs internalization involved specific membrane proteins expressed on GBM cells, but not on healthy cells (Fig. 14).

Moreover, synthetic liposomes showed no significant internalization into GBM cells, excluding that CMVs binding to the cell membranes and internalization was due to aspecific interactions of phospholipids with the cell membrane proteins and lipids (Fig. 14B)

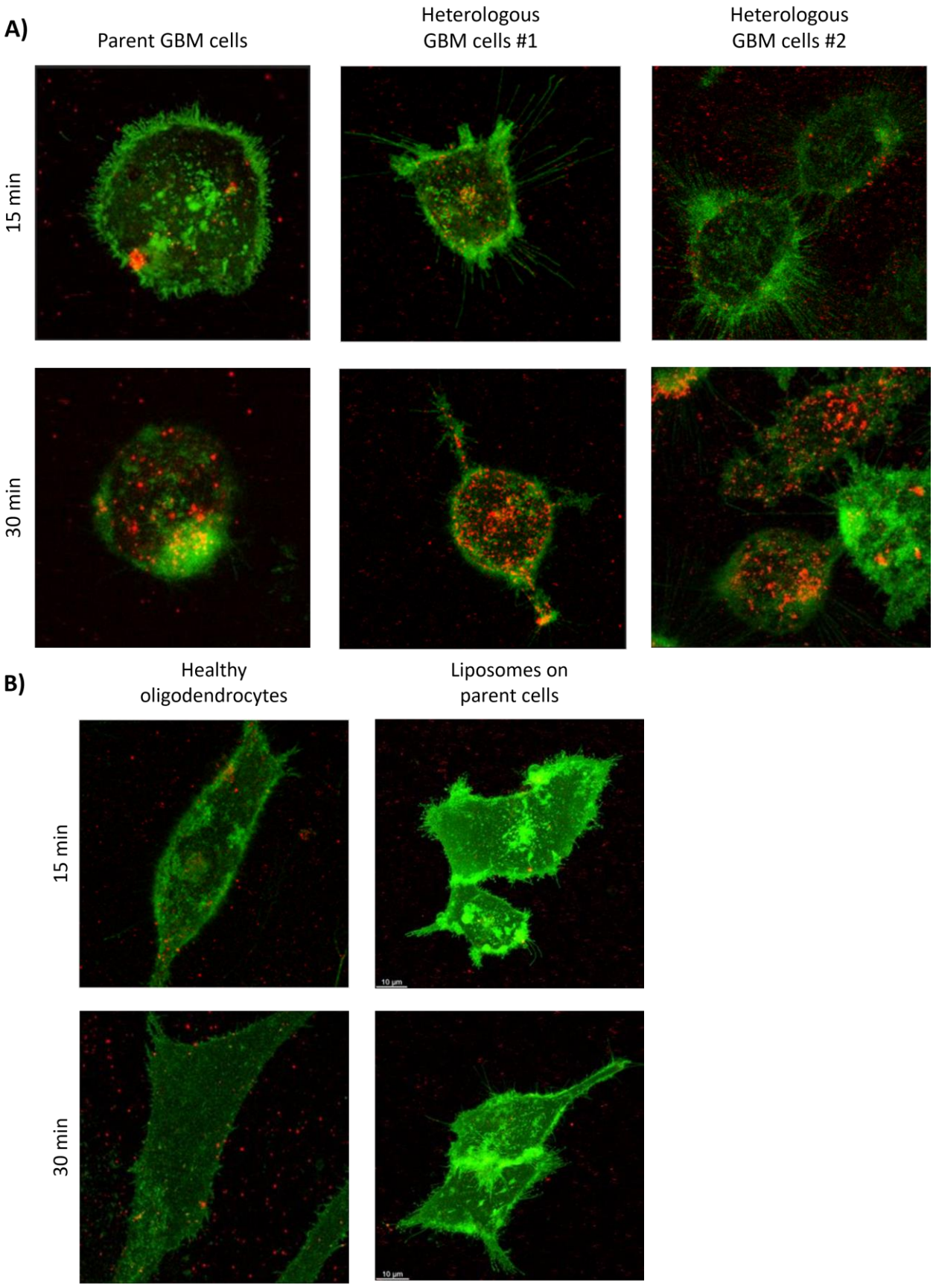

Figure 14: Confocal microscope images of (A) CM-DiI-CMVs incubated with homologous or heterologous GBM cells (B), CM-DiI-CMVs incubated with healthy oligodendrocytes and CM-DiI-liposomes incubated with parent GBM cells at two time points.

Internalization efficiency of CMVs was quantitively studied by flow cytometry. In Figure 15, the fluorescence shift of cells treated with DiI-CMVs at different incubation times is compared to untreated control samples. FACS analysis evidenced a time-dependent interaction of the DiI labelled-CMVs with homologous GBM cells: indeed, while after 30 min incubation only 2.5 % of parent GBM cells were positive to DiI fluorescent signal, this value increased to 76.9 and 81.2 % after overnight and 24 h incubation, respectively, confirming the results observed by confocal microscopy (Fig. 14A). FACS analysis was also performed on heterologous GBM cells incubated with DiI-CMVs for 24 h, demonstrating, also in this case, the high degree of internalization already evidenced through confocal microscopy. The confirmed extraordinary internalization of CMVs into GBM cells, which was not observed into healthy oligodendrocytes in confocal images, suggests the implication of specific GBM membrane proteins, which confer targeting abilities to the CM-derived nanosystem.

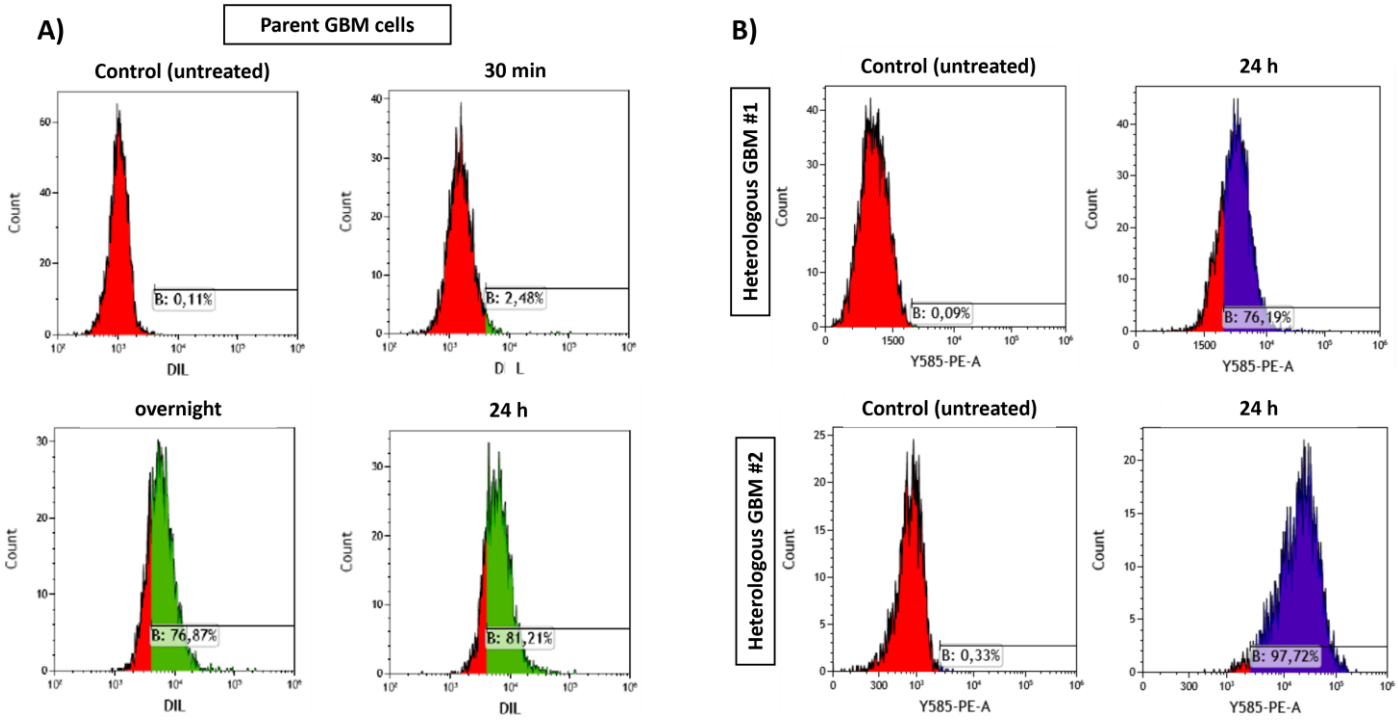

Figure 15: Fluorescence intensity shift of DiI-CMVs internalized by (A) parent and (B) heterologous GBM cells analysed by FACS.

Moreover, the low internalization of synthetic liposomes further proved the specific interaction of CMVs with GBM cells, possibly due to the retention of essential membrane proteins on CMVs surface.

In an interesting research, Han et al. used various brain murine cell lines as CM sources for the development of CM coated nanoparticles for gene delivery to glioblastoma [167]. They coated polyethylenimine/plasmid DNA complexes with CM from C6 rat glioblastoma cells and N2A murine neuroblastoma cells, and demonstrated that brain-CM coating, besides lowering the toxicity of the complex and allowing BBB crossing *in vivo*, conferred homologous targeting abilities towards the cells of origin. Indeed, the authors observed that C6-CM coated NPs had excellent transfection efficiency into C6 cells, a medium transfection of N2A cells and no transfection of L2 rat pulmonary epithelial cells. Similarly, N2A-CM coated NPs better interacted with N2A cells compared to C6 cells and L2 cells and, according to the authors, the observed homologous targeting was related to the conservation of CM proteins on NPs surface, responsible for recognition and binding of tumor cells. These results are consistent to what observed in the present research and offer interesting cues for future studies.

Cytotoxicity of CMVs on healthy oligodendrocytes and on parent and heterologous GBM cells was studied by MTT colorimetric assay at two different time points. This test relies on the reduction of the tetrazolium dye MTT (3-(4,5-dimethylthiazol-2-yl)-2,5-diphenyltetrazolium bromide) to insoluble purple formazan crystals. This reduction involves oxidoreductase enzymes active in viable cells, allowing to calculate cell metabolic activity by measuring formazan absorbance.

The MTT assay revealed a negligible toxicity of the CMVs on healthy oligodendrocytes, as shown in Fig. 16. CMVs exerted slightly higher toxicity on GBM cells, both homologous and heterologous, although this difference might not be significant, considering the biological difference among the analysed cells. Indeed, cancerous GBM cells present different proliferation rate, cellular metabolism, and several other mutated mechanisms due to their mutated proteome. This discrepancy with healthy cells might be responsible for the slight difference detected in cell viability within this analysis.

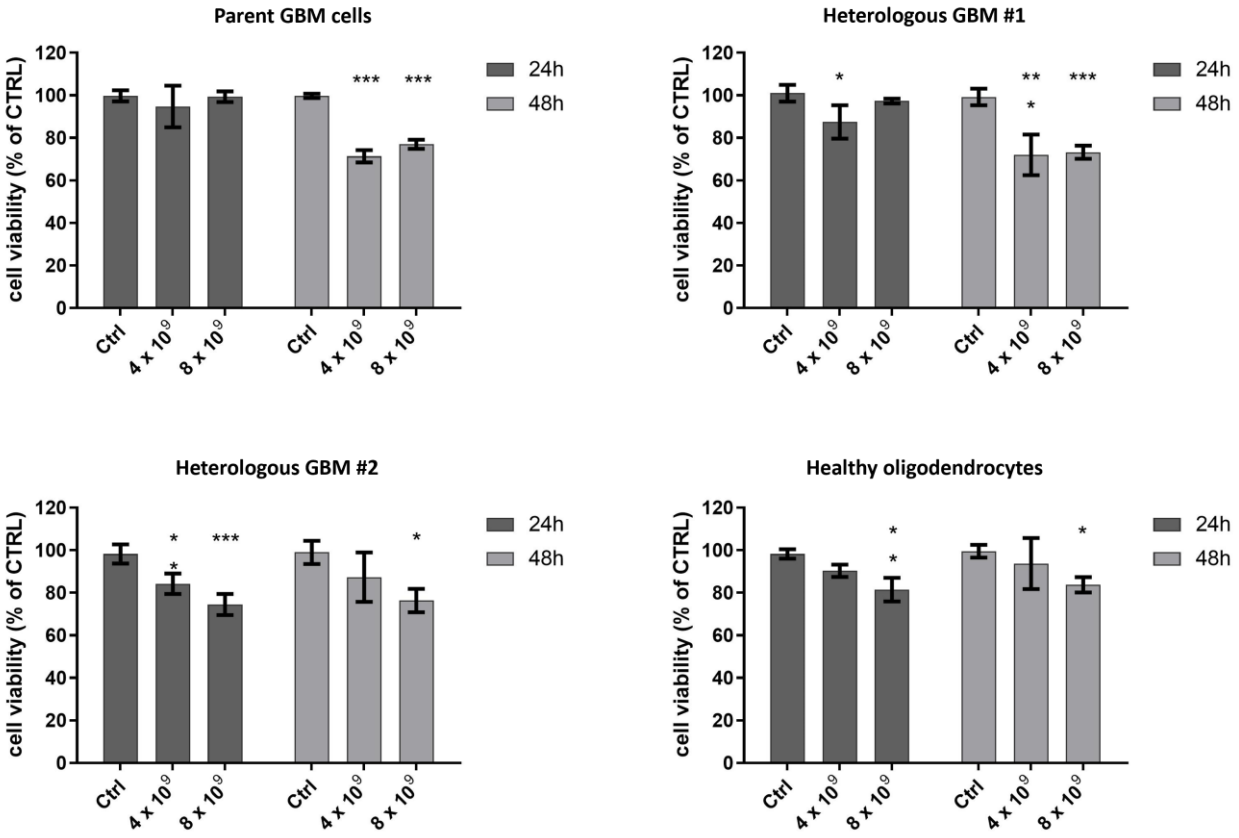

Figure 16: Cell viability of parent and heterologous GBM cells and of healthy oligodendrocytes incubated with CMVs at the two concentrations indicated (particles/mL) for 24 h or 48 h.

3.3.3. B-loaded liposomes

With the aim of performing a future hybridization of CMVs with artificial liposomes, to achieve an increased yield and to improve the industrial scalability of the formulation process, two different formulations of B-loaded pegylated liposomes were developed. The boronated agent employed in this study was boronophenylalanine (BPA), a boron-containing amino acid, approved in clinical trials for the glioma and metastatic melanoma treatment within boron neutron capture therapy. BPA water solubility is very low, consequently in the first formulation, BPA dissolution was achieved through the formation of a complex with fructose (BPA-fr), which was loaded in the aqueous core of pegylated liposomes. BPA-fr complex was formed in water at alkaline pH and the obtained complex solution was slowly neutralized with HCl (Fig. 17) as previously described [168]. BPA-fr was encapsulated into liposomes (Lipo BPA-fr) by hydration of the lipidic film with BPA-fr complex solution with a concentration of 6.5 mg/mL in BPA, followed by extrusion through polycarbonate membranes filters of decreasing pore size at 58° C. This temperature was chosen for the hydration and extrusion processes taking into account the glass transition (T_g) temperatures of the lipids included in the mixture used for liposome formulation; indeed, it is essential that the temperature of the hydrating medium is above the T_g of the lipid characterized by the highest T_g, because this assures higher mobility of the lipids, favoring the formation of bilayers.

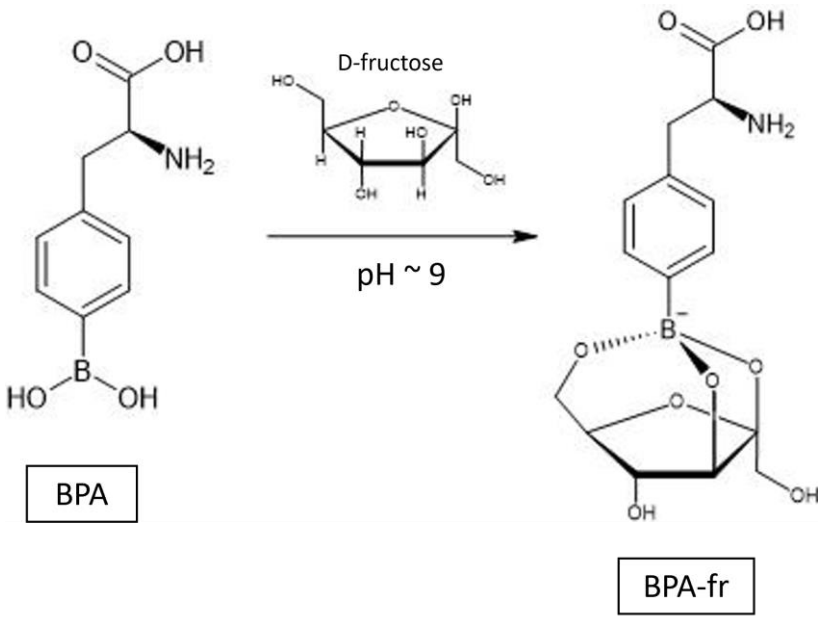

Figure 17: BPA-fructose complex synthesis.

Among the lipids used, DSPC is characterized by the highest T_g (55 °C), so the temperature was set at a slightly higher value.

In a different formulation, BPA was used as free base and inserted within the phospholipid bilayer of liposomes. Briefly, BPA was dissolved in methanol and added to the organic mixture prior to film formation, thus allowing the integration of the lipophilic portion of the molecule in the lipidic film. The film was then hydrated with Milli-Q water, and the resulting suspension was extruded as described above at 58° C, gaining Lipo BPA. Blank liposomes, Lipo BPA-fr and Lipo BPA were physico-chemically characterized, and the encapsulated BPA was quantified following purification through size exclusion chromatography. As reported in Table 3, from DLS analysis, the hydrodynamic diameter of Lipo BPA-fr resulted to be 197 ± 4 nm, which is significantly higher (p<0.005) than that of blank liposomes and of Lipo BPA, probably due to a swelling effect caused by the high osmotic pressure of BPA-fructose encapsulated in the vesicles. On the other hand, the Z potential of Lipo BPA-fr was more negative (p<0.005) compared to Lipo BPA; this might be explained by the presence of the zwitterionic portion of BPA on the surface of Lipo BPA, which could have an impact on the Stern layer surrounding the liposomes and hence on the potential difference detected by the instrument. This variation of Z potential in Lipo BPA might further confirm the boronated molecule intercalation into the phospholipid bilayer.

	Size (nm)	**PDI**	**Z potential (mV)**	**EE%**	**DL%**
Liposomes	145 ± 7	0.06 ± 0.03	-23 ± 2		
Lipo BPA-fr	197 ± 4	0.07 ± 0.03	-17 ± 3	2.4 ± 0.5	6 ± 1
Lipo BPA	142 ± 7	0.07 ± 0.01	-7 ± 2	7.8 ± 0.4	3.0 ± 0.1

Table 3: Physico-chemical characterization of blank and BPA-loaded liposomes (n=3).

Prior to size exclusion chromatography, the excess of unencapsulated BPA-fr was removed from the Lipo BPA-fr formulation through centrifugation on filter membranes

with a cut off of 100 kDa. This step was necessary to avoid pressure increase into the HPLC system caused by the high osmotic contribute of the BPA-fr solution.

All liposomal formulations were then purified through size exclusion chromatography using semipreparative HPLC, to remove the buffer salts, the lipid material not included in the liposomal vesicles, and the unencapsulated BPA. Size exclusion chromatographic separation is based on the different molecular weight (or better hydrodynamic volume) of the compounds within the sample. The process of separation involves the exclusion or inclusion of solutes during their passage through a stationary phase composed of heteroporous inert cross-linked polymeric gels or beads. The mechanism relies on the varying rates at which solute molecules penetrate the gel particle's interior. Since large molecules are excluded from the pores, they will enter the effluent first by passing through the gaps created by the gel particles or matrix, while smaller molecules will move more slowly through the column as they distribute in the mobile phase inside and outside the molecular sieve [169].

In the present purification, liposomes were characterized by an elution time of around 5 min, whereas smaller free molecules and ions eluted after 10 min. In Figure 18, the RI chromatograms of the liposomal formulations (blank liposomes, Lipo BPA and Lipo BPA-fr) and of the BPA-fr complex solution are reported. As shown in the chromatograms, liposomes, were efficiently separated from the unencapsulated drug, which was characterised by a higher retention time (between 11 and 13 min). Moreover, as shown in Figure 18A, this method enabled to resolve two peaks for BPA-fr complex and only one for free BPA. This could be further studied through the UV spectra showed in Figure 18B. Here, the spectra of the two peaks observed for the BPA-fr solution are compared to the BPA peak in the Lipo BPA UV chromatogram. BPA-fructose complex absorption maximum at 262.0 nm [170] was observed in the first peak eluting at about 11 min in the BPA-fr solution chromatogram, while the second wide peak eluting at about 12 min corresponds, most likely, to uncomplexed BPA, coeluting with salts like NaCl, present in high concentration due to the BPA-fr complex preparation. Free BPA, having a UV absorption maximum at 269.1 nm [170], showed a higher retention time, being a smaller molecule compared to BPA-fr, and it was clearly recognizable in the Lipo BPA chromatogram in Fig. 18A.

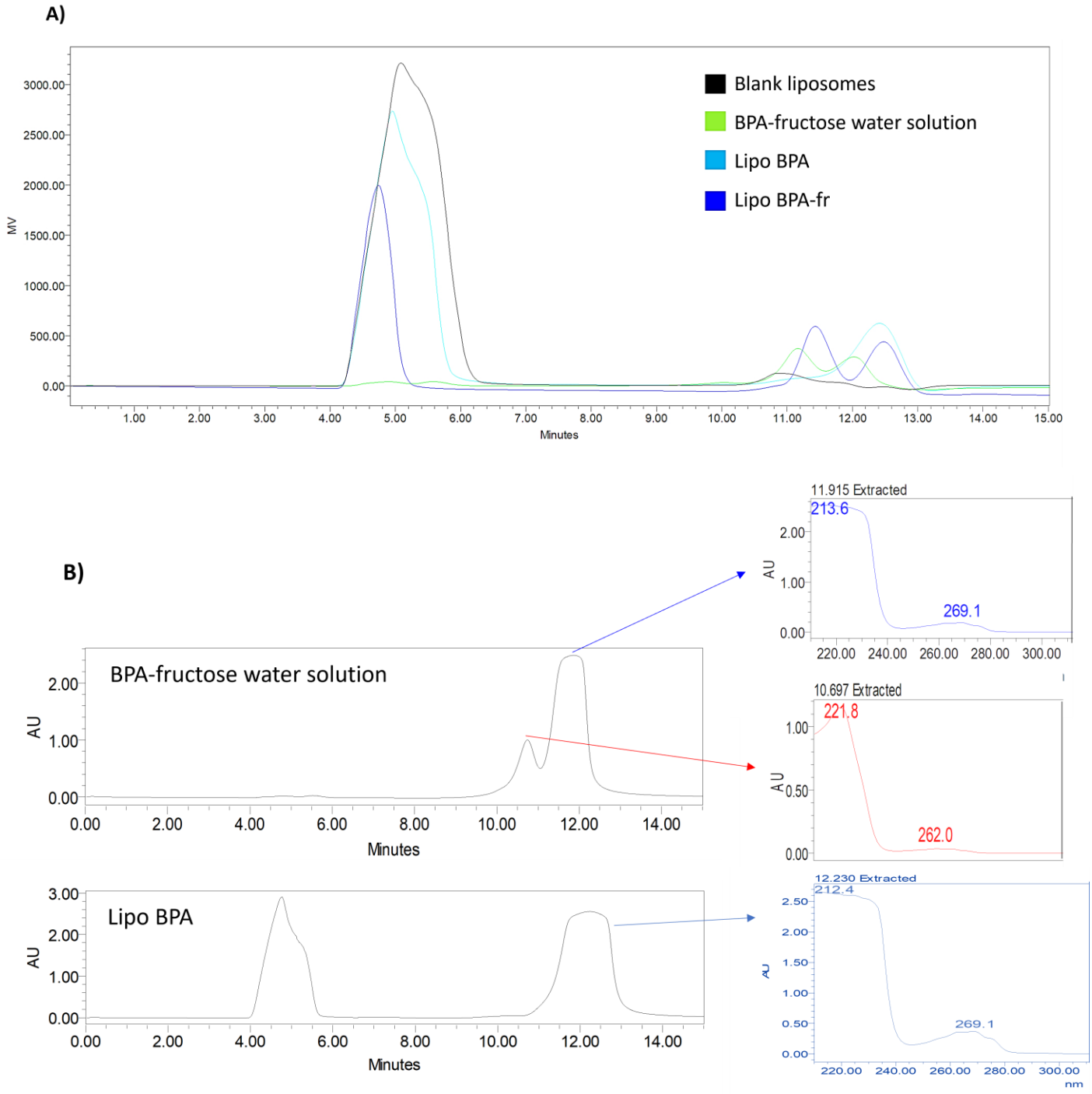

Figure 18: RI chromatograms obtained by SEC purification of the liposomal suspensions. (A) Chromatograms obtained from 400 µL injections of the indicated liposomal suspension and of a 1 mg/mL BPA-fructose solution; (B) semipreparative SEC UV chromatograms of BPA-fr solution and Lipo BPA dispersion, with the UV complete spectra of the single peaks.

After purification, a monodispersed population of liposomes was obtained, with no statistically significant difference (p>0.2) in size and Z potential compared to non-purified liposomes. The stability of purified Lipo BPA-fr and Lipo BPA suspensions was studied by DLS during 30 day-storage at 4 °C and, as shown in Figure 19, no significant variations in size, PDI and Z potential were detected along the monitored period, demonstrating the good stability of both systems.

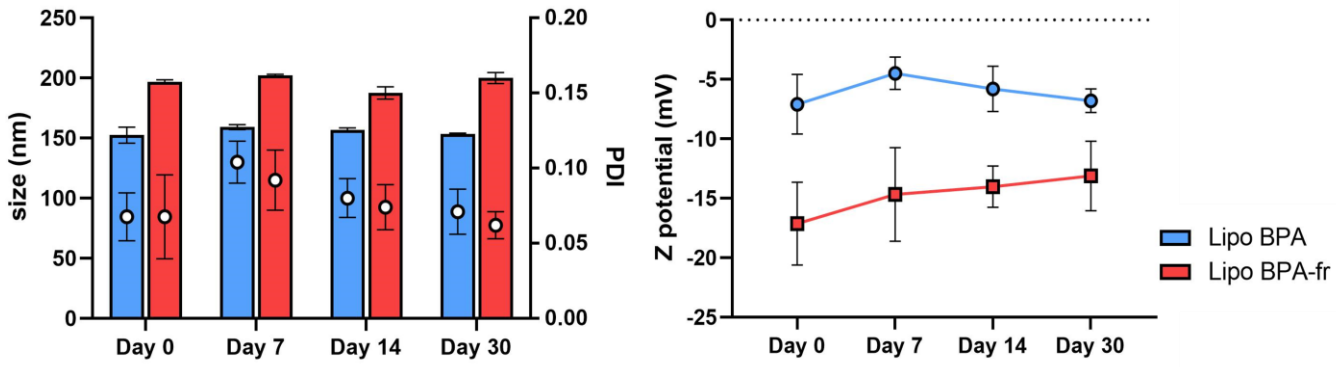

Figure 19: Stability study of the BPA-loaded formulations.
DLS results are expressed as mean value ± SD (n = 3).

Lyophilized purified Lipo BPA-fr and Lipo BPA were analysed by ICP-AES analysis. This technique allows to detect and quantify the presence of specific chemical elements. Briefly, it relies on the use of ionized argon-derived plasma, for the excitation of nebulized analyte molecules in the sample. Electrons and charged ions in the plasma collide with sample molecules and cause their atomization and ionization, leading to electrons loss and recombination, responsible for radiation emissions at a characteristic wavelengths [171]. In the present work, this technique was employed to measure boron atoms in digested Lipo BPA and Lipo BPA-fr samples, enabling BPA quantification in final purified suspensions.

Briefly, lyophilized powders were dissolved in methanol to assure vesicle disruption, thus avoiding analysis artefacts due to colloid formation. The methanolic solutions were dried in Teflon containers to prevent boron contaminations from glass, and the digestion was performed in 65% (m/m) nitric acid at 160 °C for 6 h in the same containers. Fixed aliquots of a standard yttrium solution were added to the samples as internal standard

and the highest intensity wavelength for boron detection was selected (249.773 nm). Before determination of BPA and BPA-fr encapsulation, the absence of a significant matrix signal was assessed, and the procedure for B extraction from liposomal suspensions was validated through BPA and BPA-fr recovery tests. Different aliquots of lyophilized blank liposomes were treated as described for BPA-loaded liposomes to measure matrix signal, whereas the recovery tests were performed by spiking blank liposomes with an accurately measured amount of BPA or BPA-fr solutions. After sample treatment and ICP-AES analysis, boron recovery was calculated by measuring the BPA and BPA-fr found in the spiked liposomes, expressed as the percentage over the initial drug added to the blank sample. The resulting recovery was higher than 90% for both BPA and BPA-fr (91.4 % and 94.5 % respectively), thus validating the suitability of the procedure for the determination of encapsulated BPA and BPA-fr in the two formulations.

In Lipo BPA suspension, 117 ± 6 µg of BPA were found after purification, while in Lipo BPA-fr formulation the final encapsulated BPA was 279 ± 8 µg. Results of DL% and EE% for the developed formulations are reported in Table 3. A higher drug loading % was reached for Lipo BPA-fr, due to the better solubility of the BPA-fr complex in water compared to the low solubility of free BPA in methanol. The different solubility in these solvents allowed to increase the initial drug amount in Lipo BPA-fr formulation mixture, which can also explain the lower value of EE%.

A suitable strategy to increase BPA loading into liposomes might be the co-loading of neat BPA and BPA-fr in the same formulation by embedding the drug into the lipidic bilayer and contextually encapsulating the aqueous solution of the complex in the core. This method was already evaluated by Pavanetto et al., who demonstrated that liposomes loaded with BPA-fr and BPA exhibited a drug content 4-fold higher than formulations encapsulating BPA-fr only. Moreover, they evidenced that, differently from conventional liposomes, pegylated vesicles were able to encapsulate a higher amount of BPA and BPA-fr, allowing to reach *ex vivo* blood and tissue boron concentrations suitable for BNCT application [170]. With this strategy, the authors were able to reach a maximum EE% value of 82 %. However, the comparison of this value with the results obtained in the present study might not be appropriate given the different method used to prepare

liposomes, since the authors employed the reverse-phase evaporation method followed by extrusion.

In another study, BPA-fr was co-loaded with B-381, a boronated 2-nitroimidazole derivative previously synthesized by the authors, into thermo-responsive liposomes prepared by thin film hydration [172]. In this work, the EE% obtained was about 4.5–5 %, which is comparable to the results obtained within the present study. An improvement in Lipo BPA-fr drug loading could be certainly achieved by increasing the concentration of BPA-fr solution used for the film hydration, but it would be necessary to consider the osmotic force deriving from the drug solution and the possible consequent increase in vesicle size.

3.4. Conclusions

A stable GBM cell membrane-derived bio-mimetic nanosystem (CMV) was developed, thoroughly characterized and tested *in vitro*. CMVs resulted stable nano-sized vesicles with a monodisperse distribution and a negative surface charge. Their yield of production was satisfying, although a comparison with other bio-derived systems is insidious. TEM and AFM observation confirmed their round shaped and bi-layered structure and their elasticity (expressed as Young's modulus) was found to be slightly higher compared to what reported in literature for exosomes. CMVs resulted purified from any potentially detrimental DNA or RNA contamination, thus validating the protocol for membrane isolation from cancer cells homogenate. Membrane proteins typical of the parent cells and possibly involved in the selective targeting process were preserved. The protein profile of CMVs was deeply studied: the retention of membrane proteins characteristic of the originating GBM cells was demonstrated and the specific orientation of one of the most abundant membrane proteins (i.e., annexin A2) on the outer surface of CMVs was investigated by immunostaining. The relevant role of the preserved proteins in cell interaction was evidenced by *in vitro* tests, and their implication in homologous targeting and immune escape will possibly find evidence with *in vivo* experiments.

With the future aim of designing hybrid systems by fusing cell membranes with artificial lipids, a stable formulation of pegylated liposomes was developed, and two loading methods for the BNCT agent BPA were evaluated. In Lipo BPA-fr, the water-soluble complex BPA-fructose was encapsulated in the aqueous core of liposomes, resulting in stable nanosized vesicles with a negative surface charge, whereas in Lipo BPA the neat drug was inserted in the phospholipid bilayer, causing an increase in Z potential. However, the encapsulation results obtained for these two BPA loading methods were not satisfying, suggesting that an optimization of the procedure would be necessary for a future use of the B-loaded systems for hybridization with cell membranes.

4. Cell membrane-derived vesicles and hybrids with synthetic lipids from colorectal cancer cells

4. Cell membrane-derived vesicles and hybrids with synthetic lipids from colorectal cancer cells

4.1. Introduction

4.1.1. Colorectal cancer: epidemiology and progression

Colorectal cancer (CRC) comprises colon and/or rectum cancer and represents the third most diagnosed and second most fatal cancer globally [105]. Aberrant proliferation of glandular epithelial cells of colon is the predominant cause of CRC development, and risk factors could be both environmental and genetic. Indeed, multiple studies have demonstrated that the development of CRC is related to non-modifiable risk factors and modifiable risk factors. Personal medical history (sex, age, race, adenomatous polyps or inflammatory bowel disease history) and family history cannot be controlled by individuals, whereas the modifiable factors are related to individual habits or lifestyles (obesity, physical inactivity, regular alcohol consumption, cigarette smoking, the consumption of red and processed meat) [173]. Depending upon the genetics and the aetiology of the disease, CRC can be classified in three types: sporadic, devoid of any familial predisposition and emerging as a result of dietary and environmental factors (the most diffused); hereditary, which accounts for less than 5% of incidence and is characterized by identifiable germline mutations and phenotypes; and familial, with no identifiable germline mutation or specific pattern of inheritance, but higher-than-expected incidence within a family [174].

Since CRC progresses slowly over time, early identification by screening average-risk individuals increases treatment chances. The success of screening is demonstrated by the fact that, from 2000 to 2015, an increase in screening rate was linked to a 52.4% decrease in mortality and a 25.5% reduction in annual CRC incidence [175]. The gold standard for CRC screening and diagnosis is colonoscopy, which has been increasingly replaced by radiologic, blood-based, and stool-based techniques, given the less invasive nature of these tests [176]. Moreover, novel biomarkers, like fecal bacterial indicators and miRNAs, have been identified as target for innovative screening tests, with wide potential applications [177].

CRC matures when epithelial cells become hyperproliferative and cause the formation of a benign adenoma, which can advance to cancer and metastasize. Polyps or

adenomas, characterizing stage 0, are benign soft cancer formations which are not able to metastasize to other parts of the body [174]. In stage I, adenomas become malignant adenocarcinomas, spreading from the mucosa into the submucosa and the muscularis propria of the colon. Then the tumor grows in volume and further invades the connected tissues: the peri-colorectal tissues (stage IIA) and the visceral peritoneum (stage IIB). Stage III CRCs are associated with the loss of E-cadherin expression, which induces the epithelial to mesenchymal transition process, leading cells to the loss of epithelial characteristics (cell-cell adherence), and the acquisition of mesenchymal properties, such as increased motility and resistance to apoptosis, and degradation and production of extracellular matrix components [178]. At this stage, cancer emerges into muscularis propria metastases in surrounding tissues or regional lymph nodes. Distant metastases in liver, lungs, bone and brain characterize stage IV cancer development, involving the migration of circulating tumor cells (CTCs) which are primarily responsible for metastatization and represent poor prognosis indicators for late stage CRCs [179] (Fig. 20). Five-year survival rates are over 90% for stage I CRC and 10% for stage IV CRC, according to Surveillance, Epidemiology, and End Results population-based data [180].

Genomic instability of several forms plays a significant role in the development of sporadic or inherited CRC, by facilitating the acquisition of genetic and epigenetic mutations in specific oncogenes and/or tumor suppressor genes, including genes of the chromosomal instability (CIN) and microsatellite instability (MIN) pathways [173]. Frequently, the uncontrolled proliferation of cells is related to the mutation of adenomatous polyposis coli (APC), DNA mismatch repair (MLH1 and MSH2), K-ras or p53 genes, and the accumulation of further genetic mutations leads to a malignant phenotype and progression of CRC [181].

According to the international guidelines, for patients in stage II or stage III, localized or restricted CRC is treated with surgical resection followed by an adjuvant therapy (chemotherapy or radiotherapy) [182]. For patients presenting unresectable metastasis (approximately 20–30% of CRC patients) or recurrent disease, systemic chemotherapy is applied to improve survival and palliation through the control of tumor size and symptoms. The most used active cytotoxic drugs include 5-fluorouracil (5-FU), irinotecan, oxaliplatin and capecitabine, alone or in combination, which are

though responsible for adverse side effects on healthy tissues due to non-specific drug biodistribution [183]. Radiation therapy represents another anticancer strategy, primarily used in patients at risk of tumor recurrence: it is usually applied before surgery to shrink cancer, improving its resection efficacy, or successively, to destroy any remaining cancer cells. However, also this kind of therapy is associated with severe acute and late side effects such as skin infections, fatigue, and fecal and urinary incontinence [184].

New anticancer approaches are now focusing on immunotherapy, relying on different strategies like the activation of host's immune system to achieve specific destruction of targeted cancer cells. This can be obtained by the increase of effector T cells, the suppression of negative immune checkpoints, or the elimination of cytokines and cells related to tumor development [185]. However, immunotherapeutics frequently have to deal with high costs, severe side effects, and possible short-term efficacy [186].

To date, the most diffused CRC chemotherapy involves the use of cytotoxic active principles, related on one side with severe side effects, and on the other side to drug resistance due to acquired mutations of cancer cells, leading to decreased anticancer efficacy [183]. Thus, improved and targeted therapies to protect and selectively deliver cytotoxic drugs to the site of interest are needed, to minimize these undesired effects.

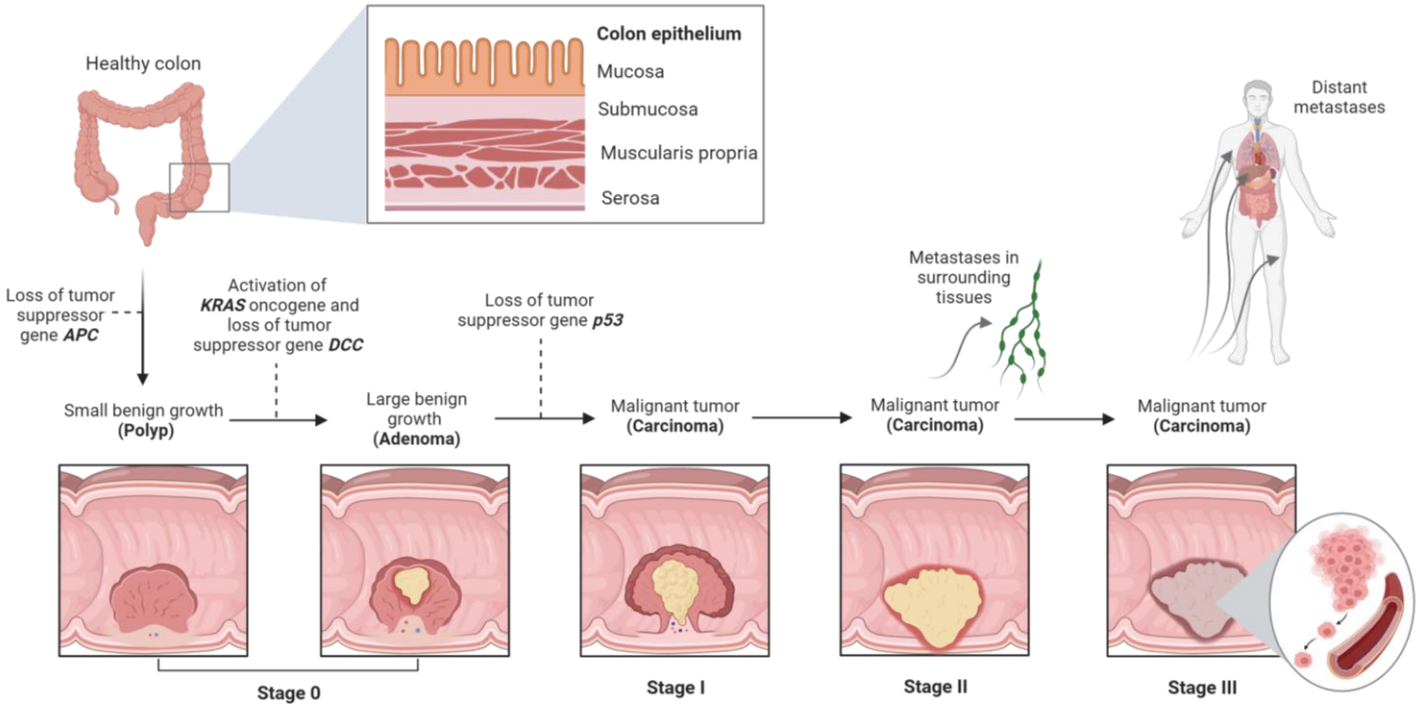

Figure 20: Schematic representation of CRC progression. Created with BioRender.com

4.1.2 Nanomedicine in colon cancer treatment

Nanotechnology has opened up to new strategies for improved performances in screening, diagnosis, and treatment of CRC along with other types of tumors. Nano-sized particles of different shapes and compositions have emerged as important and promising novel tools for colorectal cancer.

Iron oxide NPs are established diagnostic and therapeutic tools in oncology due to their superparamagnetic properties and high biocompatibility [187]. They are 1-100 nm-sized NPs with a magnetic core, usually surrounded by a polymeric coating carrying active molecules. Some examples that have been studied for their potential application in CRC therapy are 5-FU loaded iron oxide NPs, which were demonstrated to reduce tumor growth in heterotopic human CRC in mice with magnetic hyperthermia [188]; epirubicin-5TR1 aptamer-superparamagnetic iron oxide NPs, which efficiently delivered epirubicin to C26 murine colon carcinoma cells, concurrently allowing tumor detection by MRI [189]; or chitosan-coated iron oxide NPs, able to enhance reactive oxygen species' production in a human colorectal carcinoma cell line [190].

Another type of nanosystem with widening applications in CRC imaging are quantum dots, which are nanocrystal particles of semiconductors ranging from 2-10 nm, with fluorescence emission, characterized by extended excitation wavelengths and narrow emission band [190]. Quantum dots have been used as diagnostic markers for CRC in numerous *in vitro* and *in vivo* studies [191, 192].

Also PLGA NPs have found wide application in cancer therapy, thanks to their biodegradability, biocompatibility and ability to entrap small molecules enhancing their chemical stability and sustaining their release. PLGA-NPs were exploited in different formulations designed for CRC treatment: they were loaded with 5-FU to reduce the proliferation rate of HT-29 colon cancer cells [193], while their ability to impair tumor growth *in vivo* was evaluated after loading with docetaxel and SPIONs [194] or with 5-FU and perfluorocarbons [195].

Dendrimers are other biodegradable nanosized structures with wide versatility in anticancer drugs and diagnostic agents delivery. They were successfully conjugated with antibodies for colorectal CTCs targeting for diagnostic purposes, introducing an

innovative cell-capture platform exploiting nanostructured dendrimers as scaffolds to assemble antibodies with multiple targets [196]. In another study, the *in vitro* and *in vivo* theranostic efficacy of curcumin-loaded dendrimer-gold hybrid structures was evaluated, showing high cellular uptake in C26 and HT29 colorectal cells, effective anti-tumor activity and accurate computed tomography (CT) imaging potential in C26 tumor-bearing mice [197]. Dendrimers were also loaded with camptothecin [198] and oxaliplatin [199] with promising results on CRC cells *in vitro*.

Liposomes were the first nanocarriers approved by regulatory agencies for anticancer therapy, with the commercialization of Doxil® in 1995 for treatment of Kaposi sarcoma [200]. Since then, several liposomal formulations have been approved for chemotherapeutics delivery, to mention the last, Zolsketil® carrying doxorubicin, was approved in 2022 for the treatment of metastatic breast cancer, advanced ovarian cancer and multiple myeloma [201]. Many others are currently under clinical development, some of which with specific application in CRC treatment. Aroplatin™ is a liposomal formulation composed of DMPC (1,2-dimyristoylphosphatidylcholine) and DMPG (1,2-dimyristoylphosphatidylglycerol), incorporating a structural analogue of oxaliplatin. Preclinical data showed that it had lower IC50 values than oxaliplatin, carboplatin or cisplatin in several cancer cell lines and a phase 2 trial on patients with therapy-refractory advanced CRC gave promising results in terms of tolerability and selective tissue distribution [202]. Thermodox® is a thermosensitive liposomal formulation involved in phase II investigations (NCT02181075) for safety, viability, and effectiveness in treating liver metastases in CRC [203]. Thermosensitive liposomes enable the temperature-triggered release of their encapsulated content, thanks to their specific lipidic composition, allowing a temperature-induced rise in bilayer permeability in response to moderately hot temperatures (39–45 °C) [204]. In the mentioned clinical trial, the doxorubicin-loaded liposomes were administered along with ultrasound-mediated hyperthermia, resulting in safe and effective enhanced delivery and penetration of the chemotherapeutic agent; these promising results might broaden the application of these thermosensitive liposomes to a wide range of drug classes to treat primary and metastatic solid tumours.

Even though several nanoformulations are undergoing clinical trials, only few of them are actually exploited to treat CRC, suggesting that further research is needed in this field.

4.2 Materials and methods

4.2.1 2D cell cultures

Murine colorectal cancer cells (CT26) and murine ovarian cancer cells (ID8) were maintained in Dulbecco's Modified Eagle Medium (DMEM) supplemented with 10% fetal bovine serum (FBS) and penicillin-streptomycin. Murine leg muscle myoblasts (C2C12) were cultured in RPMI-Glutamax (all from Gibco, Thermo Fisher, USA) supplemented with 10% FBS and penicillin-streptomycin. Cells were counted with manual Scepter™ 2.0 Cell Counter (Life Science Research, Merck, Germany) equipped with 60 µm sensors.

4.2.2 CMVs, liposomes and hybrids preparation

CMVs preparation: CMVs from CT26 were prepared exploiting the CM extraction method already optimized for GBM-CMVs preparation. Briefly, a cell homogenate, obtained from 1-2 × 10^7 CT26 cells using a Dounce homogenizer in homogenizing buffer (225 mM mannitol, 75 mM sucrose, 0.5% w/v BSA, 0.5 mM EGTA, 30 mM tris-HCl, protease inhibitor cocktail 5 µL/mL and 1% v/v phosphatase inhibitor cocktail, pH 7.4), was subjected to a differential centrifugation procedure. A first centrifugation at 800 x g was performed for 5 min at 4 °C; the pellet was discarded, and the supernatant was centrifuged again for 5 min at 800g and 4 °C, and then for 10 min at 10000 x g and 4 °C; the supernatant was collected again and centrifuged for 20 min at 25000 x g and 4 °C to obtain the crude membrane fraction as a pellet. The pellet was resuspended in starting buffer, with the same composition used for GBM-CMVs, and centrifuged again for 20 min at 25000 x g and 4 °C to remove microsomal and cytosolic contamination. As discussed in the previous chapter, a further washing step was introduced (20 min at 25000 x g) to ensure DNA and RNA elimination from the final CM fraction. The obtained purified plasma membranes were resuspended in Milli-Q water or DPBS 1x (Gibco, Thermo Fisher, USA) and extruded through polycarbonate filters with decreasing pore size (400 – 200 – 100 nm) using an Avanti mini extruder (610000, Avanti Polar Lipids, USA) on a heating block set at 37 °C. Fluorescent labelling of CMVs was performed by resuspending the CM pellet with an ethanolic solution of the fluorescent probe (0.08 - 0.15 nmol depending on the amount of the starting material). Different fluorescent dyes were selected for labelling the bilayer membranes: CM-DiI, Cyanine5-phosphatidylethanolamine (Cy5-PE), Rhodamine-phosphatidylethanolamine (Rhd-PE)

or Nitrobenzoxadiazole-phosphatidylethanolamine (NBD-PE) (all from Thermo Fisher Scientific, USA). After vigorous stirring, ethanol was evaporated with N_2 flux, and the obtained labelled pellet was hydrated with Milli-Q water or PBS (800-900 µL depending on the amount of homogenized cells) and extruded as for non-labelled vesicles.

Liposome preparation: Stable stealth liposomes were obtained with the same procedure described in the previous experimental section. Liposomes were prepared by hydrating a lipid film composed of DSPC, DSPE-PEG2000 and cholesterol in a lipid ratio of 52:3:45 mol%. Hydration was performed with Milli-Q water or PBS at 58 °C for 2 h, obtaining a multilamellar vesicle suspension with a final lipid concentration of 5 mM. The resulting suspension was extruded with an Avanti mini extruder (610000, Avanti Polar Lipids, USA) through polycarbonate filters with decreasing pore size (400 – 200 – 100 nm) on a heating block set at 58 °C. Cy5-PE, Rhd-PE and NBD-PE labelled liposomes were prepared by adding a chloroform probe solution (0.4% mol on total lipids) to the organic mixture, prior to film formation by solvent evaporation. 5 mM liposomes were diluted in PBS to reach CMVs and hybrids concentration for *in vitro* studies.

Hybrids by extrusion (HEs) preparation: For membrane hybridization in HE, the purified CMs were co-extruded with multilamellar artificial vesicles. Briefly, the resuspended CM pellet, isolated following the protocol described for CMVs preparation, was co-extruded in a 1:1 volume ratio with a diluted aqueous suspension of multilamellar vesicles resulting from the hydration of the phospholipid film as described above. Co-extrusion was performed using an Avanti mini extruder (610000, Avanti Polar Lipids, USA) and polycarbonate filters with decreasing pore size (400 – 200 – 100 nm) on a heating block set at 37 °C, and different protein:artificial lipid mass ratios (P:L ratio) were employed (1:1.5, 1:2.5 w/w) resulting in two different formulations: HE 1:1.5 and HE 1:2.5. Fluorescently labelled hybrids were obtained by separately labelling the two different portions (CMs and artificial multilamellar vesicles) as described for labelled CMVs and labelled liposomes and by co-extruding them in Milli-Q water or PBS.

Hybrids by microfluidics (Hµs) preparation: Microfluidic generation of hybrids was performed with the small volume-NanoAssemblr® Spark™ machine (Precision NanoSystems, Canada) equipped with toroidal micromixer cartridges with a Y-type injection system. The aqueous phase consisted in a CM suspension in Milli-Q water or

PBS (80 µL of membrane suspension), while an ethanolic solution of DSPC, DSPE-PEG2000 and cholesterol in a lipid ratio of 52:3:45 mol% represented the organic phase (40 µL). PBS was used as dilution media and the same P:L w/w ratios used for HEs preparation were employed to prepare the hybrids by microfluidics (Hµ 1:1.5, Hµ 1:2.5). Within NanoAssemblr® Spark™ the two phases are injected simultaneously in the microchannels at a constant pressure, set by selecting a setting input (from 1 to 9), which depends on the volumes used. Injection setting 7 was selected for these formulations. The resulting vesicles suspension is collected in the dilution well. The final volume of each formulation was 220 µL, which were diluted with PBS to an appropriate volume to reach the same concentration of CMVs and HE, for *in vitro* experiments. Fluorescent hybrids were prepared by labelling the CMs with Cy5-PE or CM-DiI, as already described for CMVs, prior to resuspension with water or PBS, while the synthetic lipids portion was labelled by dissolving fluorescent phospholipids (Rhd-PE or NBD-PE) in ethanol and mixing them in the organic phase, prior to film formation.

4.2.3 CMVs and hybrids characterization

DLS: Hydrodynamic diameter, polydispersity index and Z potential of the nanosystems were determined by DLS (Zetasizer® NanoZS, Malvern, UK). To carry out the size measurement, liposomes were diluted 1:100 in Milli-Q water, while CMVs and hybrids were measured without further dilution. As for vesicles obtained by GBM cells, the average hydrodynamic diameter value was obtained from three measurements (10 sub runs each) and the Z potential was determined through an electrophoretic mobility measurement. The physical stability of CMVs and hybrids was evaluated by monitoring the size, PDI and Z potential of the different suspensions when stored at 4 °C.

NTA: As for GBM-CMVs, vesicle concentration was studied by NTA (NS300, Malvern, UK). Vesicles suspensions were diluted with Milli-Q water to a suitable concentration: CMVs and hybrids underwent a 1:200-1:500 dilution, while liposomes were diluted 1:100000. A 488 nm laser was used to detect the nanoparticles in scattering mode and the yield of the CMVs and hybrids production process was determined as the number of final vesicles obtained per initial cell, calculated with the following equation:

Yield = number of final vesicles/number of initial cells homogenized

Fluorescence Resonance Energy Transfer (FRET): The successful membrane fusion in hybrid vesicles was assessed by a FRET assay. Briefly, to study the effective insertion of CMs into the artificial membranes by extrusion, CMs and artificial multilamellar vesicles were labelled as described above, with the fluorescent acceptor dye CM-DiI ($\lambda_{exc/em}$=550/570 nm), and the donor dye NBD-PE ($\lambda_{exc/em}$ =463/549 nm) respectively, prior to coextrusion. Concerning hybrids by microfluidics, CM-DiI-labelled CMs were hydrodynamically mixed with the ethanolic solution of lipids containing a calculated amount of NBD-PE (NBD:CM-DiI 1:2.5 mol ratio). The fluorescence spectrum of FRET hybrids and of the physical mixture of CM-DiI-labelled CMVs and NBD-labelled liposomes were recorded in the range of 500 to 650 nm at an excitation wavelength of 463 nm, using a FP-8500 spectrofluorimeter (JASCO applied science, Canada). The fluorescence emission from the acceptor dye was measured to evaluate the effective membrane fusion.

Considering the results obtained from the characterization tests above described, only HE 1:2.5 and Hμ 1:2.5 were further characterized.

Cryogenic Transmission Electron Microscopy (Cryo-TEM): The morphology of HE 1:2.5 and Hμ 1:2.5 was assessed by Cryo-TEM. Briefly, 3.5 μL of each formulation were added on a LC300-CU LACEY carbon supported copper grid, and plunge-frozen using a Vitrobot (Thermo Fisher Scientific, USA) to generate vitreous ice. The samples were stored in liquid nitrogen and imaged with a JEM-1400 Flash electron microscope (JEOL, Japan) operating at 120 kV. Before freezing, hybrids were concentrated by centrifugation at 5000 x g for 10 min at 25° C on Amicon® Ultra 0.5 Centrifugal Filter devices, 30 kDa MWCO. Prior to concentration, Hμ were also dialyzed against Milli-Q water with a 3.5 kDa membrane (Slide-A-Lyzer MINI Dialysis Device, Thermo Fisher Scientific, USA) to remove ethanol, which might impair correct vitreous ice formation.

Bicinchoninic Acid (BCA) assay: The protein content of the isolated CM and of the CMVs and Hμ 1:2.5 obtained from approximately the same amount of initial cells was quantified by a BCA assay (micro-BCA Protein Assay Kit, Thermo Fisher Scientific, USA). A working reagent (WR) was prepared by mixing the three reagents provided with the kit (A, B and C) at a volume ratio of 25:24:1. The calibration standards were prepared by diluting a bovine serum albumin stock solution (2 mg/mL) in 0.9% saline and 0.05%

sodium azide aqueous solutions. Calibration standards and samples were diluted with 2% sodium dodecyl sulphate (SDS) (Thermo Fisher, USA) aqueous solution and the WR. The obtained mixtures were incubated at 60 °C for 60 min and then cooled at RT. The absorbance of calibration standards and samples was measured at 562 nm.

Proteomic analysis: Membrane proteins retained in CMVs and Hμ 1:2.5 were qualitatively studied by proteomic analysis following the protocol already described in the previous chapter for GBM-CMVs. Briefly, the aqueous suspensions of the two types of vesicles, obtained from approximately the same number of initial CRC cells, were dried and lysed in iST-LYSE buffer (PreOmics, Germany) for 10 min at 95 °C on a ThermoMixer (Torrey Pines Scientific, USA) at 1000 rpm. The resulting peptide chains were precipitated on magnetic microparticles and digested with LysC (Fujifilm Wako, USA) and trypsin (Promega, USA) in an enzyme/protein ratio of 1:400 (w/w) and 1:200 (w/w). The peptide mixtures were then acidified with trifluoroacetic acid and separated by liquid chromatography using a C18 column. Peptides were analysed with the Orbitrap Exploris™ 480 MS in DIA mode.

Nucleic acid electrophoresis: As already described for CMs deriving from GBM cells, DNA or RNA presence in the purified CT26 CM fraction was investigated by agarose gel electrophoresis. In this case, the intercalating agent SYBR Green II RNA gel stain (Thermo Fisher, USA) was added to an agarose gel 1% (agarose in tris/boric acid/EDTA buffer), prepared as described in the previous chapter. The samples were mixed with a gel loading buffer and the electrophoretic run was performed at 80 V for 40 min. The gels were imaged with Gel Doc™ EZ (Bio-Rad, USA) and blue transillumination, and the images were elaborated with Image Lab 6.0.1 Software.

4.2.4. *In vitro* internalization study: confocal microscopy, FACS

Confocal microscopy: Confocal microscopy was used to study the internalization efficiency of CMVs and hybrids, compared to liposomes, into parent cells, as well as to confirm the colocalization of CM and synthetic lipids portions in HE and Hμ. To this aim, CT26 cells were incubated at 37 °C in 5% CO_2 environment for 30 min or 2 h with the fluorescent nanovesicles, prepared as described above and labelled with Cy5-PE (CMVs) or Cy5-PE and Rhd-PE (hybrids). The cells were treated with vesicle suspensions diluted in culture medium at a concentration of 1.6 x 10^{10} particles/mL. After 30 min or 2 h, the

cells were fixed with 4% v/v paraformaldehyde in PBS for 10 min at RT, and then stained with Phalloidin-Atto 488 and DAPI in PBS for 1 h at RT to label cytoplasm and nuclei, respectively. The samples were finally mounted in Fluoromount-G™ Mounting Medium (Invitrogen™, Thermo Fisher, USA), and imaging was performed by a Zeiss LSM880 confocal laser scanning microscope (Carl Zeiss, Germany) using a 63x objective.

Fluorescence-Activated Cell Sorting (FACS) analysis: Internalization of CMVs, HE 1:2.5, Hμ 1:2.5 and liposomes into different cell lines was quantitatively investigated at various timepoints. Nanovesicles were prepared as described above and labelled with Cy5-PE. 150000 CT26, ID8 and 50000 C2C12 cells per well were seeded in 24-well plates, cultured for 24 h and then treated with 0.5 mL particle suspensions in complete medium at a final concentration of 1.6 x 10^{10} particles/mL. The cells were incubated with the treatments at 37 °C in 5% CO_2 environment for 30 min and 2 h. Afterwards, the cells were washed with PBS, detached with trypsin-EDTA solution, washed with cell culture medium and stained with LIVE/DEAD® dye (Invitrogen™, Thermo Fisher, USA), 1 μL per well in PBS. After 30 min of incubation at 4 °C, the dye solution was removed, and the cells were washed and read with BD LSRFortessa™ Cell Analyzer (BD Biosiences, USA). Dead cells were excluded from the analysis. Data analysis was performed using FCS Express™ software (Thermo Fisher, USA) and the results were expressed as the mean fluorescence value measured on three biologically independent replicates (three samples each replicate). Statistical analyses were performed with Prism v8.1 software (GraphPad Software, USA).

4.2.5. *In vitro* cytotoxicity study

In vitro cytotoxicity of CMVs and Hμ 1:2.5 was studied on murine healthy myoblasts (C2C12 cell line) using a crystal violet colorimetric assay; HEs were progressively abandoned in later studies given the less promising internalization efficiency results. Briefly, 1000 cells/well were seeded in 96-well plates for 24 h at 37 °C in 5% CO_2 environment, then the cells were incubated with vesicles in cell culture medium at two different concentrations (1.4 x 10^{10} and 2.8 x 10^{10} particles/mL) for 72 h, while control untreated cells were maintained in medium for the same time. After 72 h, the cells were fixed in paraformaldehyde 4% for 30 min at RT and carefully washed with PBS; then a 0.5% crystal violet solution was added and further incubated for 30 min. After washing

with PBS, the plate was allowed to dry at RT, and then methanol was added to dissolve the insoluble crystals formed after crystal violet treatment, and the 560 nm absorbance was recorded using a SPARK® Multimode microplate reader (Tecan, Switzerland). Cell viability is expressed as the mean percentage related to the signal given by the untreated control (6 samples were considered).

4.2.6. CMVs and hybrids effect on the growth of 3D healthy organoids

Mouse intestine organoids, originating from $Lgr5^{tm1(cre/ERT2)Cle/J}$ mice, were cultured in 0.9 mm specifically developed inserts in Corning Matrigel Matrix (REF: 354234). The organoids were cultured in Intesticult Organoid Growth Medium Mouse (STEMCELL Technologies, Canada) for 40 days and passaged every 3-4 days. After passage 10, the organoids were disassembled and plated (day 0). At day 1, they were treated with Hμ 1:2.5 at two different concentrations (1.4×10^{10} and 2.8×10^{10} particles/mL) or with 100 μM oxaliplatin, as toxic control; untreated control samples were maintained in culture medium. Organoid sizes were monitored at day 1, 5 and 8: the plates were observed using an optical microscope ZEISS Axis Vert.A1 (Carl Zeiss, Germany) equipped with a digital camera, and the organoid surface areas were calculated using ImaJ software. Organoid growth was calculated by normalizing the organoid surface area, measured on different days, to their size at day 1. Results were expressed as mean organoids growth considering 5 samples for each treatment condition.

4.3 Results and discussion

4.3.1 Preparation and characterization of CMVs from CT26 cells

CM isolation from CT26 cells homogenate was performed following the protocol already optimized for the extraction of CMs from GBM cells. Considering the initial protocol, an additional washing with the starting buffer was introduced to allow the efficient purification from genetic material contamination, as demonstrated in the previous section. The obtained membrane pellet was then resuspended in water or PBS and extruded. The resulting vesicles were monodispersed nanosized structures with a hydrodynamic diameter of approx. 143 nm and a negative surface charge (Table 4), similarly to the vesicles obtained from GBM cells. Size, PDI and Z potential, which were monitored for 20 days, showed no significant changes (p>0.25) when CMVs were stored in aqueous suspension at 4 °C, demonstrating good stability for the considered time (Fig. 21). A stability study was also conducted storing CMVs in PBS at 4 °C and, also in this case, no significant differences in terms of size and PDI were detected for 20 days.

	Size (nm)	PDI	Z potential (mV)	Concentration (particles/mL)	Yield (x 10^3)
CMVs	143 ± 5	0.14 ± 0.02	-27 ± 3	1.4 ± 0.4 x 10^{11}	6 ± 1

Table 4: Characterization of CMVs from CT26 cells. Physico-chemical properties, concentration of 800 µL suspension of CMVs, and yield of production. Mean values ± standard deviation (n=5).

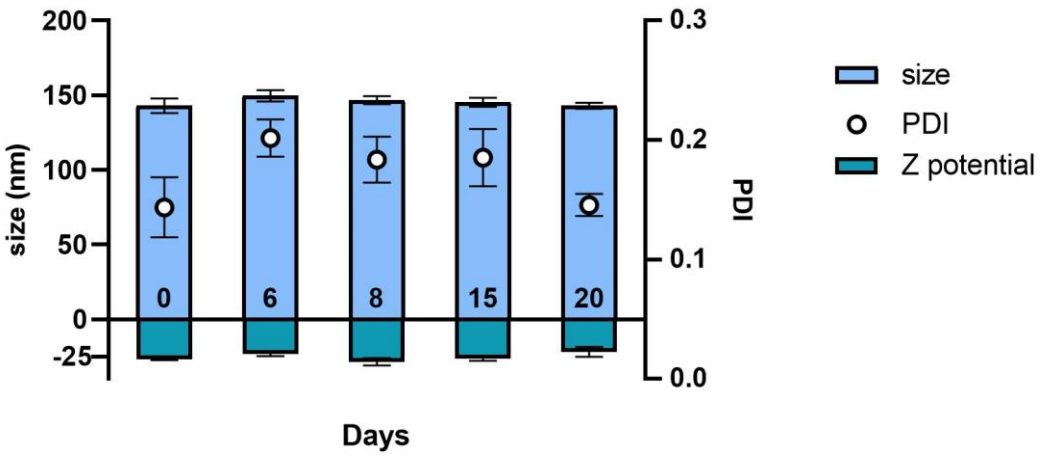

Figure 21: Stability of CMVs from CT26 cells. Mean values ± standard deviation (n=3).

The concentration of 800 µL CMVs suspension deriving from approx. 1.8 x 10^7 CT26 cells was determined by NTA, which is able to measure the number and size of nanoparticles by analysing their Brownian motion via light scattering. This analysis allowed to determine the yield of the CMVs production processes, expressed as the number of vesicles obtained per initial cell (Table 4). The measured throughput was very satisfying: it resulted higher than the value obtained for CMVs from GBM cells, and approx. 10 times higher than the yield reported in the literature for exosome isolation [133, 134]. However, the issues discussed in the previous chapter on the reliability of this comparison must be considered. The higher yield obtained for CRC-CMVs compared to GBM-CMVs might be related to the different types of parent cells: indeed, every cell type is characterized by a peculiar lipidic and protein content that might influence the mechanical properties of the membrane, as already discussed in the previous chapter when evaluating the vesicles elasticity aspects related to the AFM measurements. Within this context, the different origin of the cells used as CMVs sources might have an impact on CM composition and thus on membrane density, which is a key feature to consider when exploiting centrifugation for CM isolation, as in the present protocol. In particular, as underlined by Manni et al., the brain is enriched in phospholipids with polyunsaturated fatty acids (PUFAs), with a particular pattern in neurons, where the axon tip is enriched in phosphatidylcholine phospholipids containing arachidonate or docosahexaenoate [205]. Also in synaptic vesicles, PUFAs account for up to 70 mol% of the phospholipid pool [206]. Although the entity and the direction of the impact of the lipidic composition is still unclear, it has been found that the degree of acyl chain unsaturation affects membrane properties like curvature and packing density [207], which in turn might be responsible for a difference in CM sedimentation efficiency during the centrifugation of the two different homogenates. Moreover, another aspect that must be considered is that the cells used for the formulation of CMVs (GBM and CRC) differ not only in terms of tissue of origin but also in terms of culture type. Indeed, GBM primary cells deriving from human samples and CRC cells deriving from a murine cell line require very different culture conditions, which might influence the mechanical properties of their membranes [208].

To confirm the purity of the isolated CMs, the potentially detrimental presence of DNA or RNA was investigated. As shown in Figure 22 agarose gel electrophoresis allowed to

demonstrate that no genetic material contamination was present in the isolated membrane fraction.

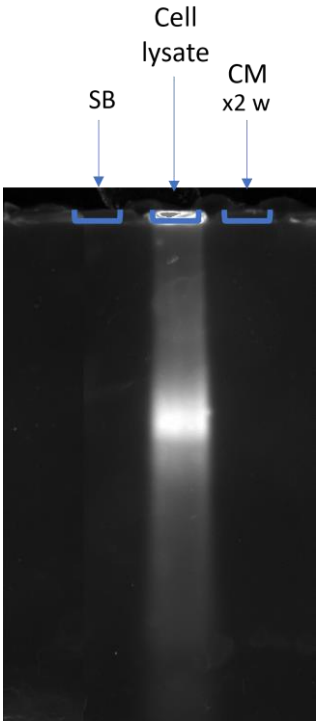

Figure 22: Scan of the agarose gel after electrophoresis. “SB” indicates the starting buffer, “Cell lysate” is the unprocessed cell homogenate, while “CM ×2 w” indicates the CMs isolated with the optimized protocol involving 2 washings with starting buffer (x2 w).

The CM isolation procedure, validated in the previous study using GBM cells, resulted effective in the present study as well, confirming its wide applicability to different cell types.

Protein retention in CM fraction and CMVs was evaluated both quantitatively and qualitatively. A micro-BCA assay was performed on resuspended CMs before and after extrusion (CMVs) for total protein quantification. BCA assay relies on the reduction of Cu^{2+} to Cu^{+}, due to the formation of a Cu^{2+}-protein complex in an alkaline environment. The chelate complex of peptide bonds with Cu^{2+} enables its reduction to Cu^{+} (Biuret reaction) which successively forms a water-soluble chelation complex with two molecules of BCA [209]. BCA-Cu^{+} chelate complex causes a colour change of the solution from green to purple, with a strong absorbance at 562 nm. The colour change is correlated to the amount of proteins in two ways: on one side, the reduction of Cu^{+} is proportional to the amount of proteins in the sample, and on the other side, the

bicinchoninic Cu^{+} complex formation is influenced by the presence of cysteine, tyrosine, and tryptophan side chains [210]. Therefore, to minimize the differences caused by unequal amino acid composition in different protein samples, the assay was performed at 60 °C, since elevated temperatures increase the exposure of amino acids, thus reducing structure influence on the test.

Moreover, as observed by Morton et al., phospholipids can induce considerable error in BCA assay results, thus compromising its reliability when measuring the protein content of proteolipids and biological membranes [211]. Indeed, in their work, the authors demonstrated the correlation of the overestimated protein values with the relative phospholipid content of the lipoprotein samples, and proposed an adaptation of the BCA protocol involving the addition of 2% SDS to the samples. The lipid interference was eliminated by the addition of SDS, allowing the application of the BCA assay to a wider range of samples. Therefore, given the high lipid presence in the CM fraction, a 2% SDS was added to the present samples for BCA protein quantification.

Sample	**Protein content (µg/mL)**
Isolated CM	162 ± 18
CMVs	10.1 ± 0.3

Table 5: Protein content of CM and CMVs measured by BCA assay. Both samples derived from 1.8 x 10^7 CT26 cells and were suspended in 800 µL.

As shown in Table 5, the retained protein concentration detected with this assay in CMs was 162 ± 18 µg/mL, which is consistent with the values of protein content reported in the literature for isolated CMs [48, 212]. Nevertheless, the protein conservation into CMVs, after extrusion of the CM suspension, resulted significantly lower. This sizable loss could be due to the hydrophilic interaction of proteins with the polycarbonate membrane filters used in the extrusion process, which are probably responsible for a general loss of material during the repeated passages through the filters, as further discussed in the following section.

Unfortunately, not many data were found in the literature assessing the protein amount in bio-mimetic systems formulation. In several studies describing the development of CM-deriving systems, proteins are quantified in the biologically derived fraction, but,

after the formulation process, only qualitative protein studies are performed, making the comparison with the protein retention result found herein, very difficult [50, 212].

Nevertheless, this result indicating a generic protein loss must be supported by a qualitative information, to determine which kinds of proteins are lost or retained, and whether this could affect the interaction of the vesicles with the target cancer cells.
With this aim, proteomic analysis was conducted on CMVs. In Table 6, a selection of the identified membrane proteins characterized by high relative abundance is reported, along with the cellular processes in which they are involved, according to the UniProt database.

Protein function	**Protein name**	**Gene name**	**Relative abundance (Log_2)**
Cell migration and adhesion	CD44 antigen	CD44	16.47
	Integrin alpha 3	ITGA3	15.38
	Vesicle-associated membrane protein 7	VAMP7	15.18
	Moesin	MSN	14.15
	Ras-related protein Ral-A	RALA	14.00
	Cadherin-2	CDH2	13.37
Cell signalling	Annexin A2	ANXA2	18.11
	Integrin alpha 6	ITGA6	15.60
	Plexin-B2	PLXNB2	15.00
	Neurogenic locus notch homolog protein 2	NOTCH2	13.26
Immune evasion	T-lymphocyte surface antigen Ly-9	LY9	11.86

Table 6: Proteomic analysis report of some of the most abundant membrane proteins found in CMVs from CT26. In the table the encoding genes, functions and relative abundance of each protein are also reported.

The proteomic analysis evidenced the conservation of proteins that are commonly overexpressed in tumor cells such as CD44, a non-kinase transmembrane glycoprotein [213] and Annexin A2, as already described in the previous chapter [160]. Moreover, characteristic antigens that resulted to play a role in CRC specific progression were identified with this analysis. Moesin, a cytoskeletal protein involved in cell motility, invasion and metastasis, has proved to be of prognostic significance in CRC progression [214]. Also Notch receptor overexpression was observed in CRC [215], as well as Ral-A receptor protein. The role of Ral-A and Ral-B small GTPases in promoting oncogenesis was illustrated in the work of Martin et al. They found upregulated Ral-A and Ral-B activation in CRC cell lines and demonstrated that Ral-A was involved in anchorage-independent cancer cell growth [216]. Moreover, the abundant presence of proteins implicated in mechanisms that are of particular interest for the aim of the present study was assessed, suggesting their potential positive impact on tumor targeting and penetration efficiency. Vesicle-associated membrane protein 7, involved in vesicle membrane fusion, and Integrin alpha 3, mediating cell migration, adhesion and matrix degradation, are representative examples.

4.3.2 Preparation and characterization of hybrid vesicles: comparison of two techniques

The hybridization of CMs with synthetic lipids was carried out following two different techniques: co-extrusion of cell-derived material with multilamellar synthetic vesicles was performed to obtain hybrids by extrusion (HEs), while hybrids by microfluidics (Hμs) resulted from the mixing of isolated CMs with an ethanolic solution of synthetic lipids through a micromixer. During co-extrusion, shear forces induce the rupture and deformation of large multilamellar vesicles, allowing fusion and reassembling of membranes [54]. An advantage of co-extrusion is the use of membrane filters with a determined pore size, which allow proper size control of the obtained particles. However, the extrusion method may be difficult to adapt to large-scale preparation, also due to the associated material loss [14].

Hydrodynamic mixing through microfluidic devices relies on mass transfer between the two phases, due to the formation of a turbulent flow within microchannels. It enables to minimize material loss and to precisely control and replicate formulation conditions,

hence allowing to scale up the procedure more easily [61]. In this work, NanoAssemblr® Spark™ system was used. This instrument operates using a pressure-driven mechanism, exerting the same pressure on two input wells of a cartridge, allowing the injection of the two phases into a toroid-type micromixer [217]. The pressure settings vary from 1 through 9; the exact pressure associated to each setting is not specified but they are selected depending on the volume of the two starting phases. In this work, setting 7 was selected.

The two components of hybrid formulations HE and Hμ were mixed in different CMs:synthetic lipids ratios, here expressed as mass ratio (w/w) of retained proteins:synthetic lipids. The tested ratios were 1:1.5 and 1:2.5 w/w, leading to the formulation of HE 1:1.5, HE 1:2.5, Hμ 1:1.5 and Hμ 1:2.5. The rationale behind the selection of these two mass ratios was the attempt of maintaining the discussed advantages related to CM-functionalization while increasing the production yield of bio-mimetic vesicles.

The results of the physico-chemical characterization, performed in water or PBS, are summarized in Table 7. HEs were first prepared in water, and their size, PDI and Z potential were determined. The preparation of Hμs was limited by costs issues, which motivated the decision of studying their physico-chemical properties and stability exclusively in PBS. Z-potential measured in PBS 1x was considered not reliable for any of the formulations developed, due to salts concentration and increased conductivity [218]. Thus, only size and PDI were monitored for hybrids stability study in PBS. All formulations resulted in monodisperse populations (PDI<0.25) of nano-sized vesicles. The surface charge of HEs resulted negative and comparable to the value obtained for CMVs. Hybrids did not show statistically significant differences in terms of hydrodynamic diameter (p>0.005), except for the formulation Hμ 1:1.5, which showed a larger size (p<0.005) and higher PDI, and for this reason it was not included in the following studies. The size of hybrids was slightly larger than CMVs (143 ± 5 nm, see Table 4). Hybrids stability was studied by monitoring size and PDI during 8 day-storage at 4 °C in PBS. As shown in Figure 23, the physico-chemical characteristics of the developed systems remained constant over the investigated period, demonstrating good stability under these conditions.

Formulation	Size (nm)	PDI	Z potential (mV)	Yield (x 10^3)
HE 1:1.5	151 ± 11	0.15 ± 0.04	-28 ± 3	7.6 ± 0.9
HE 1:2.5	153 ± 14	0.11 ± 0.02	-20 ± 5	9 ± 1
Hμ 1:1.5	257 ± 30	0.20 ± 0.03		10 ± 2
Hμ 1:2.5	176 ± 4	0.08 ± 0.06		16 ± 2

Table 7: Physico-chemical properties, concentration, and yield of two types of hybrids from CT26 cells, stored in water (HEs) or PBS (Hμs) at 4°C. Mean values ± standard deviation (n=5).

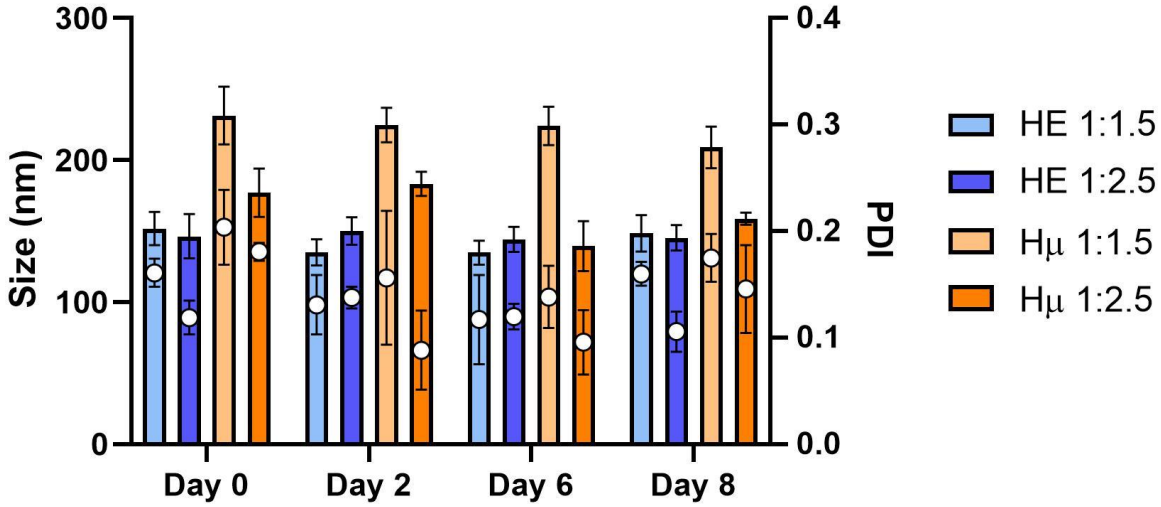

Figure 23: Physico-chemical properties of the two types of hybrids from CT26 cells, stored in PBS at 4°C. Mean values ± standard deviation (n=3).

As described for CMVs, the yield of the different production processes was calculated as the number of obtained vesicles (determined by NTA) per initial cell (Table 7). As expected, the insertion of synthetic lipids in hybrids formulation led to an increase in the production yield, if compared to CMVs, with a proportional trend following the increase in the amount of artificial lipids added. Moreover, although a good production yield was achieved for HEs, a significant increase in vesicle production was reached with the microfluidic technique, which might be reasonably responsible for a minor loss of starting materials.

Indeed, U.S. Pat. No. 4, 737, 323 revealed that the extrusion method has low throughput issues, due to membrane clogging (more common for “tortuous path” filters) and to the limited pore surface area, which constitutes the 20% of the total surface area of the membrane. Moreover, filter membranes are planar disks mounted against a flat mechanical support which further severely restricts the surface area available for extrusion and leads to low throughput [219].

The hypothesis of material loss affecting the extrusion process was further supported by the protein content measured in Hμ 1:2.5 by BCA assay.

Indeed, the protein quantified in the suspension of hybrids prepared by microfluidics, from approximately the same number of cells used to prepare CMVs (final protein concentration 10.1 ± 0.3 μg/mL), resulted to be 31.1 ± 0.2 μg/mL, demonstrating a higher protein conservation under the micromixing process.

A proteomic analysis was performed to further investigate the discrepancy in protein amount found in CMVs and Hμs, deriving from approximately the same number of CT26 cells.

This analysis confirmed the BCA result, since a higher number of protein groups was detected in hybrids compared to CMVs. Nevertheless, the same representative protein groups found in CMVs were also identified in Hμ, and their relative abundance is reported in Table 8, together with data related to CMVs for an easier comparison.

As shown in the table, the selected membrane proteins had a comparable relative abundance in the two samples, suggesting that the loss of material related to the extrusion procedure was somehow uniform, and did not affect the relative conservation of membrane proteins considered of superior interest.

Proteome databases, in particular the Cancer Surfaceome Atlas (http://fcgportal.org/TCSA) and UniProt, were employed to collect information for the present discussion. Indeed, few works developing bio-mimetic cell-derived systems report proteomic analysis on their final formulations. The most diffused qualitative studies to identify the retained proteins rely on SDS page electrophoresis followed by western blot [11, 22, 220], dot blot [48] or immuno-labelling with microspheres for TEM imaging [24]. However, being immuno-assays, these types of tests allow to evaluate the presence of single proteins by selecting specific antibodies, and do not consider all the

other antigens that might be unexpectedly found and might be equally important for an accurate characterization of the developed nanosystem.

Protein function	**Protein name**	**Gene name**	**Relative abundance (Log_2)** **CMVs**	**Relative abundance (Log_2)** **Hμ 1:2.5**
Cell migration and adhesion	CD44 antigen	CD44	16.47	14.94
	Integrin alpha 3	ITGA3	15.38	14.41
	Vesicle-associated membrane protein 7	VAMP7	15.18	13.63
	Moesin	MSN	14.15	14.28
	Ras-related protein Ral-A	RALA	14.00	13.11
	Cadherin-2	CDH2	13.37	13.21
Cell signalling	Annexin A2	ANXA2	18.11	17.91
	Integrin alpha 6	ITGA6	15.60	14.80
	Plexin-B2	PLXNB2	15.00	14.36
	Neurogenic locus notch homolog protein 2	NOTCH2	13.26	12.74
Immune evasion	T-lymphocyte surface antigen Ly-9	LY9	11.86	13.19

Table 8: Proteomic analysis report of some of the most abundant membrane proteins found in CMVs and Hμ prepared from CT26. In the table the encoding genes, functions, and relative abundance of each protein are also reported.

The morphology of HEs and Hμs was investigated by cryo-TEM. Within this particular transmission electron microscopy technique, the sample is deposited on a carbon supported copper grid as a thin film, and its vitrification is achieved by rapid plunging the grid into liquid ethane. The vitrified specimen is kept below -165 °C during storage,

transfer to the microscope, and investigation [221]. Differently from the staining process imposed by TEM, vitrification of the sample enables the preservation of the original shape of the observed objects, embedded in the pores of the carbon film inside a thin layer of amorphous ice. Besides NMR spectroscopy, cryo-TEM is the only technique able to differentiate between uni- and multi-lamellar vesicles [136], which constitutes another advantage over TEM, applied for the morphological study of the previously developed GBM-CMVs. In cryo-TEM micrographs, lipid vesicles appear as circular objects with strong contrast at the rim, due to the high projected thickness at the edges of the lipid bilayer shell [222].

As shown in Figure 24, round shaped vesicles surrounded by a phospholipid bilayer were clearly identified in both HE and Hμ samples, and no visible differences were observed for the two types of hybrids.

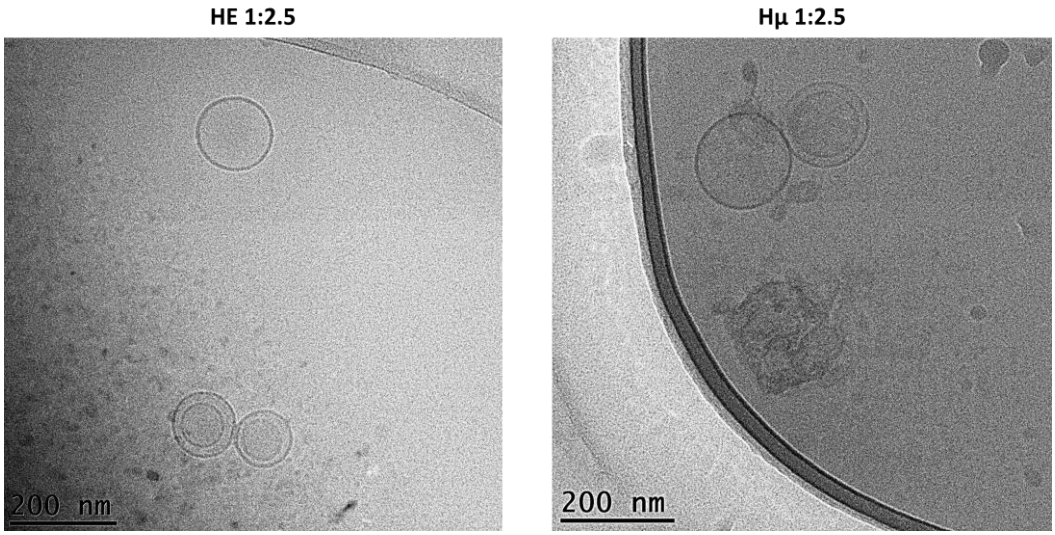

Figure 24: Representative cryo-TEM images of concentrated aliquots of HE and Hμ. Cryo-TEM analysis was performed on 3 different hybrid batches for each type of formulation.

The effective fusion of CMs with synthetic lipids was evaluated to exclude the hypothesis of the formation of distinct systems composed of the two fractions separately.

A FRET analysis was conducted on the two types of hybrids to investigate this aspect. This technique, frequently used to evaluate the effective membrane fusion in hybrid system characterization [48, 50, 212, 223], relies on the efficient energy transfer occurring between two specific fluorophores (“FRET pair”), when they are within a distance of approximately 10 nm. The efficiency of the energy transfer process varies in

proportion to the distance separating the donor and acceptor fluorophores constituting the FRET pair, consequently, FRET measurements can be exploited as an effective molecular ruler for determining distances between them [224]. The selected donor fluorophore must emit in a wavelength range which include the excitation frequency of the acceptor; if the complementary probe is sufficiently close, the radiation emitted by the excited donor will excite the acceptor, producing an increase in the measured fluorescence. Thus, when the distance between the two portions of the membrane decreases, the two fluorophores become closer, enabling the excited donor to irradiate the acceptor, inducing an increase of the FRET signal (Fig. 25).

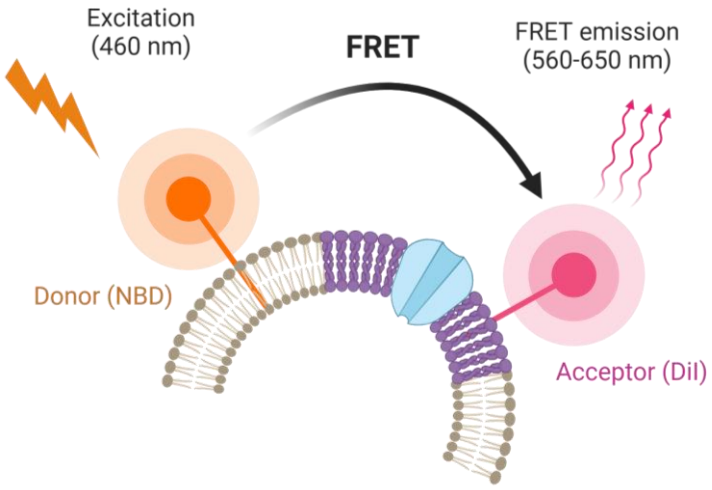

Figure 25: Schematic representation of FRET principles. Created with BioRender.com

Different strategies might be adopted to evaluate membrane fusion with FRET assays: several authors exploited the method of probes distancing, first described by Struck et al. [225]. This strategy involves the preparation of FRET liposomes labelling the phospholipid bilayer with both the donor and the acceptor probes, and the detection of a minimized emitted fluorescence from the excitation of the donor, due to its proximity with the acceptor. When hybridization with unlabelled CMs is successful, this transfer of energy, acting as quenching, is diminished, resulting in an increase in the fluorescence emission from the donor [48, 50, 212].

In contrast, van den Bogaart et al., studying the membrane fusion mediated by SNARE proteins, differently labelled the two membranes involved in the fusion process and measured the increase of the fluorescence emission from the acceptor, excited by the

excitation emission of the donor, due to the fluorophores approaching [226]. In this way, the test is less affected by other factors independent from CM insertion, which, in contrast, could interfere in FRET measurements using the "probe distancing" method. Indeed, using the probe distancing approach, the energy transfer effect measured in a FRET liposome might be impaired by many variables hardly monitored, such as lipids arrangement during extrusion, leading to a potential misrepresentation within the assay. For this reason, this approach was considered less reliable, and the "aproaching probes" method was consequently selected for the present study.

For the evaluation of membrane fusion in HEs and Hμs, FRET-hybrids were prepared by labelling the synthetic lipids and the CM portions with a fluorescence donor (NBD-PE) and a fluorescence acceptor (CM-DiI), respectively, and hybridizing the components using the two described methods. By exciting the sample at the specific donor excitation wavelength, the fluorescence emitted by the acceptor was measured and compared to the one measured in the physical mixture of the two labelled components (DiI-CMVs and NBD-liposomes). As shown in Figure 26, for both types of production techniques, the FRET signal produced by hybrids was sensibly higher than the one deriving from the physical mixture. However, the fluorescence emitted by Hμs resulted significantly higher than the signal of HEs, assessing a more efficient membrane fusion obtained through microfluidics.

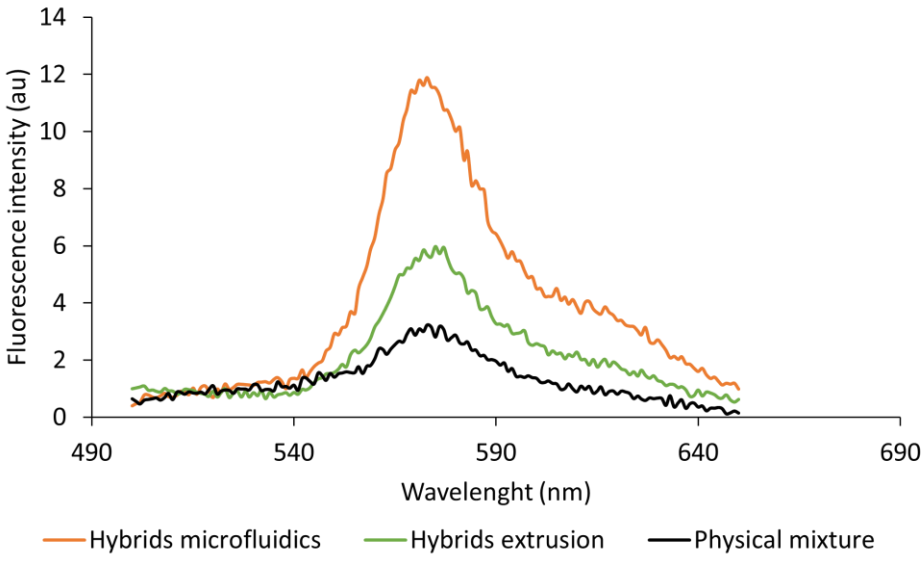

Figure 26: FRET study of the two types of hybrids. Incident radiation λ=460 nm.

4.3.3 *In vitro* studies on parent and different cell lines

Similarly to the study performed on GBM-derived CMVs, *in vitro* internalization efficiency was investigated also on CMVs and hybrids deriving from CT26 cell line. Hybrids with the better yield of production (HE 1:2.5 and Hμ 1:2.5) were selected for *in vitro* experiments. Confocal microscopy and flow cytometry were employed to evaluate CMVs and hybrids cellular internalization efficiency compared to synthetic liposomes. Stealth liposomes were used as an artificial control likewise in the previous study on GBM-CMVs, and their preparation and Cy5-labelling were performed as described in the experimental section. Their physico-chemical characteristics resulted analogue to what obtained for DiI-labelled liposomes used in GBM-CMVs *in vitro* experiments, with a hydrodynamic diameter of 141 ± 3 nm, PDI of 0.06 ± 0.03, and a negative surface charge of -26 ± 3 mV. In a preliminary study, CM-derived systems as well as synthetic liposomes (all fluorescently labelled) were incubated with parent CRC cells at two time points; the cells were then fixed, stained and imaged by confocal microscopy. The same study was performed on live cells by flow cytometry at longer times, to support the qualitative result of confocal images with a quantitative analysis. All vesicles were incubated with the cells at the same concentration.

Confocal imaging, shown in Figure 27A, demonstrated good internalization of CMVs and hybrids into the originating cells, already after 30 min-incubation. On the contrary, as already observed with GBM cells, liposomes scarcely interacted with CT26 cells at the studied time points, which supports the hypothesis of an important implication of the inserted CM portion, in the interaction of the hybrids with the parent cells.

In this test, CMs and artificial lipids used to prepare hybrids were also labelled with different fluorophores, in order to observe their co-localization as a further confirmation of the successful fusion of the two membrane components. The colocalization is displayed in the images in Figure 27A as purple colour, resulting from the superimposition of red CMs (labelled with Cy5-PE) and blue synthetic lipids (labelled with Rhd-PE), providing further qualitative evidence of the efficient hybridization.

FACS analysis was performed on CT26 cells treated with Cy5-labelled CMVs and the two types of hybrids, to quantitatively evaluate the different efficacy of internalization of the developed vesicles. Dead cells were excluded from the analysis by staining the samples

with LIVE/DEAD® dye. In Figure 27B, the results of FACS analysis are expressed as the mean percentage ratio of the number of Cy5-positive cells to the total live cells detected by the instrument for each sample (3 samples each replicate). The figure highlights that at both time points the internalization of Hμs into CT26 cells was significantly higher (p<0.005) than the value detected for the internalization of HEs. Moreover, CMVs showed a faster internalization into parent cells compared to hybrids. Whereas the superior internalization of CMVs can be explained by their whole CM composition, the higher internalization of Hμs evidenced a better homologous uptake of the microfluidic-formulated system, having the same CM composition of HEs. Functional proteins and lipids retained during formulation by microfluidics and lost during extrusion might possibly have a role in the improved internalization efficiency of Hμs.

It is important to remind that, as indicated in the experimental section, cells were incubated with the same concentration of vesicles, taking into account the aforementioned different production yield, which justified the use of different amounts of CMs for the preparation of vesicles for *in vitro* studies.

Moreover, the results obtained with FACS analysis evidenced a decrease in percentage of fluorescent cells after 24 h of incubation with labelled vesicles (Fig 27B). However, at longer time points, the proliferation rate of the studied cell lines has to be considered. Indeed, CT26 cells exhibit a high proliferation rate, leading to their duplication in 24 h of culture. Consequently, considering CMVs uptake pattern, since after 2 h of incubation the 88 ± 6 % of CT26 cells internalized the vesicles, after 24 h half of the analysed sample would be composed of newly divided cells, which lost CMVs-related fluorescence. For this reason, internalization quantification at this time point might not provide significant information, thus shorter time points were considered in the following studies.

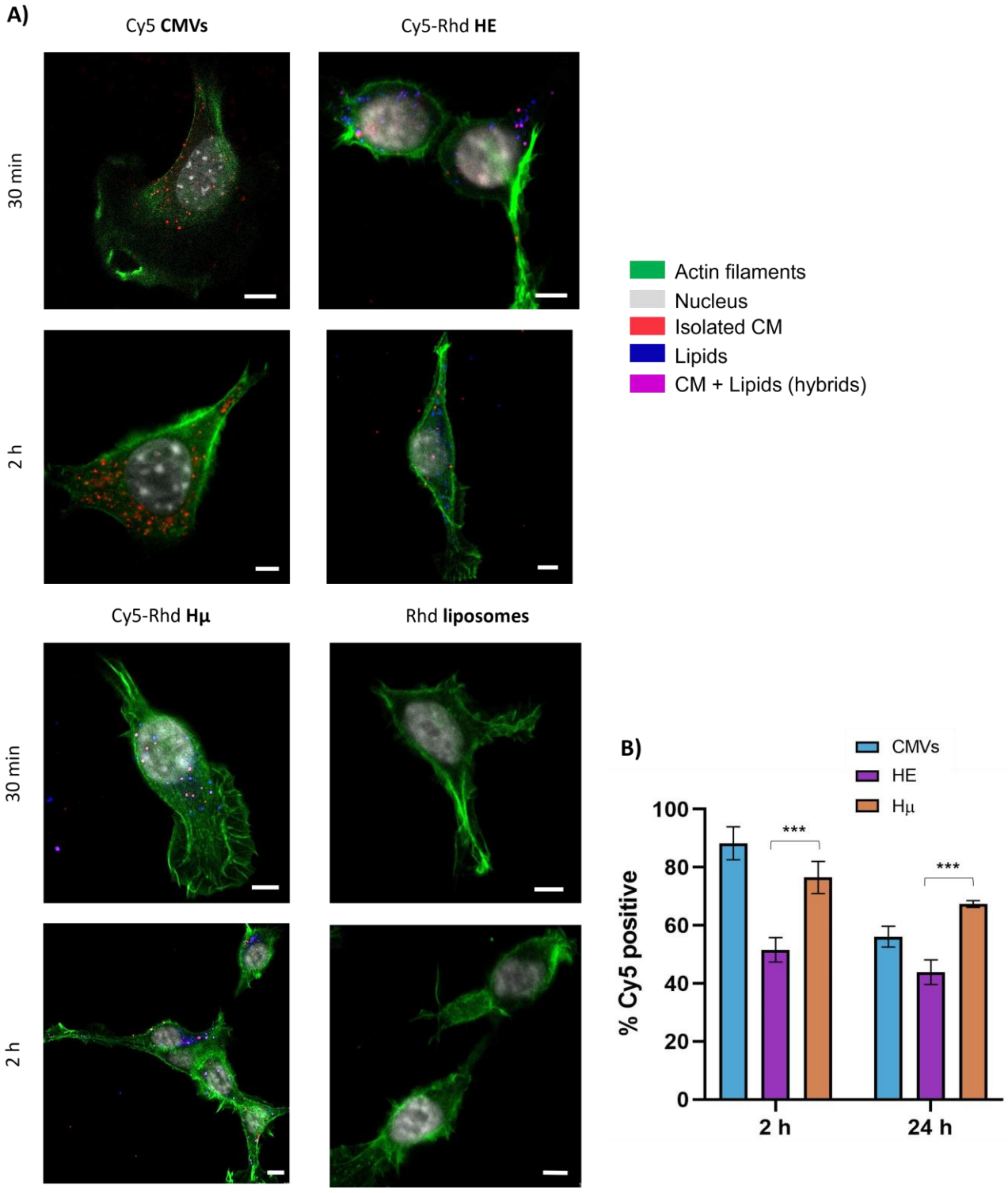

Figure 27: (A) Confocal images of Cy5-CMVs, Cy5-Rhd-HEs, Cy5-Rhd-Hμs and Rhd-liposomes, incubated with parent CT26 cells for 30 minutes and 2 h. Scale bar = 5 μm (B) FACS analysis of CT26 cells incubated with Cy5-CMVs, Cy5-HEs and Cy5-Hμs for 2 h and 24 h. Results expressed as the percentage ratio of the number of Cy5-positive cells onto the total of live cells (minimum threshold 10000 events per analysis). Each experiment was repeated in three biologically independent replicates and results are expressed as mean ± SD. ***= p<0.005

Given the promising results obtained for Hμ 1:2.5 on originating cells, this formulation was chosen for the *in vitro* studies of selective internalization into parent cells compared to different cell lines. Different types of murine immortalized cell lines were selected for this assay: besides the parent CT26 cells, ovarian epithelial cancer cells (ID8) and healthy myoblasts (C2C12) were incubated with Cy5-labelled CMVs, Hμs and synthetic liposomes. The Cy5 fluorescence signal was recorded after 30 min and 2 h of incubation and also in this case only live cells were considered for data analysis. As shown in Figure 28, a time-dependent and very rapid uptake of CMVs and Hμs was observed in their source cells, reaching 88 ± 5 % and 76 ± 6 % of internalization respectively, at 2 h. This result was predictable based on confocal microscopy observations, and confirmed the results of the preliminary FACS analysis.

Surprisingly, after 2 h-incubation, a 48 ± 5 % and a 52 ± 15 % positivity to hybrid fluorescence was also detected in ID8 and C2C12 cells respectively. At the same time point, CMVs internalization remained under 30 % in non-parent cells. The unexpected considerable heterologous internalization of hybrids might suggest the implication of CM proteins and lipids that are retained with microfluidic technique, but lost with extrusion, in the vesicle internalization process in non-parent cells. Following another hypothesis, synthetic lipids might confer to hybrids particular mechanical properties, favouring aspecific cellular uptake. This interesting aspect would be efficiently investigated with AFM.

Nevertheless, although *in vitro* separate cellular uptake studies represent valid preliminar indicators of vesicles selectivity, co-cultures of different cells or *in vivo* biodistribution studies would certainly be more reliable to investigate the targeting abilities towards homologous cells or other cell types, of the developed systems.

As evidenced in the study on GBM, also in the case of CT26-derived CMVs, the parent cells better internalized both CMVs and hybrids, compared to the other cell lines, supporting the hypothesis of the involvement of specific membrane proteins in favouring the interaction with the parent cells.

Moreover, all the cell lines treated with synthetic liposomes had similar weak fluorescence signals (less than 2%), corroborating the hypothesis that the decoration with cell membranes endowed the vesicles with faster and higher uptake *in vitro*.

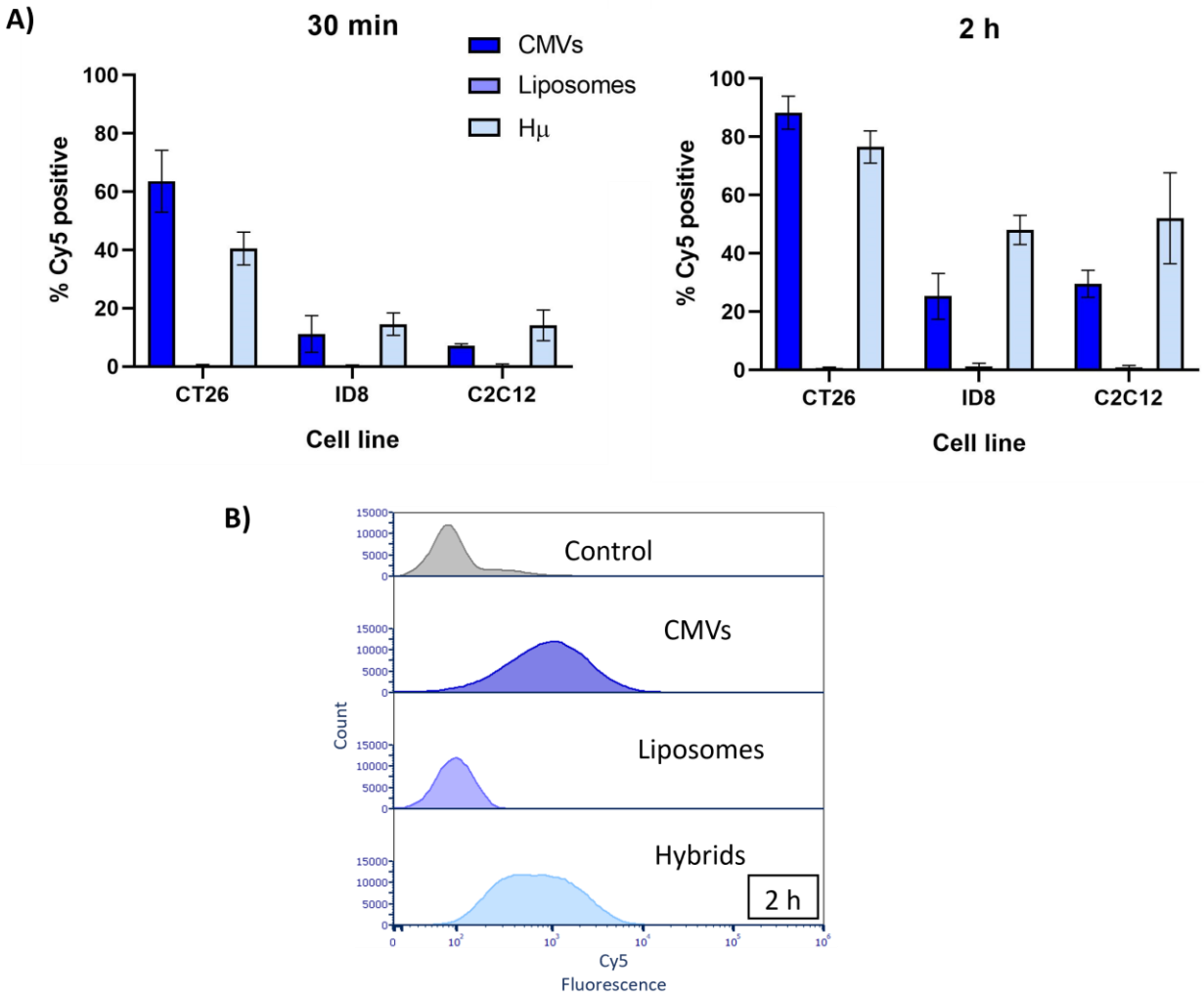

Figure 28: Cellular internalization study via flow cytometry: (A) Mean % fluorescence positivity on total live cells treated with Cy5-labelled CMVs, Hμ 1:2.5 and liposomes, at 30 min or 2 h incubation; (B) Cy5 fluorescence intensity shift in treated and untreated samples. Each experiment was repeated in three biologically independent replicates and results are expressed as mean ± SD.

A similar result was obtained by Liu et al., who coated SiO_2 NPs with CT26-deriving CMs either neat or hybridized with synthetic liposomes [227]. Analogously to the present study, to evaluate the selective uptake of their nanosystems, the authors incubated CM-SiO_2 NPs, hybrid membrane-SiO_2 NPs (H-SiO2) and synthetic lipids-coated SiO_2 NPs (L-SiO_2) with three different cell lines, namely parent cells (CT26), HeLa human cervical carcinoma and MCF-7 human breast cancer cells. After 4 h of incubation, using flow cytometry, they evidenced high internalization of CM-SiO_2 and H-SiO_2 into parent cells, and observed also an overall higher uptake of the two systems compared to L-SiO_2 in all the considered cell lines. Noteworthy, they observed higher uptake of H-SiO_2 compared

to CM-SiO_2 in the analysed cell lines, which is consistent with the results obtained in the present work.

A comparison between the internalization efficiency of the systems presented by the authors and the ones developed herein must take into account the different nature of the considered particles, which exhibit different structure and mechanical properties, leading to different mechanisms exploited for the interaction with the cell. Indeed, the authors ascribed the differences in cellular uptake to the different rate of SiO_2 NPs coating related to their developed systems, which is not applicable to the present discussion.

However, the increased vesicle uptake into different cell lines due to CM insertion is objective, noticeable not only in the parent cells but also into other cell types, although to a minor extent.

The biocompatibility of CMVs and Hμ 1:2.5 was investigated in two diverse *in vitro* models. Crystal violet was used to assess cell viability on 2D healthy myoblasts cell culture (C2C12 cell line), treated with different concentrations of vesicles, and incubated for 72 h. This colorimetric test allowed to indirectly quantify cell death through the determination of the adherence of cells, relying on the staining of attached cells with crystal violet, which binds to proteins and DNA. The dead cells lose their ability to adhere, and thus they are removed from the well prior to crystal violet treatment, causing the reduction of the amount of dye revealed in the cell culture. The bound dye is extracted from the viable cells using methanol, and the absorbance of the solution is measured. The cell viability % was calculated in relation to untreated control cells (whose absorbance was considered as 100% of cell viability) and reported in Figure 29. All vesicles under study resulted to be totally biocompatible at both concentrations tested, since the cell viability of treated cells was not significantly different from the control (p>0.4).

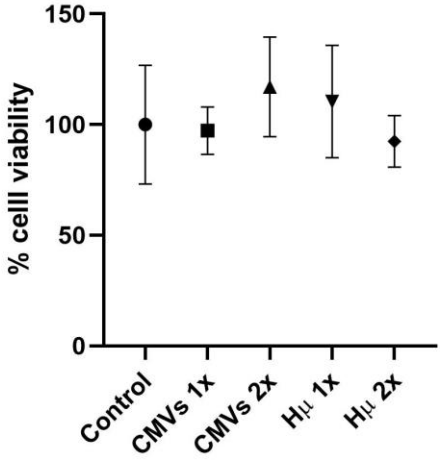

Figure 29: Biocompatibility study. (A) Cell viability of C2C12 cells incubated with CMVs and Hμs, and treated with crystal violet after 72 h. Results expressed as mean ± SD of 6 replicates.

Moreover, the potential effect of Hμ 1:2.5 on the regeneration ability of 3D healthy murine colon organoids was evaluated by monitoring the 3D sample morphology and size during 8 day-treatment.

Organoids are self-organized 3D tissues typically derived from stem cells (pluripotent, fetal or adult), mimicking the key functional, structural and biological complexity of an organ [228]. Stem cells play a fundamental role in maintaining organ structure and function through cellular renewal, migration, differentiation and apoptosis [229], which make them suitable candidates for the construction of an *in vitro* 3D organ model.

Compared to conventional 2D cultures, organoid cultures reproduce *in vitro* the typical *in vivo* tissue-like structures and functions, containing small populations of genomically stable, self-renewing stem cells that give rise to fully differentiated progeny at frequencies similar to those in living tissues [230]. Moreover, organoid cultures are more accessible for manipulation and in-depth biological studies than animal models and they enable patient specificity. Therefore, organoid cultures have been studied for a wide variety of applications including drug discovery [231], personalized diagnostics [232] and cell therapy [233]. Cells comprising organoids can be derived from induced pluripotent stem cells or from tissue-derived cells, as in the case of the organoids exploited in the present study. Tissue-derived organoids are produced from isolated fragments of tissue from the corresponding organ, originating from humans or animals. Within these

models, the cells expand in culture for prolonged time, while retaining their genetic stability and the peculiarity of their tissue of origin [234].

In the present study, intestinal organoids were employed to mimic the *in vivo* response to the potential administration of the developed vesicles. Intestinal organoids are among the first organoid types successfully established *in vitro* [235]. Their effective establishment is related to their characteristic architecture, exhibiting proper branching morphology with constant multicellular composition [236]. It has been demonstrated that intestinal organoids, cultured in Matrigel with a suitably supplemented medium, are able to proliferate *in vitro* for more than a year, overcoming the Hayflick limit, which indicates that primary non-transformed cells can only divide 40–60 times (about 2-3 months) prior to undergoing senescence [228]. Furthermore, they were demonstrated to retain their ability to generate different intestinal epithelial cells *in vitro* [237]. Generally, for their preparation, the samples of intestinal tissue are opened, washed, and then chopped into 2-4 mm fragments, to maximize the surface area available for enzymatic digestion or additional mechanical dissociation, to finally isolate individual intestinal stem cells. The collected stem cells undergo multiple rounds of washing and purification before being seeded to create and grow organoid cultures [234].

For the present experiment, organoids from the intestinal tissue of a healthy mouse were cultured for 40 days and then disassembled (day 0 of the experiment) to allow the investigation on tissue regeneration and the potential effect of Hμs on this process. Hμs at two concentrations and oxaliplatin at a toxic concentration, used as positive control, were added to the culture medium the day after the disassembling procedure (day 1), while the medium was renewed for control organoids (negative control). Size monitoring was performed by optical microscopy, following the same organoids at day 1 (before the treatment), 5 and 8, and by measuring the surface area of the samples using ImaJ software. 5 organoids per condition were monitored along the study and the mean surface area of organoids treated in the same conditions was calculated. In Figure 30A, the growth of organoids is described as the size increase in relation to sample size at day 1, while in Figure 30B some representative pictures of selected organoids are shown. The regular morphology and constant growth of Hμ-treated organoids, compared to the positive and negative control, demonstrated the biocompatibility of the developed

system. Indeed, while the toxic concentration of oxaliplatin effectively impaired organoid growth, leading to their disassembly after 6 days, untreated and Hμ-treated organoids grew regularly reaching a 6 fold-increase in size along the considered period.

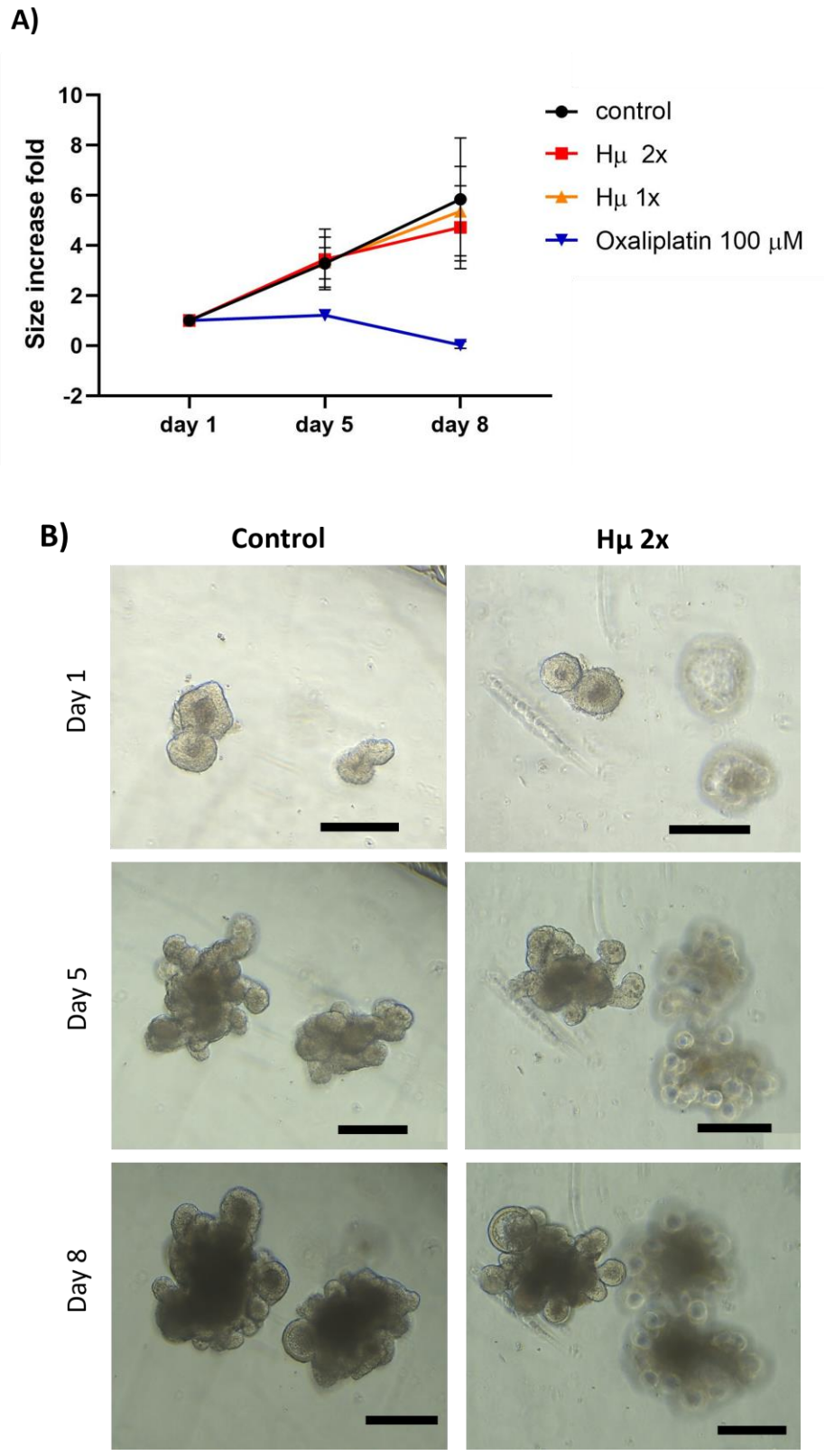

Figure 30: (A) Healthy organoid surface area, normalized by sample size at day 1, expressed as mean surface value ± SD of 5 considered samples. (B) Images of untreated and Hμ-treated organoids. Scale bar = 200 μm.
For both studies: (1x) = 1.4 x 10^{10} particles/mL; (2x) = 2.8 x 10^{10} particles/mL.

4.4 Conclusions

Three CM-derived bio-mimetic nanosystems were developed and thoroughly characterized. All formulations resulted stable and nano-sized, with a negative surface charge, demonstrating their suitability as drug delivery systems. The purification from potential carcinogenic genetic material was assessed, validating the CM isolation procedure also for cells deriving from immortalized cell lines. A considerable loss of material related to the extrusion process for CMVs and HEs preparation was demonstrated on one side by the lower amount of proteins detected in CMVs compared to Hμs, and on the other side by the lower yield of production evidenced for CMVs and HEs, compared to Hμs. Nevertheless, this loss of material appeared to involve all kinds of proteins to a similar extent, considering the consistency of the protein relative abundances detected with proteomic analysis in CMVs and Hμs.

Extrusion resulted also less effective than microfluidics in terms of hybrids membrane fusion, as revealed by FRET study.

All the developed systems showed good affinity for parent cells, although CMVs and Hμs showed higher internalization in this type of cells, compared to HEs.

CMVs also showed a selective uptake towards parent cells compared to different cell lines, while an unexpected non-specific internalization was observed for Hμ after 2h-incubation.

CMVs and Hμs showed no significant cytotoxicity on 2D cultured healthy myoblasts, and Hμs did not appear to affect intestinal tissue regeneration, as observed in a 3D organoid model study, demonstrating the biocompatibility of the developed nanosystems.

5. General discussion and conclusions

5. General discussion and conclusions

A lot of interest has arisen towards cell membranes as functional coating for nanoparticles or constituent of vesicles for cancer therapy [11]. The innovation related to this strategy relies on the unique and easy reproduction of extremely intricate biological functions to provide important features to the nanovehicle such as homologous targeting abilities and immune clearance evasion, resulting in long blood circulation, thanks to the conservation of "markers of self" from the source cells [238].

To this aim, different cell types have been investigated as well as various technological approaches [14], and particular interest was sparked by the use of microfluidic techniques, due to their unique performances related to production yield and control on the final characteristics of the nanosystems [62, 63].

My Ph.D. work focused on the development of tumor-targeted bio-mimetic vesicles, composed of cancer cell membranes, with the aim of reproducing the excellent homologous targeting efficacy observed when achieving specific antigens conservation on vesicles surface [11, 22]. CMs were extracted from different parent cell types: primary human GBM cells were cultured from patients' biopsies for GBM-CMVs, and a murine CRC cell line was used for the preparation of CRC-CMVs and hybrids, obtained from the fusion of CMVs with synthetic lipids.

A procedure for CM isolation from a cell lysate was developed and validated in terms of purification from potentially cancerous genetic materials for both cell types, and extrusion was performed to yield CMVs.

The protein profile of CMVs from GBM and CRC cells was thoroughly investigated, evidencing the successful retention of membrane proteins characteristic of the originating cells and possibly involved in cancer cellular mechanisms of particular interest.

The physico-chemical characteristics of CMVs deriving from the two cell types were comparable and stable over time.

The yield for CMVs production was evaluated through NTA, resulting in slightly different throughput related to the different parent cells: CMVs were obtained in a lower yield from GBM primary cells compared to CRC cell line. The differences in mechanical

properties and chemical composition of CM deriving from diverse cell types and cultures might contribute to this result.

Both GBM- and CRC-CMVs showed high and selective internalization rate into parent cells and no cytotoxicity towards various cell types.

With the intent of increasing the production yield of these promising bio-mimetic nanosystems, synthetic lipids were introduced in CRC-CMVs exploiting co-extrusion and micromixing through a microfluidic device, and a critical comparison of the two obtained systems was carried out. In both cases, hybridization of CMs with artificial lipids allowed to increase the number of bio-mimetic vesicles obtained, compared to CMVs gained from the same amount of parent cells. Nevertheless, the use of the microfluidic technology was associated with a higher throughput of hybrids production in terms of number of vesicles as well as protein retention from the originating cells. Moreover, a more efficient membrane fusion was observed for hybrids produced by micromixing compared to co-extrusion. Finally, hybrids obtained by microfluidics showed better internalization into parent cells compared to their extruded counterparts, along with remarkable selectivity when considering the vesicle uptake in different cell lines.

The biocompatibility of hybrids by microfluidics was investigated on 2D cultured murine healthy myoblasts and on 3D intestinal murine organoids, considered more reliable in reproducing *in vivo* conditions. Neither cytotoxicity on 2D cell cultures nor organoid growth inhibition were associated with hybrids treatment.

In conclusion, a protocol for the preparation of stable CM-deriving bio-mimetic vesicles was successfully developed, and their physico-chemical characteristics, as well as their composition and mechanical properties were thoroughly investigated. The demonstrated safety and internalization efficiency of the developed CMVs and hybrids make them novel potential drug vehicles for cancer therapy.

Future studies will focus on the development of a standard protocol for the loading of anticancer agents for radiotherapy or chemotherapy into CMVs and hybrids from different cell types. Once the protocol for vesicles development and loading will be standardized, *in vitro* and *in vivo* anticancer activity studies will be performed to evaluate the potential impact of this bio-mimetic platforms in cancer therapy.

List of abbreviations

5-FU: 5-Fluorouracil

AFM: Atomic force microscopy

APTES: (3-aminopropyl) triethoxysilane

BCA: Bicinchoninic acid

BNCT: Boron neutron capture therapy

BPA: (L)-4-dihydroxyborylphenylalanine

BPA-fr: BPA-fructose complex

BSH: Sodium borocaptate

CIN: Chromosomal instability

CM: Cell membrane

CM-DiI: 1,1'-Dioctadecyl-3,3,3',3'-tetramethylindocarbocyanine iodide

CMVs: Cell membrane derived vesicles

CRC: Colorectal cancer

Cryo-TEM: Cryogenic transmission electron microscopy

CTCs: Circulating tumor cells

CT: Computed tomography

Cy5-PE: Cyanine5-phosphatidylethanolamine

DIA: Data independent acquisition

DLS: Dynamic light scattering

DMEM: Dulbecco’s modified eagle medium

DMPC: 1,2-Dimyristoylphosphatidylcholine

DMPG: 1,2-Dimyristoylphosphatidylglycerol

DSPC: 1,2-distearoyl-sn-glycero-3-phosphocholine

DSPE-PEG2000: 1,2-distearoyl-sn-glycero-3-phosphoethanolamine-N-[methoxy(polyethylene glycol)-2000]

EGFR: Epidermal growth factor receptor

FACS: Fluorescence-activated cell sorting

FBS: Fetal bovine serum

FDG-PET: (F18)-fluorodeoxyglucose-positron emission tomography

FRR: Flow rate ratio

GBM: Glioblastoma

Hμs: Hybrids by microfluidics

HEs: Hybrids by extrusion

HLA: Human leukocyte antigen

HSP: Heat shock protein

Lipo BPA: BPA-loaded liposomes

Lipo BPA-fr: BPA-fr-loaded liposomes

MGMT: O6-methylguanine-DNA methyltransferase

MIN: Microsatellite instability

miRNA: Micro RNA

MOF: Metal organic framework

MRI: Magnetic resonance imaging

mRNA: Messenger RNA

MRS: Magnetic resonance spectroscopy

NBD-PE: Nitrobenzoxadiazole-phosphatidylethanolamine

NP: Nanoparticle

NTA: Nanoparticle tracking analysis

PC: Phosphatidylcholine

PLGA: Poly (lactic-co-glycolic acid)

PSPD: Position-sensitive photo diode

PUFAs: Polyunsaturated fatty acids

Rhd-PE: Rhodamine-phosphatidylethanolamine

RI: Refractive index

SAR: Split-and-recombine method

SB: Starting buffer

SDS: Sodium dodecyl sulphate

SEC: Size exclusion chromatography

SHM: Staggered herringbone micromixers

siRNA: Small interfering RNA

TDCs: Tissue-derived cells

TEM: Transmission electron microscopy

TFR: Total flow rate

TRAIL: Tumor necrosis factor-related apoptosis-inducing ligand

VEGF: Vascular-endothelial growth factor

WR: Working reagent

ZIF-8: Zeolitic imidazolate framework-8

Acknowledgements

I want to thank all the people that I met within my Ph. D. and who contributed to make this experience complete.

Special thanks go to my research group from the University of Genoa, Prof. Gabriele Caviglioli, Prof. Giorgia Ailuno and Prof. Sara Baldassari. I thank them for the dedication and passion they put in the projects and that they imparted me during these three years. I also thank Giorgia Ailuno, Valeria Iobbi and Daniela Donghia for their sincere friendship.

I want to thank Prof. Giovanna Lollo from the University of Lyon for allowing me to work in her lab and to expand my expertise in many fields; I also thank her for the inspiring approach to research I could experience in her lab during my visiting period. Special thanks go to Mathieu Repellin and Giuseppina Catania for their commitment, their kind help and for welcoming me.

I thank the research group of Prof. Tullio Florio from the University of Genova for the in vitro studies with glioblastoma cells; Prof. Ornella Cavalleri and her collaborators Prof. Paolo Canepa and Dott. Andrea Lagomarsino for FRET, AFM and confocal microscopy within glioblastoma study; Prof. Giuliana Drava for the ICP analysis; Prof. Andrea Petretto for the proteomic analysis; Prof. Katia Cortese for TEM analysis, Pierre Yves Dugas for Cryo-TEM imaging and Prof. Cédric Chaveroux for the organoids experiments.

I finally thank the doctoral board and the coordinator Prof. Renata Riva for the Ph. D. program I had the opportunity to be part of.

References

[1] G. Ailuno, S. Baldassari, F. Lai, T. Florio, G. Caviglioli, Exosomes and Extracellular Vesicles as Emerging Theranostic Platforms in Cancer Research, Cells, 9 (2020).

[2] M. Colombo, G. Raposo, C. Théry, Biogenesis, Secretion, and Intercellular Interactions of Exosomes and Other Extracellular Vesicles, Annual Review of Cell and Developmental Biology, Vol 30, 30 (2014) 255-289.

[3] A.A. Patil, W.J. Rhee, Exosomes: Biogenesis, Composition, Functions, and Their Role in Pre-metastatic Niche Formation, Biotechnology and Bioprocess Engineering, 24 (2019) 689-701.

[4] G. Pontecorvi, M. Bellenghi, R. Puglisi, A. Carè, G. Mattia, Tumor-derived extracellular vesicles and microRNAs: Functional roles, diagnostic, prognostic and therapeutic options, Cytokine & Growth Factor Reviews, 51 (2020) 75-83.

[5] S.G. Antimisiaris, S. Mourtas, A. Marazioti, Exosomes and Exosome-Inspired Vesicles for Targeted Drug Delivery, Pharmaceutics, 10 (2018).

[6] A. Abak, A. Abhari, S. Rahimzadeh, Exosomes in cancer: small vesicular transporters for cancer progression and metastasis, biomarkers in cancer therapeutics, Peerj, 6 (2018).

[7] K.B. Johnsen, J.M. Gudbergsson, M.N. Skov, L. Pilgaard, T. Moos, M. Duroux, A comprehensive overview of exosomes as drug delivery vehicles - Endogenous nanocarriers for targeted cancer therapy, Biochimica Et Biophysica Acta-Reviews on Cancer, 1846 (2014) 75-87.

[8] Y.F. Zhang, J.B. Shi, C. Li, Small extracellular vesicle loading systems in cancer therapy: Current status and the way forward, Cytotherapy, 21 (2019) 1122-1136.

[9] A.V. Vlassov, S. Magdaleno, R. Setterquist, R. Conrad, Exosomes: Current knowledge of their composition, biological functions, and diagnostic and therapeutic potentials, Biochimica Et Biophysica Acta-General Subjects, 1820 (2012) 940-948.

[10] M. Lu, Y.Y. Huang, Bioinspired exosome-like therapeutics and delivery nanoplatforms, Biomaterials, 242 (2020).

[11] J.Y. Zhu, D.W. Zheng, M.K. Zhang, W.Y. Yu, W.X. Qiu, J.J. Hu, J. Feng, X.Z. Zhang, Preferential Cancer Cell Self-Recognition and Tumor Self-Targeting by Coating Nanoparticles with Homotypic Cancer Cell Membranes, Nano Letters, 16 (2016) 5895-5901.

[12] S.Y. Liu, Y.W. Zhang, M. Li, L. Xiong, Z.J. Zhang, X.H. Yang, X.X. He, K.M. Wang, J.B. Liu, S. Mann, Enzyme-mediated nitric oxide production in vasoactive erythrocyte membrane-enclosed coacervate protocells, Nature Chemistry, 12 (2020) 1165.

[13] L. Rao, B. Cai, L.L. Bu, Q.Q. Liao, S.S. Guo, X.Z. Zhao, W.F. Dong, W. Liu, Microfluidic Electroporation-Facilitated Synthesis of Erythrocyte Membrane-Coated Magnetic Nanoparticles for Enhanced Imaging-Guided Cancer Therapy, Acs Nano, 11 (2017) 3496-3505.

[14] M.S. Abesekara, Y. Chau, Recent advances in surface modification of micro- and nano-scale biomaterials with biological membranes and biomolecules, Frontiers in Bioengineering and Biotechnology, 10 (2022).

[15] S. Aryal, C.M.J. Hu, R.H. Fang, D. Dehaini, C. Carpenter, D.E. Zhang, L.F. Zhang, Erythrocyte membrane-cloaked polymeric nanoparticles for controlled drug loading and release, Nanomedicine, 8 (2013) 1271-1280.

[16] C.M.J. Hu, R.H. Fang, B.T. Luk, K.N.H. Chen, C. Carpenter, W.W. Gao, K. Zhang, L.F. Zhang, 'Marker-of-self' functionalization of nanoscale particles through a top-down cellular membrane coating approach, Nanoscale, 5 (2013) 2664-2668.

[17] R. Molinaro, C. Corbo, J.O. Martinez, F. Taraballi, M. Evangelopoulos, S. Minardi, I.K. Yazdi, P. Zhao, E. De Rosa, M.B. Sherman, A. De Vita, N.E.T. Furman, X. Wang, A. Parodi, E. Tasciotti, Biomimetic proteolipid vesicles for targeting inflamed tissues, Nature Materials, 15 (2016) 1037-1046.

[18] J.O. Martinez, R. Molinaro, K.A. Hartman, C. Boada, R. Sukhovershin, E. De Rosa, D. Kirui, S.R. Zhang, M. Evangelopoulos, A.M. Carter, J.A. Bibb, J.P. Cooke, E. Tasciotti, Biomimetic nanoparticles with enhanced affinity towards activated endothelium as versatile tools for theranostic drug delivery, Theranostics, 8 (2018) 1131-1145.

[19] A. Parodi, N. Quattrocchi, A.L. van de Ven, C. Chiappini, M. Evangelopoulos, J.O. Martinez, B.S. Brown, S.Z. Khaled, I.K. Yazdi, M. Vittoria Enzo, L. Isenhart, M. Ferrari, E. Tasciotti, Synthetic nanoparticles functionalized with biomimetic leukocyte membranes possess cell-like functions, Nature Nanotechnology, 8 (2013) 61-68.

[20] R. Palomba, A. Parodi, M. Evangelopoulos, S. Acciardo, C. Corbo, E. de Rosa, I.K. Yazdi, S. Scaria, R. Molinaro, N.E.T. Furman, J. You, M. Ferrari, F. Salvatore, E. Tasciotti, Biomimetic carriers mimicking leukocyte plasma membrane to increase tumor vasculature permeability, Scientific Reports, 6 (2016).

[21] J.H. Li, Y.W. Ai, L.H. Wang, P.C. Bu, C.C. Sharkey, Q.H. Wu, B. Wun, S. Roy, X.L. Shen, M.R. King, Targeted drug delivery to circulating tumor cells via platelet membrane-functionalized particles, Biomaterials, 76 (2016) 52-65.

[22] Z. Chen, P.F. Zhao, Z.Y. Luo, M.B. Zheng, H. Tian, P. Gong, G.H. Gao, H. Pan, L.L. Liu, A.Q. Ma, H.D. Cui, Y.F. Ma, L.T. Cai, Cancer Cell Membrane-Biomimetic Nanoparticles for Homologous-Targeting Dual-Modal Imaging and Photothermal Therapy, Acs Nano, 10 (2016) 10049-10057.

[23] Y. Jiang, N. Krishnan, J.R. Zhou, S. Chekuri, X.L. Wei, A.V. Kroll, C.L. Yu, Y.O. Duan, W.W. Gao, R.N.H. Fang, L.F. Zhang, Engineered Cell-Membrane-Coated Nanoparticles Directly Present Tumor Antigens to Promote Anticancer Immunity, Advanced Materials, 32 (2020).

[24] W.W. Gao, C.M.J. Hu, R.H. Fang, B.T. Luk, J. Su, L.F. Zhang, Surface Functionalization of Gold Nanoparticles with Red Blood Cell Membranes, Advanced Materials, 25 (2013) 3549-3553.

[25] J.G. Piao, L.M. Wang, F. Gao, Y.Z. You, Y.J. Xiong, L.H. Yang, Erythrocyte Membrane Is an Alternative Coating to Polyethylene Glycol for Prolonging the Circulation Lifetime of Gold Nanocages for Photothermal Therapy, Acs Nano, 8 (2014) 10414-10425.

[26] K. Guo, S. Ren, H.F. Zhang, Y.Y. Cao, Y.T. Zhao, Y.J. Wang, W.L. Qiu, Y. Tian, L.A. Song, Z.Q. Wang, Biomimetic Gold Nanorods Modified with Erythrocyte Membranes for Imaging-Guided Photothermal/Gene Synergistic Therapy, Acs Applied Materials & Interfaces, 15 (2023) 25285-25299.

[27] M.J. Xuan, J.X. Shao, J. Zhao, Q. Li, L.R. Dai, J.B. Li, Magnetic Mesoporous Silica Nanoparticles Cloaked by Red Blood Cell Membranes: Applications in Cancer Therapy, Angewandte Chemie-International Edition, 57 (2018) 6049-6053.

[28] L. Rao, L.L. Bu, J.H. Xu, B. Cai, G.T. Yu, X.L. Yu, Z.B. He, Q.Q. Huang, A. Li, S.S. Guo, W.F. Zhang, W. Liu, Z.J. Sun, H. Wang, T.H. Wang, X.Z. Zhao, Red Blood Cell Membrane as a Biomimetic Nanocoating for Prolonged Circulation Time and Reduced Accelerated Blood Clearance, Small, 11 (2015) 6225-6236.

[29] X.Q. Ren, R. Zheng, X.L. Fang, X.F. Wang, X.Y. Zhang, W.L. Yang, X.Y. Sha, Red blood cell membrane camouflaged magnetic nanoclusters for imaging-guided photothermal therapy, Biomaterials, 92 (2016) 13-24.

[30] H. Min, J. Wang, Y.Q. Qi, Y.L. Zhang, X.X. Han, Y. Xu, J.C. Xu, Y. Li, L. Chen, K.M. Cheng, G.N. Liu, N. Yang, Y.Y. Li, G.J. Nie, Biomimetic Metal-Organic Framework Nanoparticles for Cooperative Combination of Antiangiogenesis and Photodynamic Therapy for Enhanced Efficacy, Advanced Materials, 31 (2019).

[31] L. Zhang, Z.Z. Wang, Y. Zhang, F.F. Cao, K. Dong, J.S. Ren, X.G. Qu, Erythrocyte Membrane Cloaked Metal-Organic Framework Nanoparticle as Biomimetic Nanoreactor for Starvation-Activated Colon Cancer Therapy, Acs Nano, 12 (2018) 10201-10211.

[32] M.Z. Alyami, S.K. Alsaiari, Y.Y. Li, S.S. Qutub, F.A. Aleisa, R. Sougrat, J.S. Merzaban, N.M. Khashab, Cell-Type-Specific CRISPR/Cas9 Delivery by Biomimetic Metal Organic Frameworks, Journal of the American Chemical Society, 142 (2020) 1715-1720.

[33] D. Nie, Z. Dai, J.L. Li, Y.W. Yang, Z.Y. Xi, J. Wang, W. Zhang, K. Qian, S.Y. Guo, C.L. Zhu, R. Wang, Y.M. Li, M.R. Yu, X.X. Zhang, X.H. Shi, Y. Gan, Cancer-Cell-Membrane-Coated Nanoparticles with a Yolk-Shell Structure Augment Cancer Chemotherapy, Nano Letters, 20 (2020) 936-946.

[34] Q. Sun, J.G. Wu, L.L. Jin, L.J. Hong, F. Wang, Z.W. Mao, M.J. Wu, Cancer cell membrane-coated gold nanorods for photothermal therapy and radiotherapy on oral squamous cancer, Journal of Materials Chemistry B, 8 (2020) 7253-7263.

[35] M.G. Jakaria, P. Sorkhdini, D.Q. Yang, Y. Zhou, S.A. Meenach, Lung cell membrane-coated nanoparticles capable of enhanced internalization and translocation in pulmonary epithelial cells, International Journal of Pharmaceutics, 613 (2022).

[36] C. Liu, W. Zhang, Y.K. Li, J.Q. Chang, F. Tian, F.H. Zhao, Y. Ma, J.S. Sun, Microfluidic Sonication To Assemble Exosome Membrane-Coated Nanoparticles for Immune Evasion-Mediated Targeting, Nano Letters, 19 (2019) 7836-7844.

[37] Q. Jiang, Y. Liu, R.R. Guo, X.X. Yao, S. Sung, Z.Q. Pang, W.L. Yang, Erythrocyte-cancer hybrid membrane-camouflaged melanin nanoparticles for enhancing photothermal therapy efficacy in tumors, Biomaterials, 192 (2019) 292-308.

[38] J.H. Park, Y. Jiang, J.R. Zhou, H. Gong, A. Mohapatra, J.Y. Heo, W.W. Gao, R.H. Fang, L.F. Zhang, Genetically engineered cell membrane-coated nanoparticles for targeted delivery of dexamethasone to inflamed lungs, Science Advances, 7 (2021).

[39] Q.Z. Zhang, D. Dehaini, Y. Zhang, J.L. Zhou, X.Y. Chen, L.F. Zhang, R.H. Fang, W.W. Gao, Neutrophil membrane-coated nanoparticles inhibit synovial inflammation and alleviate joint damage in inflammatory arthritis, Nature Nanotechnology, 13 (2018) 1182.

[40] Y. Gao, Y. Zhu, X.P. Xu, F.J. Wang, W.D. Shen, X. Leng, J.Y. Zhao, B.T. Liu, Y.Y. Wang, P.F. Liu, Surface PEGylated Cancer Cell Membrane-Coated Nanoparticles for Codelivery of Curcumin and Doxorubicin for the Treatment of Multidrug Resistant Esophageal Carcinoma, Frontiers in Cell and Developmental Biology, 9 (2021).

[41] M.S. Chen, M. Chen, J.T. He, Cancer cell membrane cloaking nanoparticles for targeted co-delivery of doxorubicin and PD-L1 siRNA, Artificial Cells Nanomedicine and Biotechnology, 47 (2019) 1635-1641.

[42] R.J.C. Bose, B.J. Kim, Y. Arai, I.B. Han, J.J. Moon, R. Paulmurugan, H. Park, S.H. Lee, Bioengineered stem cell membrane functionalized nanocarriers for therapeutic targeting of severe hindlimb ischemia, Biomaterials, 185 (2018) 360-370.

[43] N. Khosravi, E. Pishavar, B. Baradaran, F. Oroojalian, A. Mokhtarzadeh, Stem cell membrane, stem cell-derived exosomes and hybrid stem cell camouflaged nanoparticles: A promising biomimetic nanoplatforms for cancer theranostics, Journal of Controlled Release, 348 (2022) 706-722.

[44] X.P. Mu, J. Li, S.H. Yan, H.M. Zhang, W.J. Zhang, F.Q. Zhang, J.L. Jiang, siRNA Delivery with Stem Cell Membrane-Coated Magnetic Nanoparticles for Imaging-Guided Photothermal Therapy and Gene Therapy, Acs Biomaterials Science & Engineering, 4 (2018) 3895-3905.

[45] S.Q. Wu, C.X. Yang, X.P. Yan, A Dual-Functional Persistently Luminescent Nanocomposite Enables Engineering of Mesenchymal Stem Cells for Homing and Gene Therapy of Glioblastoma, Advanced Functional Materials, 27 (2017).

[46] L. Kaneti, T. Bronshtein, N.M. Dayan, I. Kovregina, N.L. Khait, Y. Lupu-Haber, M. Fliman, B.W. Schoen, G. Kaneti, M. Machluf, Nanoghosts as a Novel Natural Nonviral Gene Delivery Platform Safely Targeting Multiple Cancers, Nano Letters, 16 (2016) 1574-1582.

[47] G. Go, J. Lee, D.S. Choi, S.S. Kim, Y.S. Gho, Extracellular Vesicle-Mimetic Ghost Nanovesicles for Delivering Anti-Inflammatory Drugs to Mitigate Gram-Negative Bacterial Outer Membrane Vesicle-Induced Systemic Inflammatory Response Syndrome, Advanced Healthcare Materials, 8 (2019).

[48] A. Pitchaimani, T.D.T. Nguyen, S. Aryal, Natural killer cell membrane infused biomimetic liposomes for targeted tumor therapy, Biomaterials, 160 (2018) 124-137.

[49] K.L. Zhang, Y.J. Wang, J. Sun, J. Zhou, C. Xing, G.M. Huang, J. Li, H.H. Yang, Artificial chimeric exosomes for anti-phagocytosis and targeted cancer therapy, Chemical Science, 10 (2019) 1555-1561.

[50] W. Zhang, C.N. Gong, Z.Q. Chen, M. Li, Y.P. Li, J. Gao, Tumor microenvironment-activated cancer cell membrane-liposome hybrid nanoparticle-mediated synergistic metabolic therapy and chemotherapy for non-small cell lung cancer, Journal of Nanobiotechnology, 19 (2021).

[51] P. Mirabelli, L. Coppola, M. Salvatore, Cancer Cell Lines Are Useful Model Systems for Medical Research, Cancers, 11 (2019).

[52] J.N. Weinstein, Drug Discovery Cell lines battle cancer, Nature, 483 (2012) 544-545.

[53] R. Würths, A. Pattarozzi, F. Barbieri, T. Florio, Primary Cultures from Human GH-secreting or Clinically Non-functioning Pituitary Adenomas, Bio-Protocol, 8 (2018).

[54] S.G.M. Ong, M. Chitneni, K.S. Lee, L.C. Ming, K.H. Yuen, Evaluation of Extrusion Technique for Nanosizing Liposomes, Pharmaceutics, 8 (2016).

[55] Z.L. Chai, D.N. Ran, L.W. Lu, C.Y. Zhan, H.T. Ruan, X.F. Hu, C. Xie, K. Jiang, J.Y. Li, J.F. Zhou, J. Wang, Y.Y. Zhang, R.H. Fang, L.F. Zhang, W.Y. Lu, Ligand-Modified Cell Membrane Enables the Targeted Delivery of Drug Nanocrystals to Glioma, Acs Nano, 13 (2019) 5591-5601.

[56] W.X. Lv, Z.W. Han, Y.K. Li, Y.J. Huang, J.S. Sun, X.Q. Lu, C. Liu, Exosome-Coated Zeolitic Imidazolate Framework Nanoparticles for Intracellular Detection of ATP, Chinese Journal of Chemistry, 39 (2021) 2107-2112.

[57] F.P. Yang, M.H. Cabe, S.D. Ogle, V. Sanchez, K.A. Langert, Optimization of critical parameters for coating of polymeric nanoparticles with plasma membrane vesicles by sonication, Scientific Reports, 11 (2021).

[58] J. Gehl, Electroporation: theory and methods, perspectives for drug delivery, gene therapy and research, Acta Physiologica Scandinavica, 177 (2003) 437-447.

[59] J.L. Hood, M.J. Scott, S.A. Wickline, Maximizing exosome colloidal stability following electroporation, Analytical Biochemistry, 448 (2014) 41-49.

[60] M.J. Haney, N.L. Klyachko, Y.L. Zhaoa, R. Gupta, E.G. Plotnikova, Z.J. He, T. Patel, A. Piroyan, M. Sokolsky, A.V. Kabanov, E.V. Batrakova, Exosomes as drug delivery vehicles for Parkinson's disease therapy, Journal of Controlled Release, 207 (2015) 18-30.

[61] S. Joshi, M.T. Hussain, C.B. Roces, G. Anderluzzi, E. Kastner, S. Salmaso, D.J. Kirby, Y. Perrie, Microfluidics based manufacture of liposomes simultaneously entrapping hydrophilic and lipophilic drugs, International Journal of Pharmaceutics, 514 (2016) 160-168.

[62] D. Fondaj, I. Arduino, A.A. Lopedota, N. Denora, R.M. Iacobazzi, Exploring the Microfluidic Production of Biomimetic Hybrid Nanoparticles and Their Pharmaceutical Applications, Pharmaceutics, 15 (2023).

[63] R. Molinaro, M. Evangelopoulos, J.R. Hoffman, C. Corbo, F. Taraballi, J.O. Martinez, K.A. Hartman, D. Cosco, G. Costa, I. Romeo, M. Sherman, D. Paolino, S. Alcaro, E. Tasciotti, Design and Development of Biomimetic Nanovesicles Using a Microfluidic Approach, Advanced Materials, 30 (2018).

[64] A. Agha, W. Waheed, I. Stiharu, V. Nerguizian, G. Destgeer, E. Abu-Nada, A. Alazzam, A review on microfluidic-assisted nanoparticle synthesis, and their applications using multiscale simulation methods, Discover Nano, 18 (2023).

[65] Y. Liu, G.Z. Yang, Y. Hui, S. Ranaweera, C.X. Zhao, Microfluidic Nanoparticles for Drug Delivery, Small, 18 (2022).

[66] N. Forbes, M.T. Hussain, M.L. Briuglia, D.P. Edwards, J.H. ter Horst, N. Szita, Y. Perrie, Rapid and scale-independent microfluidic manufacture of liposomes entrapping protein incorporating in-line purification and at-line size monitoring, International Journal of Pharmaceutics, 556 (2019) 68-81.

[67] A. Jahn, W.N. Vreeland, M. Gaitan, L.E. Locascio, Controlled vesicle self-assembly in microfluidic channels with hydrodynamic focusing, Journal of the American Chemical Society, 126 (2004) 2674-2675.

[68] J. Marschewski, S. Jung, P. Ruch, N. Prasad, S. Mazzotti, B. Michel, D. Poulikakos, Mixing with herringbone-inspired microstructures: overcoming the diffusion limit in co-laminar microfluidic devices, Lab on a Chip, 15 (2015) 1923-1933.

[69] J.J. Wang, J.A. Wang, L.F. Feng, T. Lin, Fluid mixing in droplet-based microfluidics with a serpentine microchannel, Rsc Advances, 5 (2015) 104138-104144.

[70] P.M. Valencia, P.A. Basto, L.F. Zhang, M. Rhee, R. Langer, O.C. Farokhzad, R. Karnik, Single-Step Assembly of Homogenous Lipid - Polymeric and Lipid - Quantum Dot Nanoparticles Enabled by Microfluidic Rapid Mixing, Acs Nano, 4 (2010) 1671-1679.

[71] R. Othman, G.T. Vladisavljevic, H.C.H. Bandulasena, Z.K. Nagy, Production of polymeric nanoparticles by micromixing in a co-flow microfluidic glass capillary device, Chemical Engineering Journal, 280 (2015) 316-329.

[72] P. Erfle, J. Riewe, H. Bunjes, A. Dietzel, Stabilized Production of Lipid Nanoparticles of Tunable Size in Taylor Flow Glass Devices with High-Surface-Quality 3D Microchannels, Micromachines, 10 (2019).

[73] A. Fornell, M. Ohlin, F. Garofalo, J. Nilsson, M. Tenje, An intra-droplet particle switch for droplet microfluidics using bulk acoustic waves, Biomicrofluidics, 11 (2017).

[74] M. Maeki, T. Saito, Y. Sato, T. Yasui, N. Kaji, A. Ishida, H. Tani, Y. Baba, H. Harashima, M. Tokeshi, A strategy for synthesis of lipid nanoparticles using microfluidic devices with a mixer structure, Rsc Advances, 5 (2015) 46181-46185.

[75] J. Riewe, P. Erfle, S. Melzig, A. Kwade, A. Dietzel, H. Bunjes, Antisolvent precipitation of lipid nanoparticles in microfluidic systems - A comparative study, International Journal of Pharmaceutics, 579 (2020).

[76] N. Dimov, E. Kastner, M. Hussain, Y. Perrie, N. Szita, Formation and purification of tailored liposomes for drug delivery using a module-based micro continuous-flow system, Scientific Reports, 7 (2017).

[77] Y. Morikawa, T. Tagami, A. Hoshikawa, T. Ozeki, The Use of an Efficient Microfluidic Mixing System for Generating Stabilized Polymeric Nanoparticles for Controlled Drug Release, Biological & Pharmaceutical Bulletin, 41 (2018) 899-907.

[78] K. Osouli-Bostanabad, S. Puliga, D.R. Serrano, A. Bucchi, G. Halbert, A. Lalatsa, Microfluidic Manufacture of Lipid-Based Nanomedicines, Pharmaceutics, 14 (2022).

[79] T.A. Balbino, A.R. Azzoni, L.G. de la Torre, Microfluidic devices for continuous production of pDNA/cationic liposome complexes for gene delivery and vaccine therapy, Colloids and Surfaces B-Biointerfaces, 111 (2013) 203-210.

[80] A. Aranguren, C.E. Torres, C. Muñoz-Camargo, J.F. Osma, J.C. Cruz, Synthesis of Nanoscale Liposomes via Low-Cost Microfluidic Systems, Micromachines, 11 (2020).

[81] G. Destgeer, S. Im, B.H. Ha, J.H. Jung, M.A. Ansari, H.J. Sung, Adjustable, rapidly switching microfluidic gradient generation using focused travelling surface acoustic waves, Applied Physics Letters, 104 (2014).

[82] H.Z. Sun, Y.K. Ren, Y. Tao, T.Y. Jiang, H.Y. Jiang, Three-Fluid Sequential Micromixing-Assisted Nanoparticle Synthesis Utilizing Alternating Current Electrothermal Flow, Industrial & Engineering Chemistry Research, 59 (2020) 12514-12524.

[83] P. Modarres, M. Tabrinan, Electrohydrodynamic-Driven Micromixing for the Synthesis of Highly Monodisperse Nanoscale Liposomes, Acs Applied Nano Materials, 3 (2020) 4000-4013.

[84] X.M. Huang, R. Caddell, B. Yu, S.L. Xu, B. Theobald, L.J. Lee, R.J. Lee, Ultrasound-enhanced Microfluidic Synthesis of Liposomes, Anticancer Research, 30 (2010) 463-466.

[85] R.R. López, I. Ocampo, P.G.F. de Rubinat, L.M. Sánchez, A. Alazzam, T. Tsering, K.F. Bergeron, S. Camacho-Léon, J.V. Burnier, C. Mounier, I. Stiharu, V. Nerguizian, Parametric Study of the Factors Influencing Liposome Physicochemical Characteristics in a Periodic Disturbance Mixer, Langmuir, 37 (2021) 8544-8556.

[86] V.T. Thu, A.N. Mai, L. Tam, H.V. Trung, P.T. Thu, B.Q. Tien, N.T. Thuat, T.D. Lam, Fabrication of PDMS-Based Microfluidic Devices: Application for Synthesis of Magnetic Nanoparticles, Journal of Electronic Materials, 45 (2016) 2576-2581.

[87] M.J. Kennedy, H.D. Ladouceur, T. Moeller, D. Kirui, C.A. Batt, Analysis of a laminar-flow diffusional mixer for directed self-assembly of liposomes, Biomicrofluidics, 6 (2012).

[88] J. Cao, P. Cheng, F.J. Hong, Applications of electrohydrodynamics and Joule heating effects in microfluidic chips: A review, Science in China Series E-Technological Sciences, 52 (2009) 3477-3490.

[89] G. Lou, G. Anderluzzi, S. Woods, C.W. Roberts, Y. Perrie, A novel microfluidic-based approach to formulate size-tuneable large unilamellar cationic liposomes: Formulation, cellular uptake and biodistribution investigations, European Journal of Pharmaceutics and Biopharmaceutics, 143 (2019) 51-60.

[90] S. Amrani, M. Tabrizian, Characterization of Nanoscale Loaded Liposomes Produced by 2D Hydrodynamic Flow Focusing, Acs Biomaterials Science & Engineering, 4 (2018) 502-513.

[91] R.R. Hood, D.L. DeVoe, J. Atencia, W.N. Vreeland, D.M. Omiatek, A facile route to the synthesis of monodisperse nanoscale liposomes using 3D microfluidic hydrodynamic focusing in a concentric capillary array, Lab on a Chip, 14 (2014) 2403-2409.

[92] R. Zoqlam, C.J. Morris, M. Akbar, A.M. Alkilany, S.I. Hamdallah, P. Belton, S. Qi, Evaluation of the Benefits of Microfluidic-Assisted Preparation of Polymeric Nanoparticles for DNA Delivery, Materials Science & Engineering C-Materials for Biological Applications, 127 (2021).

[93] A. Ozcelik, Z. Aslan, A simple acoustofluidic device for on-chip fabrication of PLGA nanoparticles, Biomicrofluidics, 16 (2022).

[94] E. Lallana, R. Donno, D. Magrì, K. Barker, Z. Nazir, K. Treacher, M.J. Lawrence, M. Ashford, N. Tirelli, Microfluidic-assisted nanoprecipitation of (PEGylated) poly (D,L-lactic acid-co-

caprolactone): Effect of macromolecular and microfluidic parameters on particle size and paclitaxel encapsulation, International Journal of Pharmaceutics, 548 (2018) 530-539.

[95] J.S. Sun, Y.L. Xianyu, M.M. Li, W.W. Liu, L. Zhang, D.B. Liu, C. Liu, G.Q. Hu, X.Y. Jiang, A microfluidic origami chip for synthesis of functionalized polymeric nanoparticles, Nanoscale, 5 (2013) 5262-5265.

[96] C.C.L. Cheung, W.T. Al-Jamal, Sterically stabilized liposomes production using staggered herringbone micromixer: Effect of lipid composition and PEG-lipid content, International Journal of Pharmaceutics, 566 (2019) 687-696.

[97] M.G. Toudeshkchouei, P. Zahedi, A. Shavandi, Microfluidic-Assisted Preparation of 5-Fluorouracil-Loaded PLGA Nanoparticles as a Potential System for Colorectal Cancer Therapy, Materials, 13 (2020).

[98] L. Zhang, Q.H. Chen, Y. Ma, J.S. Sun, Microfluidic Methods for Fabrication and Engineering of Nanoparticle Drug Delivery Systems, Acs Applied Bio Materials, 3 (2020) 107-120.

[99] B.B. Mendes, J. Conniot, A. Avital, D.B. Yao, X.Y. Jiang, X. Zhou, N. Sharf-Pauker, Y.L. Xiao, O. Adir, H.J. Liang, J.J. Shi, A. Schroeder, J. Conde, Nanodelivery of nucleic acids, Nature Reviews Methods Primers, 2 (2022).

[100] A.K. Iyer, Z.F. Duan, M.M. Amiji, Nanodelivery Systems for Nucleic Acid Therapeutics in Drug Resistant Tumors, Molecular Pharmaceutics, 11 (2014) 2511-2526.

[101] A. Khurana, P. Allawadhi, I. Khurana, S. Allwadhi, R. Weiskirchen, A.K. Banothu, D. Chhabra, K. Joshi, K.K. Bharani, Role of nanotechnology behind the success of mRNA vaccines for COVID-19, Nano Today, 38 (2021).

[102] N. Chaudhary, D. Weissman, K.A. Whitehead, mRNA vaccines for infectious diseases: principles, delivery and clinical translation, Nature Reviews Drug Discovery, 20 (2021) 817-838.

[103] M.H. Chan, Z.X. Chang, C.Y.F. Huang, L.J. Lee, R.S. Liu, M. Hsiao, Integrated therapy platform of exosomal system: hybrid inorganic/organic nanoparticles with exosomes for cancer treatment, Nanoscale Horizons, 7 (2022) 352-367.

[104] B.M. Razzo, N. Ludwig, C.S. Hong, P. Sharma, K.P. Fabian, R.J. Fecek, W.J. Storkus, T.L. Whiteside, Tumor-derived exosomes promote carcinogenesis of murine oral squamous cell carcinoma, Carcinogenesis, 41 (2020) 625-633.

[105] WHO, International Statistical Classification of Diseases and Related Health Problems, 11th revision, in, Geneva, 2022.

[106] ENCR, European Network of Cancer Registries, in, 2023.

[107] M. Wrensch, Y. Minn, T. Chew, M. Bondy, M.S. Berger, Epidemiology of primary brain tumors: Current concepts and review of the literature, Neuro-Oncology, 4 (2002) 278-299.

[108] S.H. Torp, O. Solheim, A.J. Skjulsvik, The WHO 2021 Classification of Central Nervous System tumours: a practical update on what neurosurgeons need to know-a minireview, Acta Neurochirurgica, 164 (2022) 2453-2464.

[109] D. Figarella-Branger, R. Appay, A. Metais, A. Tauziède-Espariat, C. Colin, A. Rousseau, P. Varlet, The 2021 WHO classification of tumours of the central nervous system, Annales De Pathologie, 42 (2022) 367-382.

[110] A.A. Brandes, A. Tosoni, E. Franceschi, M. Reni, G. Gatta, C. Vecht, Glioblastoma in adults, Critical Reviews in Oncology Hematology, 67 (2008) 139-152.

[111] Y.H. Zhao, Z.F. Wang, C.J. Cao, H. Weng, C.S. Xu, K. Li, J.L. Li, J. Lan, X.T. Zeng, Z.Q. Li, The Clinical Significance of O⁶-Methylguanine-DNA Methyltransferase Promoter Methylation Status in Adult Patients With Glioblastoma: A Meta-analysis, Frontiers in Neurology, 9 (2018).

[112] V. Gilard, A. Tebani, I. Dabaj, A. Laquerrière, M. Fontanilles, S. Derrey, S. Marret, S. Bekri, Diagnosis and Management of Glioblastoma: A Comprehensive Perspective, Journal of Personalized Medicine, 11 (2021).

[113] G. Shukla, G.S. Alexander, S. Bakas, R. Nikam, K. Talekar, J.D. Palmer, W.Y. Shi, Advanced magnetic resonance imaging in glioblastoma: a review, Chinese Clinical Oncology, 6 (2017).

[114] V. Gouazo-Andersson, E.C.J. Moyal, New Avenues in Radiotherapy of Glioblastoma: from Bench to Bedside, Current Treatment Options in Neurology, 22 (2020).

[115] E. Carrasco-Garcia, N. Sampron, P. Aldaz, O. Arrizabalaga, J. Villanua, C. Barrena, I. Ruiz, M. Arrazola, C. Lawrie, A. Matheu, Therapeutic Strategies Targeting Glioblastoma Stem Cells, Recent Patents on Anti-Cancer Drug Discovery, 8 (2013) 216-227.

[116] A.M. Hughes, N.N.R. Hu, Optimizing Boron Neutron Capture Therapy (BNCT) to Treat Cancer: An Updated Review on the Latest Developments on Boron Compounds and Strategies, Cancers, 15 (2023).

[117] D.S. Seneviratne, O. Saifi, Y. Mackeyev, T. Malouff, S. Krishnan, Next-Generation Boron Drugs and Rational Translational Studies Driving the Revival of BNCT, Cells, 12 (2023).

[118] G. Ailuno, A. Balboni, G. Caviglioli, F. Lai, F. Barbieri, I. Dellacasagrande, T. Florio, S. Baldassari, Boron Vehiculating Nanosystems for Neutron Capture Therapy in Cancer Treatment, Cells, 11 (2022).

[119] T.D. Malouff, D.S. Seneviratne, D.K. Ebner, W.C. Stross, M.R. Waddle, D.M. Trifiletti, S. Krishnan, Boron Neutron Capture Therapy: A Review of Clinical Applications, Frontiers in Oncology, 11 (2021).

[120] S.I. Miyatake, S. Kawabata, Y. Kajimoto, A.H. Aoki, K. Yokoyama, M. Yamada, T. Kuroiwa, M. Tsuji, Y. Imahori, M. Kirihata, Y. Sakurai, S.I. Masunaga, K. Nagata, A. Maruhashi, K. Ono, Modified boron neutron capture therapy for malignant gliomas performed using epithermal neutron and two boron compounds with different accumulation mechanisms: an efficacy study based on findings on neuroimages, Journal of Neurosurgery, 103 (2005) 1000-1009.

[121] J. Capala, B.H. Stenstam, K.S. Sköld, P.M. af Rosenschöld, V. Giusti, C. Persson, E. Wallin, A. Brun, L. Franzen, J.O. Carlsson, L. Salford, C. Ceberg, B. Persson, L. Pellettieri, R. Henriksson, Boron neutron capture therapy for glioblastoma multiforme:: clinical studies in Sweden, Journal of Neuro-Oncology, 62 (2003) 135-144.

[122] S.I. Miyatake, Y. Tamura, S. Kawabata, K. Iida, T. Kuroiwa, K. Ono, Boron neutron capture therapy for malignant tumors related to meningiomas, Neurosurgery, 61 (2007) 82-90.

[123] A. Wittig, L. Collette, K. Appelman, S. Bührmann, M.C. Jäckel, K.H. Jöckel, K.W. Schmid, U. Ortmann, R. Moss, W.A.G. Sauerwein, EORTC trial 11001: distribution of two 10B-compounds in patients with squamous cell carcinoma of head and neck, a translational research/phase 1 trial, Journal of Cellular and Molecular Medicine, 13 (2009) 1653-1665.

[124] L. Kankaanranta, T. Seppälä, H. Koivunoro, K. Saarilahti, T. Atula, J. Collan, E. Salli, M. Kortesniemi, J. Uusi-Simola, A. Mäkitle, M. Seppänen, H. Minn, P. Kotiluoto, I. Auterinen, S. Savolainen, M. Kouri, H. Joensuu, Boron neutron capture therapy in the treatment of locally recurred head and neck cancer, International Journal of Radiation Oncology Biology Physics, 69 (2007) 475-482.

[125] P.R. Menéndez, B.M.C. Roth, M.D. Pereira, M.R. Casal, S.J. González, D.B. Feld, G.A.S. Cruz, J. Kessler, J. Longhino, H. Blaumann, R.J. Rebagliati, O.A.C. Larrieu, C. Fernández, S.I. Nievas, S.J. Liberman, BNCT for skin melanoma in extremities: Updated Argentine clinical results, Applied Radiation and Isotopes, 67 (2009) S50-S53.

[126] H. Yanagie, S. Higashi, K. Seguchi, I. Ikushima, M. Fujihara, Y. Nonaka, K. Oyama, S. Maruyama, R. Hatae, M. Suzuki, S. Masunaga, T. Kinashi, Y. Sakurai, H. Tanaka, N. Kondo, M. Narabayashi, T. Kajiyama, A. Maruhashi, K. Ono, J. Nakajima, M. Ono, H. Takahashi, M. Eriguchi, Pilot clinical study of boron neutron capture therapy for recurrent hepatic cancer involving the intra-arterial injection of a 10BSH-containing WOW emulsion, Applied Radiation and Isotopes, 88 (2014) 32-37.

[127] M. Nuez-Martínez, L. Pedrosa, I. Martinez-Rovira, I. Yousef, D. Diao, F. Teixidor, E. Stanzani, F. Martínez-Soler, A. Tortosa, A. Sierra, J.J. Gonzalez, C. Viñas, Synchrotron-Based Fourier-Transform Infrared Micro-Spectroscopy (SR-FTIRM) Fingerprint of the Small Anionic Molecule Cobaltabis(dicarbollide) Uptake in Glioma Stem Cells, International Journal of Molecular Sciences, 22 (2021).

[128] J. McLaurin, G.C. Trudel, I.T. Shaw, J.P. Antel, N.R. Cashman, A Human Glial Hybrid Cell-Line Differentially Expressing Genes Subserving Oligodendrocyte And Astrocyte Phenotype, Journal of Neurobiology, 26 (1995) 283-293.

[129] J.M. Suski, M. Lebiedzinska, A. Wojtala, J. Duszynski, C. Giorgi, P. Pinton, M.R. Wieckowski, Isolation of plasma membrane-associated membranes from rat liver, Nature Protocols, 9 (2014) 312-322.

[130] T. Akagi, T. Ichiki, Cell electrophoresis on a chip: what can we know from the changes in electrophoretic mobility?, Analytical and Bioanalytical Chemistry, 391 (2008) 2433-2441.

[131] V. Filipe, A. Hawe, W. Jiskoot, Critical Evaluation of Nanoparticle Tracking Analysis (NTA) by NanoSight for the Measurement of Nanoparticles and Protein Aggregates, Pharmaceutical Research, 27 (2010) 796-810.

[132] E.H. Koritzinsky, J.M. Street, R.A. Star, P.S.T. Yuen, Quantification of Exosomes, Journal of Cellular Physiology, 232 (2017) 1587-1590.

[133] N. Comfort, K.H. Cai, T.R. Bloomquist, M.D. Strait, A.W. Ferrante, A.A. Baccarelli, Nanoparticle Tracking Analysis for the Quantification and Size Determination of Extracellular Vesicles, Jove-Journal of Visualized Experiments, (2021).

[134] M. Aguilera-Rojas, B. Badewien-Rentzsch, J. Plendl, B. Kohn, R. Einspanier, Exploration of serum- and cell culture-derived exosomes from dogs, Bmc Veterinary Research, 14 (2018).

[135] J.Y. Kim, W.K. Rhim, Y.I. Yoo, D. Kim, K.W. Ko, Y. Heo, C.G. Park, D.K. Han, Defined MSC exosome with high yield and purity to improve regenerative activity, Journal of Tissue Engineering, 12 (2021).

[136] A. Meister, A. Blume, (Cryo)Transmission Electron Microscopy of Phospholipid Model Membranes Interacting with Amphiphilic and Polyphilic Molecules, Polymers, 9 (2017).

[137] L.E. Franken, E.J. Boekema, M.C.A. Stuart, Transmission Electron Microscopy as a Tool for the Characterization of Soft Materials: Application and Interpretation, Advanced Science, 4 (2017).

[138] P. Moraille, Z. Abdali, M. Ramkaran, D. Polcari, G.S. Patience, N.M.D. Courchesne, A. Badia, Experimental methods in chemical engineering: Atomic force microscopy - AFM, Canadian Journal of Chemical Engineering, 100 (2022) 2778-2806.

[139] M. LeClaire, J. Gimzewski, S. Sharma, A review of the biomechanical properties of single extracellular vesicles, in, Nano Select, 2021, pp. 1-15.

[140] S.A. Gazze, S.J. Thomas, J. Garcia-Parra, D.W. James, P. Rees, V. Marsh-Durban, R. Corteling, D. Gonzalez, R.S. Conlan, L.W. Francis, High content, quantitative AFM analysis of the scalable biomechanical properties of extracellular vesicles, Nanoscale, 13 (2021) 6129-6141.

[141] V.Y. Bairamukov, A.S. Bukatin, R.A. Kamyshinsky, V.S. Burdakov, E.B. Pichkur, T.A. Shtam, M.N. Starodubtseva, Nanomechanical characterization of exosomes and concomitant nanoparticles from blood plasma by PeakForce AFM in liquid, Biochimica Et Biophysica Acta-General Subjects, 1866 (2022).

[142] J.J. Lai, Z.L. Chau, S.Y. Chen, J.J. Hill, K.V. Korpany, N.W. Liang, L.H. Lin, Y.H. Lin, J.K. Liu, Y.C. Liu, R. Lunde, W.T. Shen, Exosome Processing and Characterization Approaches for Research and Technology Development, Advanced Science, 9 (2022).

[143] W. Rawicz, K.C. Olbrich, T. McIntosh, D. Needham, E. Evans, Effect of chain length and unsaturation on elasticity of lipid bilayers, Biophysical Journal, 79 (2000) 328-339.

[144] R. Dimova, Recent developments in the field of bending rigidity measurements on membranes, Advances in Colloid and Interface Science, 208 (2014) 225-234.

[145] R. Sorkin, R. Huisjes, F. Boskovic, D. Vorselen, S. Pignatelli, Y. Ofir-Birin, J.K.F. Leal, J. Schiller, D. Mullick, W.H. Roos, G. Bosman, N. Regev-Rudzki, R.M. Schiffelers, G.J.L. Wuite, Nanomechanics of Extracellular Vesicles Reveals Vesiculation Pathways, Small, 14 (2018).

[146] C. Théry, M. Ostrowski, E. Segura, Membrane vesicles as conveyors of immune responses, Nature Reviews Immunology, 9 (2009) 581-593.

[147] H. Bouvrais, Bending Rigidities Of Lipid Bilayers: Their Determination And Main Inputs In Biophysical Studies, Advances in Planar Lipid Bilayers and Liposomes, Vol 15, 15 (2012) 1-75.

[148] V. Vitkova, P. Méléard, T. Pott, I. Bivas, Alamethicin influence on the membrane bending elasticity, European Biophysics Journal with Biophysics Letters, 35 (2006) 281-286.

[149] W. Hackl, U. Seifert, E. Sackmann, Effects of fully and partially solubilized amphiphiles on bilayer bending stiffness and temperature dependence of the effective tension of giant vesicles, Journal De Physique Ii, 7 (1997) 1141-1157.

[150] S. Tristram-Nagle, J.F. Nagle, HIV-1 fusion peptide decreases bending energy and promotes curved fusion intermediates, Biophysical Journal, 93 (2007) 2048-2055.

[151] V. Nikolov, R. Lipowsky, R. Dimova, Behavior of giant vesicles with anchored DNA molecules, Biophysical Journal, 92 (2007) 4356-4368.

[152] C. Hiergeist, R. Lipowsky, Elastic properties of polymer-decorated membranes, Journal De Physique Ii, 6 (1996) 1465-1481.

[153] P. Ratanabanangkoon, M. Gropper, R. Merkel, E. Sackmann, A.P. Gast, Mechanics of streptavidin-coated giant lipid bilayer vesicles: A micropipet study, Langmuir, 19 (2003) 1054-1062.

[154] X. Yi, X.H. Shi, H.J. Gao, Cellular Uptake of Elastic Nanoparticles, Physical Review Letters, 107 (2011).

[155] T.T. Yue, X.R. Zhang, Molecular modeling of the pathways of vesicle-membrane interaction, Soft Matter, 9 (2013) 559-569.

[156] X. Banquy, F. Suarez, A. Argaw, J.M. Rabanel, P. Grutter, J.F. Bouchard, P. Hildgen, S. Giasson, Effect of mechanical properties of hydrogel nanoparticles on macrophage cell uptake, Soft Matter, 5 (2009) 3984-3991.

[157] K.A. Beningo, Y.L. Wang, Fc-receptor-mediated phagocytosis is regulated by mechanical properties of the target, Journal of Cell Science, 115 (2002) 849-856.

[158] A.C. Anselmo, M.W. Zhang, S. Kumar, D.R. Vogus, S. Menegatti, M.E. Helgeson, S. Mitragotri, Elasticity of Nanopartides Influences Their Blood Circulation, Phagocytosis, Endocytosis, and Targeting, Acs Nano, 9 (2015) 3169-3177.

[159] N. Kol, Y. Shi, M. Tsvitov, D. Barlam, R.Z. Shneck, M.S. Kay, I. Rousso, A stiffness switch in human immunodeficiency virus, Biophysical Journal, 92 (2007) 1777-1783.

[160] M.C. Sharma, Annexin A2 (ANX A2): An emerging biomarker and potential therapeutic target for aggressive cancers, International Journal of Cancer, 144 (2019) 2074-2081.

[161] M. Rose, T. Cardon, S. Aboulouard, N. Hajjaji, F. Kobeissy, M. Duhamel, I. Fournier, M. Salzet, Surfaceome Proteomic of Glioblastoma Revealed Potential Targets for Immunotherapy, Frontiers in Immunology, 12 (2021).

[162] D.M. Mallawaaratchy, M.E. Buckland, K.L. McDonald, C.C.Y. Li, L. Ly, E.K. Sykes, R.I. Christopherson, K.L. Kaufman, Membrane Proteome Analysis of Glioblastoma Cell Invasion, Journal of Neuropathology and Experimental Neurology, 74 (2015) 425-441.

[163] N. Hedhli, D.J. Falcone, B.H. Huang, G. Cesarman-Maus, R. Kraemer, H.Y. Zhai, S.E. Tsirka, L. Santambrogio, K.A. Hajjar, The Annexin A2/S100A10 System in Health and Disease: Emerging Paradigms, Journal of Biomedicine and Biotechnology, (2012).

[164] F. Maule, S. Bresolin, E. Rampazzo, D. Boso, A. Della Puppa, G. Esposito, E. Porcù, S. Mitola, G. Lombardi, B. Accordi, M. Tumino, G. Basso, L. Persano, Annexin 2A sustains glioblastoma cell dissemination and proliferation, Oncotarget, 7 (2016) 54632-54649.

[165] Y. Matsumoto, T. Ichikawa, K. Kurozumi, Y. Otani, A. Fujimura, K. Fujii, Y. Tomita, Y. Hattori, A. Uneda, N. Tsuboi, K. Kaneda, K. Makino, I. Date, Annexin A2-STAT3-Oncostatin M receptor axis

drives phenotypic and mesenchymal changes in glioblastoma, Acta Neuropathologica Communications, 8 (2020).

[166] H.Y. Zhai, S. Acharya, I. Gravanis, S. Mehmood, R.J. Seidman, K.R. Shroyer, K.A. Hajjar, S.E. Tsirka, Annexin A2 Promotes Glioma Cell Invasion and Tumor Progression, Journal of Neuroscience, 31 (2011) 14346-14360.

[167] S. Han, Y. Lee, M. Lee, Biomimetic cell membrane-coated DNA nanoparticles for gene delivery to glioblastoma, Journal of Controlled Release, 338 (2021) 22-32.

[168] C.M. Van RiJ, A. Sinijewel, A.C. Van Loenen, W.A.G. Sauerwein, A. Wittig, O. Kriz, A.J. Wilhelm, Stability of 10B-L-boronophenylalanine–fructose injection, in, American Journal of health-sytem pharmacy, 2005, pp. 2608-2610.

[169] E. Lubomirsky, A. Khodabandeh, J. Preis, M. Susewind, T. Hofe, E.F. Hilder, R.D. Arrua, Polymeric stationary phases for size exclusion chromatography: A review, Analytica Chimica Acta, 1151 (2021).

[170] F. Pavanetto, P. Perugini, I. Genta, C. Minoia, A. Ronchi, U. Prati, L. Roveda, R. Nano, Boron-loaded liposomes in the treatment of hepatic metastases: Preliminary investigation by autoradiography analysis, Drug Delivery, 7 (2000) 97-103.

[171] C. Douvris, T. Vaughan, D. Bussan, G. Bartzas, R. Thomas, How ICP-OES changed the face of trace element analysis: Review of the global application landscape, Science of the Total Environment, 905 (2023).

[172] M.J. Luderer, B. Muz, K. Alhallak, J. Sun, K. Wasden, N. Guenthner, P. de la Puente, C. Federico, A.K. Azab, Thermal Sensitive Liposomes Improve Delivery of Boronated Agents for Boron Neutron Capture Therapy, Pharmaceutical Research, 36 (2019).

[173] I. Mármol, C. Sánchez-De-Diego, A.P. Dieste, E. Cerrada, M.J.R. Yoldi, Colorectal Carcinoma: A General Overview and Future Perspectives in Colorectal Cancer, International Journal of Molecular Sciences, 18 (2017).

[174] H. Brenner, M. Kloor, C.P. Pox, Colorectal cancer, Lancet, 383 (2014) 1490-1502.

[175] T.R. Levin, D.A. Corley, C.D. Jensen, J.E. Schottinger, V.P. Quinn, A.G. Zauber, J.K. Lee, W.K. Zhao, N. Udaltsova, N.R. Ghai, A.T. Lee, C.P. Quesenberry, B.H. Fireman, C.A. Doubeni, Effects of Organized Colorectal Cancer Screening on Cancer Incidence and Mortality in a Large Community-Based Population, Gastroenterology, 155 (2018) 1383.

[176] S. Gupta, D.A. Sussman, C.A. Doubeni, D.S. Anderson, L. Day, A.R. Deshpande, B.J. Elmunzer, A.O. Laiyemo, J. Mendez, M. Somsouk, J. Allison, T. Bhuket, Z. Geng, B.B. Green, S.H. Itzkowitz, M.E. Martinez, Challenges and Possible Solutions to Colorectal Cancer Screening for the Underserved, Jnci-Journal of the National Cancer Institute, 106 (2014).

[177] S.C.H. Chan, J.Q. Liang, Advances in tests for colorectal cancer screening and diagnosis, Expert Review of Molecular Diagnostics, 22 (2022) 449-460.

[178] T. Vu, P.K. Datta, Regulation of EMT in Colorectal Cancer: A Culprit in Metastasis, Cancers, 9 (2017).

[179] E. Pretzsch, F. Bösch, J. Neumann, P. Ganschow, A. Bazhin, M. Guba, J. Werner, M. Angele, Mechanisms of Metastasis in Colorectal Cancer and Metastatic Organotropism: Hematogenous versus Peritoneal Spread, Journal of Oncology, 2019 (2019).

[180] L.L. Gunderson, J.M. Jessup, D.J. Sargent, F.L. Greene, A. Stewart, Revised Tumor and Node Categorization for Rectal Cancer Based on Surveillance, Epidemiology, and End Results and Rectal Pooled Analysis Outcomes, Journal of Clinical Oncology, 28 (2010) 256-263.

[181] A. Leslie, F.A. Carey, N.R. Pratt, R.J.C. Steele, The colorectal adenoma-carcinoma sequence, British Journal of Surgery, 89 (2002) 845-860.

[182] R. Labianca, B. Nordlinger, G.D. Beretta, A. Brouquet, A. Cervantes, E.G.W. Grp, Primary colon cancer: ESMO Clinical Practice Guidelines for diagnosis, adjuvant treatment and follow-up, Annals of Oncology, 21 (2010) 70-77.

[183] R.M. McQuade, V. Stojanovska, J.C. Bornstein, K. Nurgali, Colorectal Cancer Chemotherapy: The Evolution of Treatment and New Approaches, Current Medicinal Chemistry, 24 (2017) 1537-1557.

[184] M.F. Häfner, J. Debus, Radiotherapy for Colorectal Cancer: Current Standards and Future Perspectives, Visceral Medicine, 32 (2016) 172-177.

[185] D. Zahavi, L. Weiner, Monoclonal Antibodies in Cancer Therapy, Antibodies, 9 (2020).

[186] N.A. Johdi, N.F. Sukor, Colorectal Cancer Immunotherapy: Options and Strategies, Frontiers in Immunology, 11 (2020).

[187] F. Soetaert, P. Korangath, D. Serantes, S. Fiering, R. Ivkov, Cancer therapy with iron oxide nanoparticles: Agents of thermal and immune therapies, Advanced Drug Delivery Reviews, 163 (2020) 65-83.

[188] M. Dabaghi, S.M.M. Rasa, E. Cirri, A. Ori, F. Neri, R. Quaas, I. Hilger, Iron Oxide Nanoparticles Carrying 5-Fluorouracil in Combination with Magnetic Hyperthermia Induce Thrombogenic Collagen Fibers, Cellular Stress, and Immune Responses in Heterotopic Human Colon Cancer in Mice, Pharmaceutics, 13 (2021).

[189] S.H. Jalalian, S.M. Taghdisi, N.S. Hamedani, S.A.M. Kalat, P. Lavaee, M. ZandKarimi, N. Ghows, M.R. Jaafari, S. Naghibi, N.M. Danesh, M. Ramezani, K. Abnous, Epirubicin loaded super paramagnetic iron oxide nanoparticle-aptamer bioconjugate for combined colon cancer therapy and imaging in vivo, European Journal of Pharmaceutical Sciences, 50 (2013) 191-197.

[190] A.A. Alkahtane, H.A. Alghamdi, A.T. Aljasham, S. Alkahtani, A possible theranostic approach of chitosan-coated iron oxide nanoparticles against human colorectal carcinoma (HCT-116) cell line, Saudi Journal of Biological Sciences, 29 (2022) 154-160.

[191] S. Wang, W.M. Li, D.Z. Yuan, J.D. Song, J. Fang, Quantitative detection of the tumor-associated antigen large external antigen in colorectal cancer tissues and cells using quantum dot probe, International Journal of Nanomedicine, 11 (2016) 235-247.

[192] J.L. Carbary-Ganz, W.A. Welge, J.K. Barton, U. Utzinger, In vivo molecular imaging of colorectal cancer using quantum dots targeted to vascular endothelial growth factor receptor 2 and optical coherence tomography/laser-induced fluorescence dual-modality imaging, Journal of Biomedical Optics, 20 (2015).

[193] S. Eynali, S. Khoei, S. Khoee, E. Esmaelbeygi, Evaluation of the cytotoxic effects of hyperthermia and 5-fluorouracil-loaded magnetic nanoparticles on human colon cancer cell line HT-29, International Journal of Hyperthermia, 33 (2017) 327-335.

[194] K.T. Al-Jamal, J. Bai, J.T.W. Wang, A. Protti, P. Southern, L. Bogart, H. Heidari, X.J. Li, A. Cakebread, D. Asker, W.T. Al-Jamal, A. Shah, S. Bals, J. Sosabowski, Q.A. Pankhurst, Magnetic Drug Targeting: Preclinical in Vivo Studies, Mathematical Modeling, and Extrapolation to Humans, Nano Letters, 16 (2016) 5652-5660.

[195] P.P. Wu, Q. Zhou, H.Y. Zhu, Y. Zhuang, J. Bao, Enhanced antitumor efficacy in colon cancer using EGF functionalized PLGA nanoparticles loaded with 5-Fluorouracil and perfluorocarbon, Bmc Cancer, 20 (2020).

[196] J.J. Xie, J.C. Wang, H.N. Chen, W.Y. Shen, P.J. Sinko, H.Y. Dong, R.L. Zhao, Y.S. Lu, Y.W. Zhu, L. Jia, Multivalent Conjugation of Antibody to Dendrimers for the Enhanced Capture and Regulation on Colon Cancer Cells, Scientific Reports, 5 (2015).

[197] M. Alibolandi, F. Hoseini, M. Mohammadi, P. Ramezani, E. Einafshar, S.M. Taghdisi, M. Ramezani, K. Abnous, Curcumin-entrapped MUC-1 aptamer targeted dendrimer-gold hybrid nanostructure as a theranostic system for colon adenocarcinoma, International Journal of Pharmaceutics, 549 (2018) 67-75.

[198] M. Alibolandi, S.M. Taghdisi, P. Ramezani, F.H. Shamili, S.A. Farzad, K. Abnous, M. Ramezani, Smart AS1411-aptamer conjugated pegylated PAMAM dendrimer for the superior delivery of camptothecin to colon adenocarcinoma in vitro and in vivo, International Journal of Pharmaceutics, 519 (2017) 352-364.

[199] A. Narmani, M. Kamali, B. Amini, A. Salimi, Y. Panahi, Targeting delivery of oxaliplatin with smart PEG-modified PAMAM G4 to colorectal cell line: In vitro studies, Process Biochemistry, 69 (2018) 178-187.

[200] Y. Barenholz, Doxil® - The first FDA-approved nano-drug: Lessons learned, Journal of Controlled Release, 160 (2012) 117-134.

[201] M.D. Fulton, W. Najahi-Missaoui, Liposomes in Cancer Therapy: How Did We Start and Where Are We Now, International Journal of Molecular Sciences, 24 (2023).

[202] T. Dragovich, D. Mendelson, S. Kurtin, K. Richardson, D. Von Hoff, A. Hoos, A phase 2 trial of the liposomal DACH platinum L-NDDP in patients with therapy-refractory advanced colorectal cancer, Cancer Chemotherapy and Pharmacology, 58 (2006) 759-764.

[203] P.C. Lyon, L.F. Griffiths, J. Lee, D. Chung, R. Carlisle, F. Wu, M.R. Middleton, F.V. Gleeson, C.C. Coussios, Clinical trial protocol for TARDOX: a phase I study to investigate the feasibility of targeted release of lyso-thermosensitive liposomal doxorubicin (ThermoDox®) using focused ultrasound in patients with liver tumours, Journal of Therapeutic Ultrasound, 5 (2017).

[204] M. Regenold, P. Bannigan, J.C. Evans, A. Waspe, M.J. Temple, C. Allen, Turning down the heat: The case for mild hyperthermia and thermosensitive liposomes, Nanomedicine-Nanotechnology Biology and Medicine, 40 (2022).

[205] M.M. Manni, M.L. Tiberti, S. Pagnotta, H. Barelli, R. Gautier, B. Antonny, Acyl chain asymmetry and polyunsaturation of brain phospho ipids facilitate membrane vesiculation without leakage, Elife, 7 (2018).

[206] S. Takamori, M. Holt, K. Stenius, E.A. Lemke, M. Gronborg, D. Riedel, H. Urlaub, S. Schenck, B. Brügger, P. Ringler, S.A. Müller, B. Rammner, F. Gräter, J.S. Hub, B.L. De Groot, G. Mieskes, Y. Moriyama, J. Klingauf, H. Grubmüller, J. Heuser, F. Wieland, R. Jahn, Molecular anatomy of a trafficking organelle, Cell, 127 (2006) 831-846.

[207] L.L. Holte, S.A. Peter, T.M. Sinnwell, K. Gawrisch, ^{2}H Nuclear Magnetic Resonance Order Parameter Profiles Suggest a Change of Molecular Shape for Phosphatidylcholines Containing a Polyunsaturated Acyl Chain, in, Biophysical Journal, 1995, pp. 2396-2403.

[208] J. Steinkühler, E. Sezgin, I. Urbancic, C. Eggeling, R. Dimova, Mechanical properties of plasma membrane vesicles correlate with lipid order, viscosity and cell density, Communications Biology, 2 (2019).

[209] P.K. Smith, R.I. Krohn, G.T. Hermanson, A.K. Mallia, F.H. Gartner, M.D. Provenzano, E.K. Fujimoto, N.M. Goeke, B.J. Olson, D.C. Klenk, Measurement Of Protein Using Bicinchoninic Acid, Analytical Biochemistry, 150 (1985) 76-85.

[210] K.J. Wiechelman, R.D. Braun, J.D. Fitzpatrick, Investigation Of The Bicinchoninic Acid Protein Assay - Identification Of The Groups Responsible For Color Formation, Analytical Biochemistry, 175 (1988) 231-237.

[211] R.E. Morton, T.A. Evans, Modification Of The Bicinchoninic Acid Protein Assay To Eliminate Lipid Interference In Determining Lipoprotein Protein-Content, Analytical Biochemistry, 204 (1992) 332-334.

[212] S. Rayamajhi, T.D.T. Nguyen, R. Marasini, S. Aryal, Macrophage-derived exosome-mimetic hybrid vesicles for tumor targeted drug delivery, Acta Biomaterialia, 94 (2019) 482-494.

[213] C. Chen, S.J. Zhao, A. Karnad, J.W. Freeman, The biology and role of CD44 in cancer progression: therapeutic implications, Journal of Hematology & Oncology, 11 (2018).

[214] L.F. Yu, L. Zhao, H.Z. Wu, H.S. Zhao, Z.J. Yu, M. He, F. Jin, M.J. Wei, Moesin is an independent prognostic marker for ER-positive breast cancer, Oncology Letters, 17 (2019) 1921-1933.

[215] W.D. Liao, G.H. Li, Y. You, H.P. Wan, Q. Wu, C.W. Wang, N.H. Lv, Antitumor activity of Notch-1 inhibition in human colorectal carcinoma cells, Oncology Reports, 39 (2018) 1063-1071.

[216] B. Győrffy, I. Stelniec-Klotz, C. Sigler, K. Kasack, T. Redmer, Y. Qian, R. Schäfer, Effects of RAL signal transduction in KRAS- and BRAF-mutated cells and prognostic potential of the RAL signature in colorectal cancer, Oncotarget, 6 (2015) 13334-13346.

[217] NanoSystems, NanoAssemblr® Spark™ User Guide, 2022.

[218] S. Bhattacharjee, DLS and zeta potential - What they are and what they are not?, Journal of Controlled Release, 235 (2016) 337-351.

[219] F.J. Martin, J.K. Morano, Liposome Extrusion Method, in, U.S. Patent 06/829,710, 12 April 1988.

[220] J.Y. Wu, Y.J. Li, J.M. Wang, X.B. Hu, S. Huang, S.L. Luo, D.X. Xiang, Multifunctional exosome-mimetics for targeted anti-glioblastoma therapy by manipulating protein corona, Journal of Nanobiotechnology, 19 (2021).

[221] J.P. Patterson, Y.F. Xu, M.A. Moradi, N. Sommerdijk, H. Friedrich, CryoTEM as an Advanced Analytical Tool for Materials Chemists, Accounts of Chemical Research, 50 (2017) 1495-1501.

[222] M. Almgren, K. Edwards, G. Karlsson, Cryo transmission electron microscopy of liposomes and related structures, Colloids and Surfaces a-Physicochemical and Engineering Aspects, 174 (2000) 3-21.

[223] S. Rayamajhi, R. Marasini, T.D.T. Nguyen, B.L. Plattner, D. Biller, S. Aryal, Strategic reconstruction of macrophage-derived extracellular vesicles as a magnetic resonance imaging contrast agent, Biomaterials Science, 8 (2020) 2887-2904.

[224] L.M.S. Loura, M. Prieto, FRET in membrane biophysics: an overview, Frontiers in Physiology, 2 (2011).

[225] D.K. Struck, D. Hoekstra, R.E. Pagano, Use of resonance energy transfer to monitor membrane fusion, in, Biochemistry, 1981, pp. 4093-4099.

[226] G. van den Bogaart, M.G. Holt, G. Bunt, D. Riedel, F.S. Wouters, R. Jahn, One SNARE complex is sufficient for membrane fusion, Nature Structural & Molecular Biology, 17 (2010) 358-U129.

[227] L.Z. Liu, D.Y. Pan, S. Chen, M.V. Martikainen, A. Kårlund, J. Ke, H. Pulkkinen, H. Ruhanen, M. Roponen, R. Käkelä, W.J. Xu, J. Wang, V.P. Lehto, Systematic design of cell membrane coating to improve tumor targeting of nanoparticles, Nature Communications, 13 (2022).

[228] M. Huch, B.K. Koo, Modeling mouse and human development using organoid cultures, Development, 142 (2015) 3113-3125.

[229] W. Zakrzewski, M. Dobrzynski, M. Szymonowicz, Z. Rybak, Stem cells: past, present, and future, Stem Cell Research & Therapy, 10 (2019).

[230] M. Scalise, F. Marino, L. Salerno, E. Cianflone, C. Molinaro, N. Salerno, A. De Angelis, G. Viglietto, K. Urbanek, D. Torella, From Spheroids to Organoids: The Next Generation of Model Systems of Human Cardiac Regeneration in a Dish, International Journal of Molecular Sciences, 22 (2021).

[231] M. Kim, H. Mun, C.O. Sung, E.J. Cho, H.J. Jeon, S.M. Chun, D.J. Jung, T.H. Shin, G.S. Jeong, D.K. Kim, E.K. Choi, S.Y. Jeong, A.M. Taylor, S. Jain, M. Meyerson, S.J. Jang, Patient-derived lung cancer organoids as in vitro cancer models for therapeutic screening, Nature Communications, 10 (2019).

[232] A. Al Shihabi, A. Davarifar, H.T.L. Nguyen, N. Tavanaie, S.D. Nelson, J. Yanagawa, N. Federman, N. Bernthal, F. Hornicek, A. Soragni, Personalized chordoma organoids for drug discovery studies, Science Advances, 8 (2022).

[233] T. Frum, J.R. Spence, hPSC-derived organoids: models of human development and disease, Journal of Molecular Medicine-Jmm, 99 (2021) 463-473.

[234] Z.X. Zhao, X.Y. Chen, A.M. Dowbaj, A. Sljukic, K. Bratlie, L.D. Lin, E.L. Fong, G.M. Balachander, Z.W. Chen, A. Soragni, M. Huch, Y.A. Zeng, Q. Wang, H. Yu, Organoids, Nature Reviews Methods Primers, 2 (2022).

[235] T. Sato, D.E. Stange, M. Ferrante, R.G.J. Vries, J.H. van Es, S. van den Brink, W.J. van Houdt, A. Pronk, J. van Gorp, P.D. Siersema, H. Clevers, Long-term Expansion of Epithelial Organoids From Human Colon, Adenoma, Adenocarcinoma, and Barrett's Epithelium, Gastroenterology, 141 (2011) 1762-1772.

[236] S. Date, T. Sato, Mini-Gut Organoids: Reconstitution of Stem Cell Niche, Annual Review of Cell and Developmental Biology, Vol 31, 31 (2015) 269-289.

[237] A. Ootani, X.N. Li, E. Sangiorgi, Q.T. Ho, H. Ueno, S. Toda, H. Sugihara, K. Fujimoto, I.L. Weissman, M.R. Capecchi, C.J. Kuo, Sustained in vitro intestinal epithelial culture within a Wnt-dependent stem cell niche, Nature Medicine, 15 (2009) 1-U140.

[238] X.Z. Ai, S.Y. Wang, Y.O. Duan, Q.Z. Zhang, M.S. Chen, W.W. Gao, L.F. Zhang, Emerging Approaches to Functionalizing Cell Membrane-Coated Nanoparticles, Biochemistry, 60 (2021) 941-955.